LBL--14643

DE82 020127

INTERSTITIAL-PHASE PRECIPITATION IN IRON-BASE ALLOYS: A COMPARATIVE STUDY

Alan Roy Pelton

Ph.D. Thesis

June 1982

Materials and Molecular Research Division
Lawrence Berkeley Laboratory
University of California
Berkeley, CA 94720

This work was supported by the Director, Office of Energy Research, Office of Basic Energy Sciences, Materials Science Division of the U.S. Department of Energy under Contract No. DE-AC03-76SF00098.

TABLE OF CONTENTS

INTERSTITIAL PHASE PRECIPITATION IN IRON-BASE ALLOYS: A COMPARATIVE STUDY

by

Alan R. Pelton

ABSTRACT

Recent developments have elucidated the atomistic mechanisms of precipitation of interstitial elements in simple alloy systems. However, in the more technologically important iron base alloys, interstitial phase precipitation is generally not well understood. The present experimental study was therefore designed to test the applicability of these concepts to more complex ferrous alloys. Hence, a comparative study was made of interstitial phase precipitation in ferritic Fe-Si-C and in austenitic phosphorus-containing Fe-Cr-Ni steels. These systems were subjected to a variety of quench-age thermal treatments, and the microstructural development was subsequently characterized by transmission electron microscopy.

A pattern emerged from these investigations which demonstrated the interrelationships between lattice defects and interstitial atoms in the formation of oversize second phases. Specifically, intragranular precipitation of disparate phases requires the structural and volume accommodation provided by vacancies and dislocations. Two distinct roles of vacancies were observed to be operational in these steels: In the ferritic alloy, the lattice pertubation associated with a single vacancy

is capable of nucleating a carbide. A model is proposed by which the carbide nucleus may grow into a bct structure by the successive jumps of the vacancy followed by the addition of migrating carbon atoms. In the austenitic alloy, the formation of the incipient phosphide phase is interpreted in terms of co-precipitation of vacancies and phosphorus atoms. The partial collapse of the sheet of vacancies on {100} planes provides the necessary accommodation for a layer of phosphorus atoms. The resulting stacking fault additionally affords a structure for further precipitation. It is suggested that the carbides ($M_{23}C_6$-type) precipitate in the stainless steel by a similar mechanism to that in Fe-Si-C. These results confirm the general validity of the concepts developed for model systems. Moreover, these findings have important implications for sophisticated alloy design.

1.0 Introduction

Interstitial elements, such as hydrogen, carbon, nitrogen and oxygen, often play a dominant role in determining the properties of metallic alloys. The effects of these elements may be beneficial; consider, for example, the well-known strengthening role of carbon and nitrogen in steels. Strengthening occurs from interstitials in solid solution as well as from precipitation of interstitial phases (carbide and nitrides). Examples of material degradation due to interstitials include hydrogen embrittlement and oxidation. Unfortunately, the precise atomic mechanisms of metal-interstitial interactions have not been entirely unveiled. Similarly, the interactions between interstitial solute atoms and vacant lattice sites are largely unknown. These vacancy-interstitial impurity (V-I) interactions are of utmost importance in materials subjected to drastic environments, such as in alloys designed for use in nuclear fission and fusion reactors [1]. However, similar interactions may also occur during routine materials processing; for example, in quench-age treatments. Indeed, these fundamental interactions between vacancies and interstitial elements may determine the ultimate fate of the solute: the kinetics, morphology and crystallography of subsequently formed interstitial phases may depend on the initial V-I pairing.

The experimental difficulties encountered in these investigations should not be overlooked [2]. Even the most sophisticated high-resolution transmission electron microscopes (TEM) are unable to image single vacancies or interstitial atoms in close-packed materials. However, TEM is a powerful technique for studying groups of vacancies and/or

solute atoms. Potentially, field-ion microscopy holds the most promise for directly imaging individual atomic species. Although in practice this technique has not been employed in many investigations of this nature because not all materials may be unambiguously studied [3].

Thus, other indirect experimental techniques must be used to infer the presence of vacancies and trace quantities of interstitials. For example, changes in electrical resistivity have been used to estimate the concentration of excess vacancies in various alloys [4]. Positron annihilation spectroscopy (PAS) techniques have also been employed to "detect" vacancies and V-I interactions [5]. Internal friction methods were developed to measure the amount of interstitial atoms retained in solid solution in body-centered cubic (bcc) alloys [6]. Unfortunately, data interpretation from these experimental methods is not always straight forward. Since no single technique is currently able to provide all the answers, researchers must collate data from various sources. A realistic picture of the fundamental V-I interactions may then be painted.

This thesis is concerned primarily with the interrelationships between interstitial elements and vacancies in iron-base alloys. A major goal was to elucidate the role of vacancies in the precipitation of interstitial phases. The materials selected for this research are a bcc Fe-2Si-0.1C steel and a face-centered cubic (fcc) Fe-18Cr-10Ni-0.3P-0.01C steel. (All compositions, unless otherwise noted, are in weight percent). The precipitation reactions were monitored by TEM, and the results compared with data from other experimental methods on similar alloys.

In order to place the present research in proper context, it is helpful to review the precipitation reactions in other bcc and fcc iron-base systems. Section 1.1 highlights the pertinent investigations of interstitial precipitation in ferritic alloys, while Section 1.2 discusses precipitation in austenitic steels. Vacancy-interstitial solute atom interactions will be emphasized in these introductory reviews.

1.1 Interstitial Precipitation in Ferritic Steels

Metastable carbide precipitation in low-carbon ferritic steels has been extensively studied by various experimental techniques (e.g. see references [7] and [8]). However, many questions regarding the precipitation of carbon from α-iron remain unanswered. For example, the precise characterization of the initial interstitial precipitate phase, in terms of crystal structure and chemistry are not yet clear. Also lacking is an atomistic model of the nucleation and growth processes. This dearth of knowledge is mainly due to the low scattering power and low volume fraction of the incipient carbide; thus, X-ray and electron diffraction evidence is scarce. Some authors [9,10] identify the structure as epsilon carbide, the transitional phase found in high-carbon martensites. Others [11,12] suggest a structure isomorphous with $Fe_{16}N_2(\alpha'')$ which is the metastable phase found in Fe-N alloys. From early TEM studies, the transitional precipitate in binary Fe-C alloys was observed to be disc-shaped with {100} habit planes. A summary of these studies follows. Leslie [13] investigated the effects of alloying elements on carbon precipitation in ferrite. With constant C content (~0.014%), the {100} precipitates were stable up to approximately 150°C for binary Fe-C alloys. Additions of 3.25 % Si increased the stability of the carbides up to 600°C,

whereas 0.45% Mn suppressed the formation of {100} precipitates. In the Mn-containing alloy, only {110} carbides (cementite) were observed even at the lowest aging temperature examined (60°C). Subsequent investigations (e.g. refs. [14-16]) have used the habit plane criterion to distinguish between the initial carbide and cementite.

Various models of the precipitation mechanisms have been postulated to explain the formation of the {100} carbides. Most of the models propose an interaction between quenched-in vacancies and supersaturated carbon atoms. For example, Leslie [13] suggested that metastable carbides originate at vacant lattice sites. Based upon a comparison between the density of precipitates and the calculated concentration of excess vacancies, he estimated that 1 to 10 vacancies participate in the formation of a carbide. Hull and Mogford [16] made a comparative study of carbide precipitation during neutron irradiation and quench-aging. They proposed that the nuclei of the carbides in the irradiated Fe-C alloys consisted of displacement spikes. They estimated that each displacement spike consisted of approximately 10 to 100 vacancies surrounded by a much wider region containing self-interstitials. The central vacancy-rich region could provide a potent sink for carbon atoms. This calculated number of displacement spikes was 2×10^{14} cm^{-3}, which is in good agreement with the observed number of particles. The density of precipitates in the samples fast-cooled from 900°C and aged at 100°C was 2×10^{13} cm^{-3}. Assuming a considerable loss of vacancies due to the inefficient quench, the vacancy content per particle was estimated to be 100. These authors further proposed that the structure of the {100} precipitates consisted of a monatomic layer of carbon in the [0,0,1/2] intertices. The arrangement

of atoms around the carbon-rich layer is similar to a closed loop of an edge dislocation in the (001) plane. The lattice displacement would be about 0.35a, where a is the ferrite lattice parameter.

In a series of papers, Damask, et al. [17-20] investigated the kinetics of carbon precipitation in irradiated iron. Internal friction [17] and electrical resistivity [18] measurements indicated that carbon is trapped at defects prior to precipitation. Calorometric studies [19] suggest a binding energy of 0.41 eV/atom between carbon and the irradiation-produced defects. In quenched-aged samples, the energy released per carbon atom to form metastable {100} carbides (observed via TEM [20]) was measured to be 0.27 eV [19]. From these results, the authors concluded that in the presence of a sufficient concentration of point defects (assumed to be vacancies) the kinetics of carbide formation is retarded. Similar conclusions were reached by Takeyama and Takahashi [21] in their investigation of electron-irradiated Fe-C alloys.

Further evidence for vacancy-carbon (V-C) interactions have been provided from PAS studies [22,23]. In one investigation [22], a comparison was made between vacancy concentrations (from positron angular correlation measurements) and carbon content in solid solution (from internal friction measurements) as a function of temperature in neutron-irradiated Fe-C binaries. Between 50-100°C there is a decrease in the concentration of vacancies which coincides with the decrease in the carbon in solution. Positron lifetime measurements were also made on several purities of electron-irradiated iron [23]. Increasing carbon concentrations (5-750 atomic ppm) increases the number of monovacancies retained. These authors ascribe this behavior to the capture of migrating

vacancies by relatively less mobile carbon atoms resulting in bound C-V pair formation. Furthermore, they propose that the carbon atom is located off the center of the vacancy; i.e. the pair does not combine into a substitutional carbon atom. These results are similar to computer modeling studies [24] which propose that the most stable monovacancy-carbon complex has a binding energy of 0.42 eV. The configuration for this complex is a carbon atom of approximately 0.36a from the vacancy along <001>.

As a final example of carbide precipitation of low-carbon ferrite, Vyhnal and Radcliffe (VR) [25], showed that the density of transitional carbides is dependent upon the quench rate. They propose a nucleation model for the carbides based on the dynamic equilibrium between vacancies, carbon atoms, and vacancy-carbon pairs.

VR propose that as the cooling rate increases, higher concentrations of vacancies are retained from the solution temperature. At room temperature, these vacancies exist as stable V-C pairs, which may serve as nucleation sites for subsequent carbide formation.

The above examples provide strong evidence of vacancy-carbon interactions in quenched-aged and irradiated low-carbon ferritic alloys. While metastable carbide precipitation is a common phenomenon in these alloys, analogous precipitation from the duplex ferrite-martensite systems has received little attention. Since these alloys are currently of great interest and importance, a brief summary of the most pertinent investigations of precipitation in quenched and room-temperature aged steels follows.

The first reported observation of carbide precipitation in the ferritic phase of dual-phase steels was by Young [26]. He studied the

structure-property relationships in AISI 1010 and 1020 steels and observed large densities of "unidentified particles" in the ferrite matrix and on dislocations, with precipitate-free zones (PFZ's) near grain boundaries (e.g., Figure 5 of reference [26]). Later, O'Neill [27] found "rods" within the ferrite of an Fe - 1Al - 0.06C alloy. It was assumed that these particles were AlN precipitates since the steel was air-melted. However, a subsequent investigation [28] has shown that these particles are present in both air and vacuum-melted Fe-Al-C steels. It was suggested [27,28,29] that due to the strengthening of the ferrite by these particles that the tensile properties are independent of the volume fraction of martensite. Precipitates were also observed in Fe - 0.4Si - 1Al - 0.6C alloys [27]; however, this system appears to follow the two-phase rule of mixture. This empirical rule predicts increasing strength with increasing volume fraction of martensite [30].

Alloying low-carbon steels with Mo or Nb also produced fine precipitates which appear to induce deviations from the law of mixtures [31]. Hoel and Thomas [32] studied the precipitation in these steels, and observed precipitate densities of approximately 7×10^{15} cm^{-3}; for equivalent thermal treatments, the density was constant for the two systems. It was shown that these plate-shaped precipitates have {100} habit planes and that the plate diameter ranges from 4 - 25 nm. It was additionally shown that the particles have dislocation-loop contrast which changes by reversing the diffraction vector. Moreover, these authors suggest that the inside/outside contrast is consistent with vacancy-type strain fields.

Similar observations of precipitation in ferrite were made in dual-phase steels containing Mo and Nb [33] and V [34]. A summary of these two investigations is presented in a paper jointly authored by Gau, Koo Nakagawa and Thomas [35]. They suggested that these carbides (or carbonitrides) are formed during the quench due to supersaturations of carbon and/or nitrogen.

Thus, it appears the precipitation in dual phase steels is also a general phenomenon. Alloys containing elements which decrease the activity of carbon in ferrite (i.e., "carbide formers" - Mo, Nb, V and Mn) as well as alloys with substitutional additions which increase the activity of carbon in ferrite (i.e., "carbide inhibitors" - Si and Al) exhibit extensive carbide precipitation. The precipitation behavior of an Fe - 2Si - 0.1C alloy is presented in this thesis. In the original study of this alloy [36], no observations of precipitation in the natural-aged samples were reported. However, a subsequent investigation [37] revealed copious carbide precipitation in specimens which had aged at room temperature for several years.

In the next section, interstitial precipitation in austenitic stainless steels is reviewed.

1.2 Interstitial Precipitation in Austenitic Stainless Steels

Precipitation in austenitic stainless steels was recently reviewed by Edmonds and Honeycombe [7]. They discuss the various types of interstitial phases (carbides and nitrides) observed in this class of alloys. The major precipitating phase in unmodified austenites is $M_{23}C_6$. This chromium-rich carbide has a complex cubic structure (Fm3m, $D8_4$) with 92 metal atoms per unit cell [38,39]. The lattice parameter is 1.06nm,

which is approximately three times larger than the austenite unit cell (0.36nm) [38,40]. Other substitutional solutes such as Fe, Mo, Ni, and W can replace Cr on the metal lattice.

TEM investigations [40-53] of quenched-aged (500-850°C) austenitic steels have revelaed that $M_{23}C_6$ precipitates on grain boundaries, dislocations, and within the matrix. In general, grain boundary precipitation is favored at the higher aging temperatures with intragranular precipitation occuring at lower temperatures. Lewis and Hattersley [41] observed carbides on grain boundaries, on extrinsic dislocations which are on coherent twin boundaries, and on non-coherent twin boundaries after aging at 750°C for 0.5h. After slightly longer aging times, precipitation on matrix dislocations was detected. Beckitt and Clark [42] confirmed these results; in addition, these investigators studied the formation of dislocation-carbide stringers in long-aged samples. Trace analysis of the carbides indicated that the preferred matrix-precipitate interfaces are {111} and {110} planes. From electron diffraction evidence, the orientation relationship between the parent (γ) and product ($M_{23}C_6$) is:

$$\{100\}_\gamma \,//\, \{100\}\ M_{23}C_6$$
$$\langle 001\rangle_\gamma \,//\, \langle 001\rangle\ M_{23}C_6$$

Kcgg and Silcock [43,44] studied $M_{23}C_6$ precipitation in Fe-Cr-Ni alloys containing 0.25%C. They observed that the carbides continued to nucleate on climbing dislocations, and that those dislocations with large edge components produced uniform planar arrays of precipitates on {110} planes. The climbing dislocations produced vacancies able to accommodate the ~11% volume expansion associated with carbide formation.

Matrix precipitation of $M_{23}C_6$ is facilitated by three conditions:

(i) lower aging temperatures

(ii) irradiation

(iii) phosphorus additions

After aging a stainless steel for 15h at 650°C, Singhal and Martin [48] observed a homogeneous dispersion of "matrix-dot" precipitates with spherical strain fields as well as denuded regions near grain boundaries. These authors associated the PFZ's with vacancy depletion, and thus concluded that vacancies are essential to the formation of the $M_{23}C_6$ carbides. Similar conclusions were reached in other studies [43,49].

Nickel-ion irradiation of an 18Cr-14Ni stainless steel produced copious precipitation of $M_{23}C_6$ at irradiation temperatures less than 600°C [50]. The carbides were between 2-10nm in diameter, and were uniformly distributed throughout the matrix. In the presence of carbides, no voids or dislocation loops were observed; these latter defects formed at higher irradiation temperatures. The author concluded that vacancies determined the nucleation sites for the carbides. Neutron irradiation also enhances matrix precipitation of $M_{23}C_6$ over the temperature range 525-610°C [40,51].

A third condition for producing matrix $M_{23}C_6$ precipitates in stainless steels is by additions of approximately 0.3%P. Since the present investigation concerns a phosphorus-containing stainless steel, a more complete review of the effects of this element on precipitation reactions follows.

1.3 The Effects of Phosphorus

The effects of minor additions of phosphorus to austenitic stainless steels have been studied for many years. One of the earliest systematic investigations was reported in 1954 by Allten, Chow and Simon [56]. They found that increasing the phosphorus content from 0.03 to 0.5% in a Fe-21Cr-12Ni-0.5C steel resulted in the following:

(1) Increased hardness

(2) The times for the start of precipitation hardening were decreased.

(3) The rates of precipitation and precipitation hardening were increased.

(4) The degree of dispersion of the precipitate increased.

(5) The austenite lattice parameter increased.

Furthermore, these authors detected only $M_{23}C_6$ precipitates (by X-ray diffraction); no phosphorus compounds were observed. It was therefore concluded that phosphorus was dissolved interstitially in the matrix, but did not precipitate during the aging temperatures. Rather, it was suggested that the role of phosphorus was to provide nucleation sites for the $M_{23}C_6$.

Subsequent studies have shown that phosphorus strongly influences precipitation behavior and mechanical properties of austenitic stainless steels. For example, Rundell and Raudebaugh [57] obtained increased yield and ultimate tensile strengths in low-carbon steels with additions of phosphorus. In a study aimed to produce high-strength austenitic steels, Irvine, et al. [58] found that the best combinations of tensile strength and ductility were obtained when the total content of C,N and

P reached 0.4 - 0.5%. In addition, they found that increasing the phosphorus content decreased the austenite lattice parameter. Furthermore, they observed intragranular precipitates with a suggested composition of $M_{23}(C,P)_6$. These authors therefore concluded that phosphorus is a substitutional element in solid solution, but dissolves interstitially in the precipitates. Thomas and Weglein [59] reported that doping 18 Cr - 10Ni austenitic steels with 0.27 to 0.35%P increased room and high-temperature (~600°C) yield strengths. Henry, et. al. [52] examined the alloys from the previous study by TEM. In the steels exhibiting the highest strengths, they observed Bardeen-Herring dislocation loops and PFZ's near grain boundaries. They concluded that the increased high-temperature strength is due to precipitation of $M_{23}C_6$ on the vacancy-type dislocation loops. Depletion of vacancies was suggested to be responsible for the denuded grain-boundary regions. Stainless steels without phosphorus had lower strengths with no decorated dislocation loops.

Banerjee, Dulis and Hauser [53] studied 18 Cr - 9Ni - 4 Mn steels with 0.3%C and between 0.007 and 0.38%P, and they obtained results similar to earlier investigations; i.e., increasing phosphorus contents promotes finer dispersions of carbides. They interpreted their results in terms of carbide nucleation at vacancy-phosphorus (V-P) sites. From X-ray diffraction lattice parameter measurements, they concluded that phosphorus substitutes on the metal atom lattice of the carbide; hence, the phase was labeled $(M,P)_{23}C_6$. It is interesting to compare these results to those from Froes, Wells and Banerjee [54]. These latter authors investigated the critical temperature for homogeneous precipitation

in the same alloys used by Banerjee, et al. [53]. They determined that the critical temperature increases with increasing additions of phosphorus, and suggested that phosphorus increases the effective interstitial content of the steel, which may be due either to phosphorus entering the precipitate interstitially as $M_{23}(C,P)_6$ - or to increase in the effective supersaturation of carbon at the aging temperature. This discrepancy in the labeling of the carbide as $(M,P)_{23}\ C_6$ or $M_{23}\ (C,P)_6$ is puzzeling since Banerjee is common to both publications; no explanation for this is offered.

Rowcliffe and Nicholson [60] and Rowcliffe and Eyre [61] studied defect formation and precipitation reactions in low-carbon 18Cr - 10Ni steels with 0.3%P. The steels were quenched from 1100°C into liquid lead at temperatures between 400-750°C. These are their primary results:

(1) Needles and laths of Cr_3P on {100} habit planes were observed when the aging temperature was >700°C. Precipitation occurred mainly on grain boundaries and dislocations.

(2) Aging temperatures between 600-700°C produced pure edge vacancy loops with $\vec{b}$ = a/2 <110> on {110} habit planes. These are similar to Henry's et al. [52] results, and were described as climb-source loops. Precipitates with spherical strain fields (probably $M_{23}C_6$) were also occasionally observed.

(3) By lowering the aging temperatures to 500°C, vacancy-type loops with $\vec{b}$ = a <100> and {100} habit planes were obtained.

(4) Voids were formed after aging at 400°C.

(5) Precipitate-free (and loop-free) zones were observed adjacent to high angle grain boundaries and dislocations.

(6) None of these secondary defect structures were observed in the phosphorus-free steels of various compositions.

Kegg, Silcock and West [55] investigated the effects of phosphorus and cooling rate on the precipitation of $M_{23}C_6$ in high-carbon austenitic steels. They found that the rate of precipitation was much faster in the presence of phosphorus. The acceleration of the rate of nucleation was attributed to both a reduction in the interfacial energy and to an increase in the number of nucleating sites. It was suggested that these sites could be vacancy-phosphorus-chromium-carbon complexes. The growth rate also increased with increasing phosphorus content. They postulated that this effect may be ascribed to an increase in diffusivity due to an increase in retained vacancy concentration resulting from a high V-P binding energy. The solubility of phosphorus in the carbide phase is ~1 at %, with phosphorus primarily occupying carbon sites; i.e. $M_{23}(C,P)_6$. These authors found no evidence of voids.

Phosphorus additionally enhances the nucleation of NbC [62] and Cr_2N [63] in austenitic stainless steels. In both publications, the authors propose that phosphorus prolongs excess vacancy lifetime and provides nucleation sites for the interstitial phases. It was further suggested that the retained vacancies reduce the nucleation barrier by relieving transformation strains.

In an effort to understand the secondary defects observed in commerical-quality steels containing phosphorus [52,61,62], Azarian, et. al. [64] fabricated high-purity austenitic steels with phosphorus. In addition to the previously observed a/2 <110> loops, these authors observed Frank loops and stacking fault tetrahedra; no a<100> or voids were found. From

PAS experiments, the energy of vacancy formation in the phosphorus steels was found to be 1.4 $\pm$ 0.2 eV; without phosphorus, the formation energy is 1.6 $\pm$ 0.2 eV. In a recent publication, Azarian and Kheloufi [65] found convincing evidence from positron angular correlation data that vacancy concentrations are increased by additions of phosphorus. Conversely, boron additions do not significantly affect vacancy concentrations.

Similar conclusions on the effects of phosphorus were reached by Boulanger [66] by investigating void formation in slowly cooled Fe-18Cr-14Ni-P steels. He compared the vacancy content in the voids with the calculated equilibrium concentrations available at the quench temperature. When compared to models predicting various phosphorus-vacancy interactions, binding energies of 0.5-0.8eV were calculated.

From this survey of investigations, it appears that the primary role of phosphorus is to increase the excess vacancy concentrations. This is due to a strong (0.5 - 0.8 eV) V-P binding energy. In high-carbon or high-nitrogen steels, these V-P complexes facilitate nucleation of carbides ($M_{23}C_6$ or MC) and nitrides (M_2N). The location of phosphorus in the $M_{23}C_6$ phase is still a subject of controversy, however, it is generally accepted that in solid solution, phosphorus is a substitutional atom. In low-carbon alloys, V-P complexes form various types of vacancy-type defects; the {100} loops observed by Rowcliffe, et al. are the most novel. The present investigation is concerned with the study of these {100} defects, with emphasis on the mechanisms of defect formation and the role these defects play in subsequent interstitial phase precipitation.

2.0 Experimental Procedures

The chemistry of the alloys examined in this research program are listed in Table 1, and are categorized according to their solution and aging treatments in Table 2. Prior to thermal treatments, the alloys were hot rolled and cold rolled to ~75μm. After rolling, the samples were lightly sanded and electropolished to clean the surface. Electropolishing was generally performed at room temperature in a 200ml stainless steel beaker. The beaker served as the cathode to give a uniform current density from the anodic samples. For all alloys, current densities of ~0.5 amps per cm^2 produced shiny surfaces with isolated pits.

The ferritic alloys were electropolished with either 90 v/o acetic acid - 10 v/o perchloric acid or with a chromic acetic solution - 75 grams chromium trioxide dissolved in 10ml distilled water and 400ml acetic acid. A solution of 50 v/o orthophosphoric acid, 35 v/o sulphuric acid and 15 v/o ethyl alcohol was used for the stainless steel.

Solution treatments were carried out in vertical tube furnaces with separate thermocouples for controlling and for monitoring the temperature. Two major parameters in this investigation were the concentration of vacancies and the interstitial impurity content; therefore, the quenching apparatus was designed to maximize the quench rate while minimizing oxygen pick-up. These criteria were optimized by encapsulating the specimens in quartz under a static pressure of $\sim 5 \times 10^{-6}$ torr; tantalum foil was added to getter the residual oxygen. The quartz tubes were secured to a stainless steel support rod during the solutionizing treatments. These treatments were terminated by propelling the support rod into ice water thereby breaking the end of the tube and quenching the samples. An additional

function of the tantalum foil was to diminish the flow rate of the in-rushing water, which reduces the mechanical deformation of the thin foils.

Above-ambient aging of the ferritic steels was done in silicone oil baths. The stainless steel samples were re-encapsulated in quartz and aged in horizontal tube furnaces. The accuracy of the quoted aging temperatures is $\pm$ 5°C.

The majority of samples were heat treated in the above manner, i.e. by a quench-age treatment. There were two expections in the stainless steel treatments: a furnace-cooled ($\sim$3°/min) and a directly quenched treatment. These latter samples were quenched from 1150°C into a salt bath at 500°C without breaking the capsules.

The heat-treated samples were thinned to electron transparency in the above-mentioned solutions. The ferritic samples were jet polished in a Fishione unit at $\sim$40 volts and $\sim$0.5 amps/cm^2 current density. Austenitic specimens were obtained by the "dipping method" at <0°C using 10 volts and $\sim$0.5 amps/cm^2.

Various TEM's at different energies were used to view the samples, including: Siemens I at 120keV, Philips 301 at 100keV, Philips 400 at 100 or 120 keV and Siemens 102 at 100keV. Bright-field (BF) micrographs were taken in two-beam conditions with ξ positive. Weak-beam dark field (WBDF) imaging was done by beam tilting the diffracted beam to the optic axis. This procedure illuminates g/3g; the deviation parameter was adjusted by tilting the specimen. Traditional selected area diffraction (SAD) patterns were taken to record the diffraction conditions. In addition, certain experiments necessitated the use of a highly-convergent beam; the appendix outlines the convergent beam microdiffraction (CBMD)

techniques used in this research program.

Micrographs were printed with emulsion-side up, which reproduces imaging conditions in the microscope. The vector $\underset{\sim}{g}$ defines the upward specimen normal, and the diffraction patterns were indexed self-consistently. Directions in reciprocal space are denoted as <hkl>*, and in real space as <hkl>.

3.0 Experimental Results from the Fe-Si-C Alloy

The thermal treatments employed for this system were summarized in Table II. Samples of the Fe-Si-C alloy were quenched from the two-phase ($\alpha+\gamma$) region resulting in a mixture of ferrite and martensite. Figure 1 shows the structure of a sample quenched from 850°C and aged at room temperature for less than 1 hour. Figure 1(a) is from a ferrite region which shows scattered dislocations but no precipitates. The martensite in these specimens (a BF image is in Figure 1(b) and a DF in Figure 1(c)) was generally micro-twinned which is similar to earlier observations [36]. The remaining results concern only carbide precipitation in the ferrite phase, and will not address martensitic transformations.

3.1 Room Temperature Aging

Quenching from 850°C and aging for 1 week produces the ferritic microstructure seen in Figure 2. The beam direction is near [001] with $\underset{\sim}{g}$ = [110]*. These precipitates show black/white strain contrast. The density of precipitates is approximately 7×10^{15} cm^{-3} and the particles are ∿15nm in diameter. Trace analysis showed that the precipitates have {100} habit planes.

3.2 100°C Aging

Figures 3-5 show the structure of samples aged at 100°C after a 850°C quench - 25°C/1 week pre-age treatment. The density of precipitates is essentially the same as in Figure 2, except near dislocations and grain boundaries. However, the size of the particles has increased to ∿35 nm in diameter. This indicates that nucleation occurred during the pre-aging treatment and that the precipitates grew

at 100°C. Again, these particles have {100} habit planes. Another feature of the microstructure is the precipitation on dislocations. In general, two variants of the precipitates are associated with each dislocation. With the diffraction conditions of Figure 3 ($\underset{\sim}{\beta}$ = [011], $\underset{\sim}{g}$ = [01$\bar{1}$]*, the matrix precipitates show contrast similar to dislocation loops, which is expected from inclined, thin plates [67-70]. These "loops" show inside/outside contrast behavior when the diffraction vector is reversed. For example, in Figure 4 with $\underset{\sim}{\beta}$ near [011], two precipitate variants are inclined ~45° to the beam. These loops change image width with $\pm$ g = [01$\bar{1}$]*, for instance, see the precipitates near the asterisk. Unfortunately, due to limited specimen tilt (Siemens I microscope) a precise identification of habit planes was not possible. Therefore, the nature of the strain fields could not be determined. (At least three micrographs are necessary for this determination as explained in a later section).

Precipitate-free zones are observed near grain boundaries as seen in Figure 5. These boundaries appear to be small angle grain boundaries, although PFZ's are also observed near high angle boundaries.

Figure 6 shows a Centered Dark Field (CDF) micrograph with $\underset{\sim}{g}$ = [01$\bar{1}$]* and $\underset{\sim}{s}$ = 0; extreme care was taken to correctly orient the diffraction vector on the image. The black-white strain contrast of the carbide "loops" is quite evident. Following the convention proposed by Ashby and Brown [71,72], a vector $\underset{\sim}{l}$ is defined as pointing from the black lobe to the white lobe. In the CDF image, if $\underset{\sim}{l}$ is <u>antiparallel</u> to $\underset{\sim}{g}$, the defect has an interstitial-type strain field. This procedure is tantamount to stating that if $\underset{\sim}{g}$ points towards a black lobe, the

precipitate has an interstitial strain field. The overwhelming majority of precipitates in Figure 6 show interstitial-type strains, which is expected from a phase with increased atomic volume.

Another thermal treatment employed in this study was the 850°C quench-100°C/1h age - 25°C/2 week age. Typical microstructures of this treatment are shown in Figures 7 and 8. There is a bi-modal distribution of precipitate sizes; the larger particles are ∿50 nm in diameter while the smaller ones are ∿20 nm. The relative densities are $\sim 10^{5}$ cm^{-3} and $\sim 10^{15}$ cm^{-3} respectively for the large and small particles. Both sizes of precipitates have {100} habit planes. In Figure 8, these precipitates are imaged near $\underset{\sim}{B}$ = [001] with [200]* and [$\bar{1}\bar{1}$0]* diffraction vectors in BF, and with [110]* for DF. Several observations may be made from this series of micrographs. First, with $\underset{\sim}{g}$ = [200]* (Figure 8(a)) only one variant of the small defect is visible. These lie on (100) planes and show strain contrast. Both the (100) and (010) variants of the larger precipitates are visible in this micrograph. With the [$\bar{1}\bar{1}$0]* reflection, both sizes of particles have two variants in contrast. The DF image in Figure 8(c)} again shows that the precipitates have black/white strain contrast. However, the vector $\underset{\sim}{l}$ is not unidirectional in either size of precipitate since s≠0 in this case. Thus, this method could not be used to determine the nature of the strain fields. Another observation is that there are small, yet well-defined, PFZ's around the larger precipitates.

3.3. 170°C Aging

A final thermal treatment used for the Fe-Si-C alloy was the 850°C quench-170°C/1h age. A BF/WBDF pair of this treatment is shown in Figure

9. The beam direction is near [011]; $\underline{g}$ = [01$\bar{1}$]* for the BF and [0$\bar{1}$1]* for the WBDF with the $\underline{g}/3\underline{g}$ condition nearly satisfied. The precipitates formed after this treatment are ~100nm in diameter. In addition, the majority of precipitates have nucleated heterogeneously on dislocations and on low angle grain boundaries. The precipitates also have {100} habit planes. The fringes seen in the particles are displacement fringes which are expected from precipitates of this size and inclination to the beam [67-70].

4.0 Experimental Results from Fe-Cr-Ni-P-C Alloy

The phosphorus-containing stainless steel specimens were subjected to various quench-age treatments; these thermal treatments were specified in Table II. Three types of quenches were used to terminate the solutionizing treatments:

(1) Furnace cool to room temperature

(2) Ice-water quench to room temperature

(3) Direct quench to 500°C

After quenching, the samples were aged between 500°-700°C for times ranging from 1 to 100 hour, and were examined *via* TEM. The purpose of these experiments was to monitor the precipitation sequences in order to elucidate the various roles of vacancies. Since the resultant microstructures depend upon the thermal histories of the samples, this chapter is subdivided according to the type of quench and to the aging temperature/time.

4.1 Furnace Cool

The microstructure of a furnace-cooled ($\sim$3°/min) sample is shown in Figure 10. The austenitic matrix has a low density of dislocations and no signs of precipitation.

4.2 Ice-Water Quench

The TEM observations of the microstructures produced after ice-water quenching and aging treatments are reported in this section. The as-quenched structure is shown in Figure 11. In general, the microstructure consisted of austenitic grains with a low density of long ($\sim$800 nm), straight dislocations and helical arrays. No intragranular or dislocation

nucleated precipitates were visible in the as-quenched condition.

Aging this quenched supersaturated structure between 500-700°C produced various defects and precipitate phases. Only minor differences were observed in the samples aged at 500°C for 1 to 100h and at 600°C for 1 h. Therefore, the results of there thermal treatments will be presented together. The microstructures obtained after the other temperature/time schedules will be discussed separately.

4.2.1. Aging at 500°C/1-100h or at 600°C/1h

Four distinct modes of precipitation occurred upon aging the stainless steel samples in this temperature/time regime. They are:

(A) {100} faulted loops

(B) Fine matrix precipitates

(C) Coarse matrix precipitates

(D) Dislocation-nucleated precipitation

Grain boundary depleted zones were also observed in these samples and will be discussed in Section E.

A. {100} Faulted Loops

The microstructures developed after aging at 500°C for 1, 10 and 100h and at 600°C for 1h are shown in Figures 12-15 respectively. The beam direction of these micrographs is near $\underset{\sim}{B}$ = [110]. A [002]* diffraction vector was used in Figure 12, while <111>* type vectors were used to image Figures 13-15. Within this temperature/time regime, high densities ($\sim 10^{15}$ cm^{-3}) of homogeneously distributed precipitates have formed in the matrix. The sizes of these particles range from 10 to 35 nm and they were approximately 1-2 nm thick.

Increasing the aging time at 500°C or increasing the aging temperature to 600°C coarsens the precipitates slightly with a concomitant decrease in precipitate density. From trace analysis, these defects were found to adopt {100} habit planes. Only one variant of the defects is visible in Figure 12 and this is on edge perpendicular to $\underline{g}$. In the other micrographs, two variants are inclined ~45° to the beam, while the third variant is on edge. Figure 13-15 were imaged in both BF and W3DF conditions to better illuminate the fringe nature of the {100} loops. In addition, Figure 15 shows part of a diffraction contrast series which will be discussed in more detail below. The Kikuchi map in Figure 16 serves as a reciprocal lattice guide for the many tilting experiments employed in this study; consequently, the subsequent micrographs are indexed consistently with the map. Specifically, the diffraction vectors for the images in Figure 15 are marked on Figure 16 according to the approximate positions in reciprocal space.

The crystal structure of these {100} defects could not be determined from electron diffraction studies; conventional selected area diffraction patterns (SADP) failed to show any extra reflections. Therefore, convergent beam microdiffraction (CBMD) techniques were employed, but this also failed to reveal precipitate reflections. Figure 17 shows a CBMD pattern which was obtained by focussing a ~25 nm electron beam on a single defect. Exposure times of 30 sec to 3 min were used to produce these CBMD patterns; however, only matrix spots were visible. The sensitivity of this diffraction technique is sufficient to resolve second phase diffraction patterns as evidence from the crystal structure investigations of small precipitates in Ta-C [73] and Pt-C [74]. Therefore, two conclusions may be drawn to

explain the lack of precipitate diffraction patterns in the present study: Either the precipitate lattice parameters and symmetry are very close to those of the matrix resulting in overlapping of the patterns, or the scattering power of the phase is insufficient to allow it to be distinguished from the background intensity.

Although direct crystallographic identification of the {100} planar precipitates was not obtained, indirect structural information was acquired through diffraction contrast experiments. The rationale for using contrast analysis stems from the treatment of the precipitates as lattice defects, i.e., as dislocation loops. From image contrast theories [67-70], dislocation images arise from variations in intensities that are due to the local bending of the crystal in the vicinity of the lattice defects. Thus, by using suitable diffraction conditions, the magnitude and direction of the lattice displacement due to the precipitates (dislocation loops) are determined. Based on these diffraction contrast studies, models of the atomic structure of the precipitate phases may be constructed.

The diffraction contrast analysis of the lattice defects in Figure 15 will now be addressed. The two-fold purpose in this series of micrographs was to determine:

- the direction and magnitude of the lattice displacements (i.e., the Burgers and displacement vectors)
- the nature of the matrix strain field (vacancy-or interstitial-type)

Figures 15 (a,b) are a BF/WBDF pair with $\underset{\sim}{g}$ = [$\bar{1}$11]* and near $\underset{\sim}{\beta}$ = [110]. In these micrographs, the planar defects marked A and B show only fringe-type contrast, while defect C was on edge. As noted above,

this is consistent with {100} habit planes. With this diffraction vector, defect A had stronger contrast than defect B. Subsequent micrographs in this series were taken from the outlined area in Figure 15(a). Imaging with $\underset{\sim}{g} = [1\bar{1}1]^*$ near [110] (Figure 15(c)), resulted in three variants being visible. However, the fringe contrast from B was stronger than from A. (Discussions of and further examples of this asymmetry in the fault contrast are presented in a later section). Using $\underset{\sim}{g} = [002]^*$, A and B are out of contrast, while C is still visible, Figure 15(d). Defects A and B display dislocation-loop contrast and C is out of contrast with $g = \pm [\bar{2}20]^*$ (Figure 15(e,f)). However, with the $[\bar{2}20]^*$ diffraction vector, loop B has residual contrast, whereas loop A is in strong contrast. Using the opposite g-vector, B is strongly diffracting, but A is nearly invisible. This behavior is consistent with $\underset{\sim}{g}\cdot\underset{\sim}{b} = \pm 2/3$ with $w \geq 1.0$ [75]. After titling the sample ~45° along the $[002]^*$ Kikuchi band towards $\underset{\sim}{R} = [100]$, defect A rotated to an edge-on configuration and defect B was face on. Thus, A lies on (010), B is on (100) and C lies on (001). With $\underset{\sim}{g} = [002]^*$ only defect C is visible (Figure 15 (g)). Only defect A is in contrast with $\underset{\sim}{g} = [0\bar{2}0]^*$ (Figure 15 (h)), while both A and C are visible with $\underset{\sim}{g} = [02\bar{2}]^*$ (Figure 15(i)).

From the image contrast of these defects, it is apparent that the major displacement vector is along the <100> directions normal to the habit planes. Since A and B have fringe contrast with <111>* diffraction vectors, it may be additionally deduced that the displacement is a fraction of a lattice vector, i.e., $\underset{\sim}{R} = a/x$ <100>, where a is the lattice parameter and x = 2,3,.... However, the exact magnitude of the displacement can not be umabiguously determined from these micrographs. For example, no

fringes are visible with $\underline{g} = \pm$ [$\bar{2}$20]*, so it could be concluded that x = 2 and that they are π faults ($\underline{g} \cdot \underline{R} = \pm$ [$\bar{2}$20]* · a/2 <100> = π). However, since the defects are only 10-35nm in size, they are significantly smaller than one extinction distance for <200>*, assuming behavior similar to pure nickel or nickel-base superalloys [75]. The <220>* extinction distance, ξ_{220}, is approximately 40 nm, which is in good agreement with the values determined from CBMD foil thickness measurements as discussed in the appendix. Thus, if these {100} defects have α-fringes, it is necessary to reduce ξ_g to reveal them.

The WBDF technique is an effective method to decrease ξ_g and thereby increase image resolution [76]. Figure 15 (j) is a WBDF micrograph with $\underline{g}$ = [$\bar{2}$20]* and a deviation parameter, $\underline{s}$, of $\sim$0.17nm^{-1} (c.f. Figure 15 (e)). Under these conditions, the effective extinction distance, ξ_{220}^{eff} is reduced by nearly a factor of ten. Clearly, both fringe contrast and dislocation contrast are visible in defects A and B. Thus, with this additional information, $\underline{b} = \underline{R} \simeq \pm$ a/3<100>. A summary of image contrast of the {100} defects is presented in Table 3.

The remaining determination to be made is the nature of the defect strain field, i.e., whether they are vacancy-or interstitial-type. By using the dislocation-loop analogy, it is possible to differientiate between a local lattice collapse (vacancy-type) or a local lattice expansion (interstitial-type). This is done by employing the inside/outside contrast which occurs for dislocation loops when the diffraction vector is reversed [67-70,77]. Recently, Dahmen [78] and Dahmen, et. al. [73] presented an experimentally simple procedure to interpret inside/outside contrast based on Föll and Wilkens [79] concepts. According to Dahmen

[78], the foil is tilted until the precipitates are edge on (for example, defect A in Figures 15 (g,h)). The foil is then tilted through a large angle towards, for example, the [110] pole (Figure 15 (a-e)). By using $\pm$ g = [$\bar{2}$20]* vectors (Figure 15 (d,e)), loops A and B show inside/outside contrast. (In these micrographs, inside constrast has stronger contrast than the outside, residual contrast). The direction of positive $\underset{\sim}{g}$ is defined [78] as pointing towards the pole where the loops are edge on. Hence, for loop A, positive $\underset{\sim}{g}$ is [$\bar{2}$20]* since it points towards the [100] pole (refer to Figure 16). If the loops show inside contrast when imaged with positive $\underset{\sim}{g}$, they are vacancy-type, whereas if they show inside contrast with negative $\underset{\sim}{g}$, they are interstitial loops. Since defect A has inside contrast (strong contrast) with $\underset{\sim}{g}$ = [$\bar{2}$20]*, it has a vacancy-type strain field. Similarly, B shows inside contrast with $\underset{\sim}{g}$ = [2$\bar{2}$0]* (Figure 15 (e)), which points towards the [010] pole where B is edge on. Again, this is consistent with vacancy-type strain fields.

The above analyses were made by comparing the image contrast of the {100} planar precipitates with contrast behavior of conventional partial dislocations and stacking faults in isotropic f.c.c. materials. For example, the partial dislocations surrounding the {100} faults are invisible with <111>* diffraction vectors, in accordance with $\underset{\sim}{g}.\underset{\sim}{b} = \pm 1/3$ invisibility criteria from contrast theory [67-70]. However, at present, theory does not predict the reversal of fringe contrast observed in Figure 15. This asymmetry was also observed in defects when they were imaged with $\pm$ <111>* diffraction vectors. For example, Figure 18 shows a sample aged at 500°C for 10h imaged with [$\bar{1}$11]*, [1$\bar{1}\bar{1}$]* and [2$\bar{2}$0]* two-beam diffraction conditions. The fault fringes from defects marked A are strong

with $\underset{\sim}{g} = [\bar{1}11]^*$ (Figure 18 (a)) and weak with $\underset{\sim}{g} = [1\bar{1}\bar{1}]^*$ (Figure 18 (b)); defects B have the opposite behavior. Since it was determined that these are vacancy defects, the strong contrast of loop B and weak contrast of loop A with $\underset{\sim}{g} = [2\bar{2}0]^*$ in Figure 18 (c) indicates that A lies on (010) with $\underset{\sim}{b} = \underset{\sim}{R}\ a/3\ [010]$ and that B lies on (100) with $\underset{\sim}{b} = \underset{\sim}{R}\ a/3\ [100]$; c.f. Figure 15 (f). An additional constraint on the fault contrast reversal is that kinematical conditions must exist, i.e., only one Bragg reflection must be strongly diffracting with $\underset{\sim}{s}>0$. Defects imaged in regions of $\underset{\sim}{s}\leq 0$ have "anomalous" contrast such as the two defects near the arrow in Figure 18 (b)). These defects have opposite contrast in Figure 18 (a) and (c). Hence, under kinematical conditions, strong loop and fault contrast results respectively when $(\underset{\sim}{g}\cdot\underset{\sim}{b}) = +2/3$ and when $(\underset{\sim}{g}\cdot\underset{\sim}{R}) = +1/3$ (or $\alpha = +2\pi/3$). Presently, the above "rules" are only a summary of observations, however similar observations have been made previously, and will be compared with the present results in the Discussion chapter.

B. Fine Matrix Precipitates

Another prominent product of the phase decompositions occurring in the quenched/500°-600°C aged stainless steel samples are small (5-10 nm) matrix precipitates. Upon close inspection, these precipitates are observed in nearly all diffraction conditions, although their visibility is enhanced by WBDF imaging; for instance, in Figure 15 (j) for a 600°C/1h sample, and Figure 19 for a 500°C/10h sample. The average density of these precipitates is approximately 10^{16} cm^{-3}, which is an order of magnitude greater than the density of {100} planar precipitates.

A sample aged at 600°C for 1h was imaged at higher magnifications using multibeam conditions near the [100] pole (see Figure 20). The fine

precipitates also appear to be disk-shaped with {100} habit planes. Thus, in this zone, two variants are edge-on, while the face-on variant is visible from residual contrast (marked with arrows). Another important observation is that there does not appear to be any distinct PFZ's around the larger particles. This probably implies that the composition of the smaller particles is different than that of the larger ones.

The CBMD pattern corresponding to this micrograph failed to reveal any precipitate reflections as seen in the inset of Figure 20. However, by employing a slightly slower quench rate followed by aging at 600°C for 10h, diffraction from the precipitates was obtained. Figure 21(a) is a multibeam BF image wth $\underset{\sim}{B}$ = [100] which reveals the small precipitates. With this thermal treatment, the {100} faulted defects do not form. [100] and [110] SAD patterns from this area are shown in Figure 21 (b) and (c). It is evident that the matrix and precipitate patterns have identical symmetry, but differ in size by a factor of three. Thus, three conclusions may be drawn: First, there is a cube-cube orientation relationship, i.e., $(100)_\gamma$ // (100)ppt, $[010]_\gamma$ // [010] ppt. Second, the lattice parameter of the precipitate is approximately three times that of the matrix. Third, the symmetry of the precipitate is probably based on the m3m space group. With this information, the precipitates may be identified as $M_{23}C_6$-type.

C. Coarse Matrix Precipitates

Figure 22 is from a sample aged at 500°C for 100h and shows "coarse" matrix precipitates (arrowed) in addition to the {100} planar faults and fine matrix precipitates. These micrographs are a BF/WBDF pair taken near $\underset{\sim}{B}$ = $[21\bar{1}]$ with g = $[\bar{1}1\bar{1}]^*$; the deviation parameter for the WBDF

image is approximately 0.11 nm^{-1}. The size of these particles is about 45nm by 30nm (projected lengths). They exhibit fringe contrast, but are unusual since the fringes appear to be in two directions. However, it is not possible to extract the habit planes since the image was not taken in the zero-tilt condition.

These precipitates were observed solely in the 500°C/1h specimens. They are qualitatively similar to (albeit, smaller than) the precipitates produced by the double-aged thermal treatment (Figure 31), and are probably a phosphorus-rich phase. Implications of the precipitation of this phase will be presented in the Discussion chapter.

D. Dislocation-nucleated precipitation

Another characterizing feature of the quenched-age alloys is the dislocation-nucleated precipitation. Examples of this mode of precipitation are seen in several of the earlier micrographs, e.g. Figures 13-15. Although it was not always possible to determine the dislocations' Burgers vectors or the precipitates' habit planes uniquely two types of dislocation/precipitate arrays were distinguished:

(1) Precipitation on climbing edge or predominantly edge dislocations, and

(2) Precipitation on screw dislocations which have climbed into helices.

Figures 23-26 provide examples of precipitation on edge or near-edge dislocation. The series of micrographs shown in Figure 23 is from a specimen aged at 500°C for 10h. Figures 23 (a,b) are a BF/WBDF pair with $\underset{\sim}{B}$ = [231] and $\underset{\sim}{g}$ = $[1\bar{1}1]^*$. The deviation parameter used for the WBDF image is 0.13nm^{-1}. Figure 23 (c) shows the dislocation near

B = [111]. The Burgers vector of the dislocation is a/2 [01$\bar{1}$] since the dislocation is out of contrast with $\underset{\sim}{g}$ = [$\bar{1}$11]* and has a double image (indicative of $\underset{\sim}{g}\cdot\underset{\sim}{b}$ = 2) with $\underset{\sim}{g}$ = [022]*. Dislocation segments AB and CD are aligned approximately along [$\bar{2}$20] and are therefore 60° dislocation segments, whereas segment BC is normal to $\underset{\sim}{b}$, and is thus pure edge. Only BC has evidence of precipitation on it with the [231] beam direction. In this orientation, the precipitates appear to be needles rather than discrete particles, even in the WBDF image. As the sample is tilted toward the [111] pole (approximately 35°), the image length of the precipitates decreases. This indicates that the climb plane is perpendicular to (111), and is probably (01$\bar{1}$). Thus, for the pure edge segment, the climb plane is perpendicular to the Burgers vector of the dislocation. The 60° segments appear to have climbed on high index planes.

An example of heterogeneous precipitation on a dislocation of mixed character is shown in Figure 24. The average dislocation direction is [010] near the foil normal, [100]. With this orientation ($\underset{\sim}{B}$ = [100]), the precipitates are nearly parallel to the beam, except for segments near B, see Figure 24 (a,b). As the sample is tilted about the [022]* axis toward [21$\bar{1}$], the precipitate images enlarge. It is also apparent that dislocation segment BC has slipped out of the foil, probably during the thinning of the sample.

From the [$\bar{1}$1$\bar{1}$]* BF image (Figure 24 (c)) the precipitates appear to be discrete particles, which are generally larger near the dislocation. The fringe contrast of the precipitates in Figure 24 (d) (WBDF with $\underset{\sim}{s}$ $\sim$0.11 nm^{-1}) indicates that the precipitates are inclined to the beam direction. These fringes denote the intersection of the precipitates

with the foil surface; their direction is approximately 70° from the $\underset{\sim}{g}$ = $[\bar{1}1\bar{1}]^*$ direction. With this geometry, a possible habit plane for the precipitates, and thus, a possible climb plane for the dislocation is $(11\bar{2})$. This plane does not contain the Burgers vector of the dislocation, $\underset{\sim}{b}$ = a/2 $[01\bar{1}]$.

A variety of dislocation-precipitate configurations are shown in Figure 25. These examples illustrate the difficulties in assigning unique Burgers vectors and climb planes to the dislocations. For example, consider the image contrast of dislocation A. From Figure 25 (a), with $\underset{\sim}{B}$ = [341] and $\underset{\sim}{g}$ = $[\bar{1}1\bar{1}]^*$, this dislocation has an average line direction of a few degrees from $[\bar{1}11]$. In projection, the precipitates are nearly parallel to $[\bar{1}1\bar{1}]$. With $\underset{\sim}{B}$ = [431] and $\underset{\sim}{g}$ = $[\bar{1}11]^*$ (Figure 25 (b)) the dislocation is out of contrast; hence $\underset{\sim}{b}$ = $\pm$ a/2 $[0\bar{1}\bar{1}]$ or $\pm$ a/2 $[\bar{1}01]$. The projected direction of the Burgers vector is marked on Figure 25 (b). Since the Burgers vector is nearly perpendicular to the line direction, dislocation A has a predominantly edge character. A drastic change in image contrast is seen by comparing Figures 25 (c,d). Both micrographs were taken with $\underset{\sim}{g}$ = $[002]^*$ but with a 45° tilt between $\underset{\sim}{B}$ = [130] and $\underset{\sim}{B}$ = [210], Figures 25 (c,d) respectively. Near the [130] pole, the precipitates are small, discrete dots, whereas near $\underset{\sim}{B}$ = [210], they show a more complex contrast behavior.

A further difference in image contrast is due to the magnitude of $\underset{\sim}{s}$ in WBDF conditions, Figure 25 (e,f). Both micrographs were taken with $\underset{\sim}{g}$ = $[00\bar{2}]^*$ near $\underset{\sim}{B}$ = [210], but $\underset{\sim}{s}$ $\sim$0.09nm^{-1} in Figure 26 (e) and approximately 0.11nm^{-1} in Figure 25 (f). The "zig-zag" contrast seen

in the g/2g condition (Figure 25 (e)) is similar to the contrast behavior of certain grain boundaries and mechanical twins in ferroelectric materials such as Pb TiO_3 [81], and arises when a series of lattice displacements are superimposed in the direction of the electron beam. By increasing the deviation parameter such that the g/3g conditions are met, the precipitates appear as elongated white dots. A final difficulty in analyzing dislocation A is that the majority of the dislocation has slipped out of the foil.

The image contrast "anomalies" described for dislocation A also plague the interpretation of dislocation B. This latter dislocation curves from a pure edge orientation to a mixed orientation. This also indicates that there is not a unique climb plane. However, the segment parallel to $[1\bar{1}0]$ has apparently climbed on (001) planes.

Dislocation C is an example of a helical array. The original direction of the screw dislocation was parallel to the Burgers vector. After climbing into a helix, the array consists of a series of prismatic loops on $(01\bar{1})$ or $(10\bar{1})$ planes. Precipitation occurred as the helix expanded.

There are two major conclusions to be drawn from the analysis of the dislocations in Figure 25. First, it is obvious that dislocation climb nucleated the precipitates since only one variant was observed on each dislocation. For example, in Figure 25(b), the dislocations and the precipitates are out of contrast with $\underline{g} = [\bar{1}11]^*$. This behavior may be compared with heterogeneous precipitation on dislocations where in general two variants are observed. Second, it is apparent that climb was not restricted to only one plane. Evidence for this is seen in the change in

projected length of the precipitates along dislocation A, for example, refer to Figure 25 (a). It appears that the precipitates are on a cylinder with the dislocation as the axis: at the top of the micrograph, the precipitates are nearly parallel to the beam. The precipitates spiral in a counter-clockwise direction such that the maximum projection occurs near the middle of the micrograph. The projected length of the precipitates decreases towards the bottom of the micrograph.

Several of the analysis difficulties mentioned above may be overcome by stereo imaging; WBDF stereo pairs are especially helpful. For example, Figure 26 is a WBDF stereo pair from a sample aged at 600°C for 1 hour. The operating reflection is $[\bar{1}11]^*$ with $\underset{\sim}{s} \sim 0.11 nm^{-1}$ for both micrographs. There is approximately 13° tilt between $\underset{\sim}{B} = [110]$ (Figure 26 (a)) and $\underset{\sim}{B} \sim [23\bar{1}]$ (Figure 26 (b)). From diffraction contrast experiments and stereo imaging, the Burgers vector of dislocations A, B and C were determined to be $\pm$ a/2 [011]. Dislocation A has an average line direction of $[\bar{1}10]$; thus, it is of mixed character. The climb plane was determined to be (011).

The line direction of dislocation B curves from $[\bar{1}1\bar{1}]$ (pure edge) to $[\bar{1}10]$ (mixed). This dislocation appears to have climbed on (011) and (111) planes.

Dislocation C is a helix with a [011] axis parallel to $\underset{\sim}{b}$. *The* processes of climb and glide resulted in the formation of prismatic loops on (011) planes. As the helix expanded rows of precipitates formed principally along $[1\bar{1}1]$ and $[1\bar{1}0]$ directions on the loops.

E. Grain boundary denuded zones

Another feature of the quenched / 500-600°C aged samples is the occurrence of denuded regions near grain boundaries. For convenience, these depleted zones will be referred to as precipitate-free zones (PFZ's); this term will also apply to dislocation loop-free zones (LFZ's). PFZ's were observed near the majority of the grain boundaries in the samples subjected to this quench-age thermal treatments. Exceptions were noted however, and these will be dealt with in the concluding paragraphs of this section.

An example of a grain boundary PFZ in a sample aged at 500°C for 10h is shown in Figure 27. The zone half-width (the average value from both sides of the boundary) for the {100} faulted loops is approximately 250 nm. The zone width for the fine matrix precipitates is approximately 100 nm. The different denuded zone widths may be seen more clearly in the WBDF micrographs taken from both grains, Figures 27 (b,c).

The effect of thermal treatment on the width of PFZ's may be seen by comparing Figure 27 with Figure 28. This later micrograph is from a sample aged at 600°C for 1h. WBDF images were not recorded from this area, so a comparison of the PFZ's from both types of defects is not possible. However, the {100} defect PFZ from grain 1 is about 400nm. The effect of the combination of grain boundary and dislocation sinks is clearly seen in grain 2: the denuded region is much larger than in grain 1.

Another factor which may influence the width of the PFZ is grain boundary energy. The boundary energy is a complicated function of the relative misorientation of the grains and of the dislocation substructure

of the boundary itself. As mentioned above, occasionally there are deviations from the average PFZ width for a given thermal treatment. For example, compare the grain boundary in Figure 14 which does not exhibit a PFZ with the boundaries in the two preceeding figures. Consider also Figure 29: this micrograph shows a triple junction in a 500°C/10h aged sample. The PFZ between grains 1-2 and 1-3 are fairly uniform (∿200nm), whereas there is no apparent depleted zone between grains 2-3.

A thorough discourse on grain boundary energies and geometries is beyond the scope of this thesis. The interested reader is referred to the series of articles in Grain Boundary Structure and Kinetics [82] and to theses by R. Gronsky [83], J. Briceño [84], and E. Kamenetzky [85] for further details and references. However, to understand the behavior of boundary 2-3 in Figure 29, a cursory introduction to grain boundary nomenclature is required. For example, the grain boundaries were analyzed by determining axis/angle pairs. This classification describes a common direction in the two grains, and the angle of rotation about that direction. The relationship between the grains may be further classified by considering the superlattice of common lattice points called coincident site lattices (C.S.L.'s). The fraction of lattice points the grains have in common is written as $1/\Sigma$, where Σ is an odd integer.

Experimentally, the axis/angle pair relationships were determined via the procedure outlined by Edington [69]. For the grains in Figure 29, the process involved the following steps:

(1) Grain 1 was tilted into an exact [103] zone axis orientation, and the diffraction conditions for the three grains were recorded.

(2) The sample was then tilted such that grain 1 had a [001]

orientation (an 18.4° tilt about the [020]* diffraction vector). The diffraction patterns from this orientation were again recorded.

(3) The diffraction patterns were consistently indexed and analyzed to obtain the precise beam directions. These analyses were greatly facilitated by the combined use of: (a) CBMD to provide Kikuchi lines from relatively thin areas, and (b) a small camera length (280mm) to allow a large angular view of reciprocal space ($\sim$0.3 rad). See the appendix for further discussions of CBMD.

(4) The axis/angle paris corresponding to the beam direction pairs were obtained from a computer program courtesy of E. Kamenetzky.

(5) The axis/angle pairs were then compared with tables of C.S.L. relationships [86].

The diffraction patterns from the grains are shown in Figures 29 (b-d).

The relationship between grains 1-2 is [$\bar{2}\bar{3}5$]/21.09° which is not near any Σ value, i.e., it is a high angle, disordered grain boundary. The axis/angle pair for boundary 1-3 is [032]/51.87° which is 3° away from a Σ=77c boundary, and is thus also disordered. Grain boundary 2-3 is described as [$\bar{1}$13]/145.68°, which is one description for a Σ=3 incoherent twin boundary (refer to Table 2 of Mykura's article [86] for a complete enumeration of relationships for Σ=3 boundaries). The implications of special grain orientations on the width of PFZ's will be discussed further in the Discussion chapter.

4.2.2. Aging at 600°C/10h and at 700°C/1h

Samples aged at 600°C for 10h and at 700°C for 1h show dramatically different microstructures than the previously discussed thermal treatments. There were no dislocation loops or precipitates observed in these samples; only perfect dislocations and dislocation tangles were evident as seen in Figure 30. These scattered dislocations did not appear to be decorated with precipitates.

4.2.3. Aging at 500°C/10h plus 700°C/24h

The microstructure of a double-aged sample (500°C/10h followed by 700°C/24h) is shown in Figure 31. This is a multibeam BF image with $\underset{\sim}{g}$ = [100]. The main products of the thermal treatment are intragranular needles and laths. The needles lie in <100> directions while the laths have {100} habit planes with <100> directions.

CBMD experiments were performed to determine the crystal structure of these precipitates. Examples of the CBMD patterns from a lath with a (010) habit plane are shown in Figure 32. Figures 32(a), (b) and (c) are respectively [010], [110] and [310] reciprocal lattice sections of the phosphide precipitate. The [010] pattern shows that there is complete ordering in the (010) plane. There is no spot splitting in the [002]* direction, therefore, the (001) precipitate planes are coherent with the matrix. Along the [200]* direction, there is a mismatch of less than 0.7%; thus, the (100) precipitate planes are nearly coherent. The precipitate reflections have a two-fold symmetry in the [010] pattern compared to the four-fold symmetry of the matrix reflections. Hence, the highest symmetry the precipitate could have is based on the tetragonal Bravais lattice with $a_p = b_p \neq c_p$. From the [010] pattern, $a_p = 2a_o = 0.72$ nm

and $c_p \sim 3a_o \sim 1.08$ nm with a c/a ratio of ~1.5. In the [110] reciprocal lattice section, the precipitate reflections have the same symmetry as the matrix pattern. Note the streaking perpendicular to the [002]* direction. The <220>* precipitate reflections occupy non-rational positions; i.e., they are not at $\pm$ 0.5 [2$\bar{2}$0]* matrix positions, but rather, are displaced inwards by approximately 2%. This displacement is significantly larger than expected from the 0.7% mismatch in the [010] pattern. In the [310] pattern, the precipitate reflections that are perpendicular to the [002]* direction are also in non-rational positions. The streaking has increased in length consistent with a nearly edge-on plate.

While a complete reciprocal lattice unit cell could not be fully determined, these patterns were sufficient to allow a tentative construction to be made, and this is shown in Figure 32(d). To be consistent with the incommensurate positions of the precipitate reflections, the [020]* precipitate repeat distance is correspondingly ~5% smaller than the matrix reciprocal distance. As drawn, it is a body-centered orthorhombic unit cell (in reciprocal space). Additional CBMD patterns are required for a complete analysis.

4.3 Direct Quench

Specimens were directly quenched from 1150°C to 500°C and aged for 10h. Figures 33-35 are examples of the microstructures produced from this thermal treatment. Figure 33 is a diffraction contrast series in which $\underset{\sim}{B} \sim$[110] for micrographs a-d, and $\underset{\sim}{B} \sim$[100] for e-h. The purpose for this series was to determine the habit planes, displacement vectors and the nature of the defects. Using $\underset{\sim}{g} = [1\bar{1}1]$* (Figure 33 (a)), three variants

of the small defects were visible, marked A, B and C. These precipitates were approximately 12.5nm in diameter and had fringe-type contrast. There are also several larger (~80nm in diameter) defects visible which have complicated geometries and contrast behvaior. With the $[1\bar{1}1]^*$ reflection, loops D, E and F are in strong contrast. In Figure 33(b) with the $[002]^*$ two-beam imaging condition, defects A and B are out of contrast, while C is on edge perpendicular to $\underset{\sim}{g}$. Defects D, F, G, and H are also visible with the $[002]^*$ reflection. A BF/WBDF pair using $\underset{\sim}{g} = [1\bar{1}\bar{1}]^*$ is shown in Figure 33 (c,d); for the WBDF, $\underset{\sim}{s}$ is slightly positive of 3g, and equals 0.1 nm^{-1}. With these imaging conditions, defects A,B,C,E,G and H are in contrast. The WBDF illustrates the fringe contrast of A and B, and the absence of fringes in the larger loops. A 45° specimen tilt about the $[00\bar{2}]^*$ axis changes the image width of the defects, for example, compare defect G in Figures 33(b) and (e). Imaging with the $[0\bar{2}2]^*$ diffraction vector, A and C are on edge at 45° to $\underset{\sim}{g}$, and of the larger loops, only F is out of contrast (Figure 33 (f)). Within some of the larger loops, there are small particles which appear to lie on {100} planes; for example, see loop E and H. The two remaining micrographs in this figure are a $\pm [020]^*$ pair (Figure 33 (g,h)) in which defects A, E, F and G are in contrast. (These micrographs are smaller due to a slight difference in imaging area for Figure 33 (g). Defects F and G are clearly visible on the negative of Figure 25 (h), whereas loop H is out of contrast). Defect E has inside contrast with $\underset{\sim}{g} = [0\bar{2}0]^*$ and outside contrast with $\underset{\sim}{g} = [020]^*$. Since this loop is nearly edge-on in Figure 33 (a), the $[0\bar{2}0]^*$ vector is +g for loop E usi[illegible] definitions discussed in conjection with Figure 15.

The contrast behavior of these defects are summarized in Table 4. Defects A, B and C have {100} habit planes with a/x <100> displacement vectors. The value of "x" may be determined from the BF/WBDF [220]* pair in Figure 34. The deviation parameter of the WBDF micrograph is $\sim 0.21 nm^{-1}$, corresponding to a $\underset{\sim}{g}/3\underset{\sim}{g}$ diffraction condition (for 120keV electrons). In these micrographs the beam direction is near [110]. Two variants of the {100} defects are visible, and display dislocation and fringe contrast (evident in the WBDF). Thus, these defects are similar to those analyzed in Figure 15 with $\underset{\sim}{b} = \underset{\sim}{R} \sim a/3$ <100>. The larger defects D-H lie on {110} habit planes with perpendicular displacement vectors. Since fringe contrast is not detected in BF or WBDF images, the defects are prismatic loops with $\underset{\sim}{b} = a/2$ <110>. From the inside/outside behavior of loop E (inside contrast with $+\underset{\sim}{g}$), it may be concluded that it has a vacancy-type strain field. (It should be noted that the image shift of loop E with $\pm$ [020]* is not large since $\underset{\sim}{g}.\underset{\sim}{b} = \pm 1$).

The internal structure associated with the {110} loops apparently follow similar visibility rules as the loops. However, since these particles appear to have {100} habit planes, they could have a/x <100> displacements. It was also observed that loops with $\underset{\sim}{b} = a/2$ [110] have (010) particles associated with them. For example, the particles within loop E ($\underset{\sim}{b} = a/2$ [1$\bar{1}$0]) lie on (010) planes; loop H ($\underset{\sim}{b} = a/2$ [10$\bar{1}$]) encloses (001) particles. It must be stressed, however, that the overlapping strain fields of the loops and particles hampers more exact characterization of the particles.

The grain boundary in Figure 33 does not have a well-defined PFZ; in addition, loops have formed on the boundary. Other grain boundaries,

however, show very distinct denuded zones, for example see Figure 35. The PFZ's between grains 1-2 and 1-3 have a uniform width of approximately 170nm, while defects have precipitated on boundary 2-3. This behavior is similar to that observed in Figure 29. However, since the axis/angle pairs were not determined for the grains in Figure 36, correlations between zone widths and boundary types can not be made.

5.0 Discussion

The main objective of this thesis, as explained in the introduction, was to study the precipitation reactions and their relation to lattice defects in a bcc Fe-Si-C alloy and in a fcc phosphorus-containing stainless steel. Of major interest was to determine the extent of vacancy involvement in the phase decompositions of these commercial-quality alloys. The microstructural responses to thermal treatments were detailed in the previous chapters. Thus, the purpose of this chapter is to discuss these results, mindful of the comparative nature of this investigation.

The phase transitions exhibited by these iron-base alloys are qualitatively similar to those occurring in many age-hardenable alloys. After suitable quench-age treatments, common microstructures observed in these systems include:

- homogeneous dispersions of coherent or semi-coherent plate-shaped precipitates (or pre-precipitates)
- {100} habit planes with orthogonal displacement vectors
- precipitate-free zones near dislocations and grain boundaries
- precipitate densities related to excess vacancy concentrations

Many investigators have attributed these features to the involvement of quenched-in vacancies (see, for example, the articles in reference 87). The same conclusion is drawn in the present study. However, since the effects of vacancies are manifested in a variety of ways, it is not immediately obvious what the total extent of vacancy involvement is. Therefore, in order to facilitate the interpretations of the precipitation reactions in the two steels under present investigation, it is advantageous to review the known effects of non-equilibrium vacancies.

5.1 The Roles of Excess Vacancies in Precipitation Processes

There are four effects of excess vacancies regarding precipitation reactions; three of them deal primarily with the kinetics and thermodynamics of the phase decompositions, while the fourth assumes a structural role. One effect of excess vacancies is to increase the rates of precipitation from solid solution. Rosenbaum and Turnbull [88] used this concept to interpret the rapid kinetics of precipitation in Al-Si alloys. A related phenomenon is the role of vacancies in zone formation. Federighi and Thomas [89] proposed that the kinetics of G.P. zone formation in Al alloys can be explained on the basis on non-equilibrium concentrations of vacancies. The differences in cluster kinetics were discussed in terms of the variation in solute-vacancy binding energies. Thus, these effects are due to enhanced solute diffusivities: since metallic diffusion occurs by vacancy exchange, an increase in vacancy concentration creates a concomitant increase in substitutional solute migration rates.

A second vacancy effect is to lower the nucleation barrier for homogeneous incoherent precipitation [90,91]. Russell [91] considered the driving force for nucleation of a second phase with a large misfit in the matrix. The driving force equation he derived included a term to account for the number of vacancies required for stress-free transformations, and inherently assumes that the vacancies are destroyed to accommodate the new phase. This model adequately describes the precipitation behavior in several systems [62,91].

A third method of vacancy-assisted precipitation assumes that only a "few" vacancies are required to nucleate the phase, and the vacancies

are not consumed in the reaction. The basic concepts of this method were outlined by Vyhnal and Radcliffe [25] for carbide precipitation in ferrite, and will be discussed in more detail in the following section.

The fourth role of vacancies is apparent in a recently developed structural model [92,93]. This mechanism was originally proposed by Westmacott and Perez [93] to explain the carbide precipitation in quenched Pt. The premise of this model is based on a strong V-C binding energy and the accommodation of oversized solute. The authors propose that V-C complexes form during the quench; once formed, these complexes migrate as an entity and condense into planar arrays on {100} planes. From a hard sphere model, the proposed lattice displacement of the initial collapsed V-C clusters is ~0.3a (where a is the lattice parameter of Pt). The open structure of the {100} stacking fault accommodates the oversized carbon and provides the correct stacking for subsequent carbide formation. This is in good agreement with the diffraction contrast experiments. More recently, these ideas have been extended to explain the observations in bcc Ta-C [72, 93] and in fcc substitutional solutions [93].

Logically, the third model may also be considered to be a structural mechanism; however, there are subtle, yet distinct, differences between the two which should be appreciated. For instance, in the structural model, it is assumed that the vacancies partially collapse to accommodate the solute atoms, thereby forming the nucleus of a second phase. Note that this is different from Russell's total collapse mechanism as well as the mechanism proposed in the third model. Furthermore, for the vacancies to be structurally incorporated in the phase, it is obvious that locally there must be a sufficiently high vacancy concentration. Once these sheets

of vacancies have relaxed, their individual identities are lost; this is in contrast to the assumptions of the third model. The similarities and differences in the four models will be amplified in the discussions of the following sections.

Since the key to the co-precipitation models is the association of vacancies and solute atoms, it is instructive to understand what effects solutes have on vacancies. From a theoretical study, Wert [94] concluded that solute effects are more pronounced under the following conditions:

(i) relatively slow quench rates

(ii) high sink densities

(iii) high solute concentration

(iv) high absolute energy of vacancy formation (E_V^F)

(v) low relative vacancy migration enthalpy (E_V^M/E_V^F)

(vi) high relative vacancy-solute binding enthalpy (E^B/E_V^F)

When these conditions are met, the concentration and lifetime of quenched-in vacancies are increased. These excess vacancies may then participate in the precipitation reactions as described previously. Since available data indicate that these conditions are applicable to the alloys in the present investigation, it is expected that solute-vacancy interactions will be of major importance. Therefore, with these general considerations as background, the specific details of the precipitation processes in the Fe-Si-C and stainless steel will be presently discussed.

5.2 Precipitation in the Fe-Si-C Alloy

In the Fe-Si-C alloy, quenching from the ($\alpha+\gamma$) region produces a supersaturation of carbon in the ferrite as illustrated in Figure 1 (a). After aging at room temperature for one week, high densities of small

precipitates are observed (Figure 2). Based on the previous discussions of vacancy-assisted precipitation, an obvious question to ask is: To what extent do vacancies participate in the precipitation of carbides? To answer this question, it is first necessary to estimate the concentration of vacancies at the quench temperature, $C_V(T)$. Since it has been established that a strong V-C binding energy does exist [19, 22,23], the Lomer equation [2] will be used to calculate $C_V(T)$:

$$(1)\quad C_V(T) = A\exp\left(\frac{-E_V^F}{kT}\right)\left\{1-ZC_s + ZC_s \exp\left(\frac{E^B}{kT}\right)\right\}$$

where A is an entropic factor taken equal to one

E_V^F is the enthalpy of vacancy formation; 1.5 eV [95]

E^B is the vacancy-solute binding energy; 0.4 eV [17]

Z is the number of interstitial sites near a vacancy (since C occupies octahedral sites, Z=6)

C_s is the solute concentration

Without V-C interactions, the equilibrium concentration of vacancies is $C_V^o(T)$:

$$(2)\quad C_V^o(T) = A\exp\left(\frac{-E_V^F}{kT}\right)$$

Thus, the bracketed term in equation 1 represents the increase in vacancy concentration due to V-C binding. Other useful quantities are the concentration of bound V-C pairs, C_B, and the ratio of bound to free vacancies, C_B/C_V^o.

$$(3)\quad C_B = C_s \exp\left(\frac{E^B-E_V^F}{kT}\right)$$

$$(4)\quad C_B/C_V^o = \frac{ZC_s}{1-ZC_s}\exp\left(\frac{E^B}{kT}\right)$$

It must be stressed that equations 1-4 are merely estimates. Application of the Lomer model to a two-phase, multicomponent system must be justified by several assumptions. Firstly, it is assumed that C_V in the α-phase is independent of C_V in the γ-phase. Secondly, it is assumed that no gross substitutional solute segregation occurs between the two phases. Koo, et al. [96] measured the aluminum concentration across a martensite/ferrite boundary in an Fe-1Al-0.1C dual phase steel. They found that Al preferentialy partitions to the ferrite grains. In contrast, no partitioning of Si was observed in the present Fe-Si-C alloy [37]. Additionally, it is assumed that during the two-phase annealing an equilibrium concentration of carbon is obtained. (Annealing times of 1 hour were used to assure this). Furthermore, it is assumed that the quench is sufficiently rapid to prevent massive segregation of carbon from α to γ. Thus, the concentration of carbon in ferrite may be approximated from a psuedo-binary phase diagram, shown in Figure 36. For a quench from 850°C, C_s $\sim$0.015% ($\sim 7 \times 10^{-4}$ atomic fraction). Substituting this value into equation 1, C_V (850°C) $\sim 2.4 \times 10^{-7}$, which corresponds to $\sim 2 \times 10^{16}$ vacancies per cm^3. The ratio of bound vacancies to free vacancies (C_B/C_V^o) at the quench temperature and at room temperature (equation 4) are:

$$\frac{C_B}{C_V^o}\,(850°C) = 0.3; \quad \frac{C_B}{C_V^o}\,(25°C) = 5.5 \times 10^4$$

Hence, at 850°C, the increase in the number of vacancies is negligible. However, the ratio of 25°C indicates that nearly all of the quenched-in vacancies are paired with carbon atoms. Furthermore, these ratios indicate that due to the pairings there is no significant vacancy loss during the quench.

The calculated concentration of vacancies, C_v, agrees well with the density of precipitates after room temperature aging for 1 week ($\sim 7 \times 10^{15}$ cm^{-3}). Vyhnal and Radcliffe (VR) [25] also observed that the concentration of vacancies is similar to the density of precipitates. They quenched an Fe-0.019%C steel from 710°C and aged it at room temperature for approximately 1000h. This treatment produced a precipitate density of $\sim 10^{15}$ cm^{-3}. The estimated vacancy concentration for their conditions is C_v (710°C) $\sim$ 3.5×10^{-8}, which corresponds to $\sim 3 \times 10^{15}$ vacancies per cm^3. Thus, with similar E^B, carbon contents and quench rates, the density of precipitates is greater in the Fe-Si-C alloy of the present investigation. It appears that the density difference is due to the order of magnitude increase in retained vacancies.

These comparisons lend further support to the precipitation model proposed by VR. They suggest that carbide nucleation occurs because the interaction between the strain field of a V-C complex and freely migrating interstitial carbon atom results in the formation of a critical sized vacancy/carbon cluster.

The other results obtained for the Fe-Si-C alloy may also be explained by the VR nucleation model. For example, pre-aging at room temperature allows the maximum number of V-C complexes to nucleate the carbides; further growth of the precipitates occurs at 100°C, Figures 3-6. This results in a precipitate density comparable to that in Figure 2. An indication that nucleation is difficult at 100°C is clearly shown in Figures 7-8; the density of the larger precipitates is only $\sim 10^5$ cm^{-3}. As the aging temperature is further increased to 170°C, precipitates have nucleated primarily on dislocations and grain boundaries,

Figure 9. These results are in agreement with earlier studies of Fe-C systems [13,25]. From solid-solid nucleation theory (e.g. reference 97) these observations indicate that the size of the critical nucleus increases with increasing aging temperature. Thus, the nucleation sites which are responsible for the high precipitate densities at room temperature are not available at the higher temperatures.

It may now be concluded that vacancies are likely to be involved in the nucleation of the carbides. From Wert's [94] criteria, it appears that the Fe-Si-C system is able to retain a large portion of the high temperature vacancies during the quench due to V-C binding. These V-C complexes attract migrating free carbon atoms to form the critical nucleus of a carbide. The C_V estimates indicate that single vacancies are associated with the carbide nucleus. Again, it is stressed that while this is not a true structural mechanism, it may be considered as an extreme case in which the lattice pertubation associated with the vacancy nucleates the new phase.

This limited degree of vacancy involvement is also consistent with the interstitial-type strain field of the precipitates (Figure 6). Similar observations were made for carbides in Ta-C [72], which cast doubts on the report of vacancy-type strain fields in the precipitates formed in the Nb-containing dual-phase steels [32]. As noted earlier, a minimum of three micrographs are required to determine the strain field of a defect by inside/outside image shifts. It is of paramount importance to establish unambiguously the habit plane of the precipitates. Consequently, the strain fields could not be determined for the precipitates in Figure 4; similarly, the information provided by Figure 3 in reference 32 is

insufficient for such a determination. Conversely, it is likely that they are interstitial-type as expected from precipitates of increased atomic volume.

Thus far it has been demonstrated that vacancies could assist in the nucleation of the carbides; a more detailed consideration of the precipitation model suggests that the vacancies could also participate in the growth of the precipitate. Earlier it was stated that the vacancies are probably not consumed in the nucleation reaction. This is supported by PAS experiments which indicate that at higher temperatures ($\lesssim$200°C) there is an increase in the free vacancy concentration [22]. These observations suggest that the vacancies dissociate from the carbon clusters at these higher temperatures. Therefore, it is possible that the vacancies aid in the growth of the carbides prior to high temperature dissociations.

However, as discussed in the Introduction, there is no firm evidence in the literature which uniquely determines the crystal structure of the incipient carbide in α-iron. From lowest energy criteria, it is possible that the initial carbide structure is closely related to bcc ferrite. The diffraction contrast behavior of the precipitates in Figure 8 also suggests that the displacements of the smaller particles is different than the larger ones. It is proposed that the small carbides exert pure orthogonal displacements, while the large precipitates may have an additional shear component.

Computer modelling studies of carbon clustering in α-iron also suggest that the initial carbide structure may be bct (isomorphous with α") rather than hcp (ε-carbide) [98]. For these reasons, the growth mechanism of an α" precipitate is treated.

A process whereby a unit cell of α" could be nucleated by a V-C complex can be readily seen by reference to Figure 37. In this figure, the open circles represent Fe (or Si) atoms, and the smaller closed circles denote carbon and/or nitrogen atoms. The bct unit cell of α" is composed of eight slightly distorted unit cells of bcc α-iron; the c/a ratio for this structure is 1.10 [99]. Let the V-I complex occupy the center position of the eight unit cells that subsequently become the α" cell. If 4 freely migrating solute atoms (carbon or nitrogen) become bound to the complex, the atom relaxation around the vacancy can lead to a structure closely resembling the bct structure. Its complete formation requires that the vacancy undergoes a minimum of 2 nearest neighbor jumps to the center position of an adjacent 8 cell bcc unit. The tensile stress in the surrounding matrix due to the precipitate cell expansion will favor this process. The advantage of this model is that the process can continuously repeat itself as further mobile solute atoms become bound to the vacancy. This mechanism could operate only if the vacancies do not become structurally incorporated within the phase.

To determine whether this proposed carbide growth process is valid, it may be mathematically modelled with appropriate values of diffusivities and activation energies. In general, diffusion-controlled precipitate growth follows a parabolic growth law, i.e.,

$$(5) \quad r = \beta(Dt)^{1/2}$$

where r is the growth distance; here the precipitate diameter

β is a function of the supersaturation

t is the time

D is the characteristic diffusivity; of the form

(6) $D = D_o \exp(-Q/kT)$

In the present model, both vacancy and solute migrations are necessary for precipitate growth. If the rate-controlling step is the vacancy migration, then the pre-exponential term (making the simplest assumptions) is given by

(7) $D_o = 4/3\ a^2 \nu_o \exp(\frac{Sm}{k})$

where a is the ferrite lattice parameter (0.2866nm), ν_o is the jump frequency (10^{13} sec^{-1}) and Sm is the entropy of migration. For these calculations, it is assumed that the entropic term is unity.

The activation energy, Q, characterizes the vacancy jumps in the local solute-rich environment, and is of the order $(E_V^M + E^B)$. Unfortunately, the values of E_V^M and E^B are quite controversial for the Fe-C and Fe-N systems [95]. Nevertheless, if Q is 0.9eV (0.5+0.4), the precipitate diameters predicted after 168 and 1000h aging at room temperature are 19 and 47nm respectively. These diameters are in good agreement with the observed values (Figure 2 and reference 25). This model additionally predicts that after 1h aging at room temperature the precipitates consist of only 2-3 units cells of α''. The lack of visible precipitates in Figure 1(a) can thus be explained.

Conversely, if precipitate growth is limited by carbon migration, the characteristic diffusivity is [100]:

(8) $D_C = 2 \times 10^{-2} \exp(\frac{-0.86eV}{kT})\ cm^2 sec^{-1}$

substituting equation 8 into equation 5 gives 57 and 140nm respectively for the 168 and 1000h aging. While the vacancy-limited model predicts more realistic precipitate diameters, it is realized that the application

of these diffusivity equations is near the limits of reliability. However, the proposed growth model is a logical extension of VR's [25] nucleation mechanism. Additionally, the similarities in the activation energies (0.9 compared to 0.86 eV) further suggests that vacancies may play a role in equilibrium interstitial diffusion.

Thus, from the above discussions, it may be concluded that the incipient carbide structures form through the aid of vacancies. Due to the limited number of vacancies, the most realistic mechanism for vacancy-assisted precipitation in this system is that proposed by VR [25]. In agreement with their model, the concentration of quenched-in vacancies corresponds to the volume density of precipitates in the ferrite of the dual-phase steel aged at room temperature. It was therefore suggested that single vacancies are sufficient to nucleate the new phase. In an extension of this model, it was proposed that growth of a bct interstitial phase is limited by vacancy migration.

In the next section, the precipitation reactions in the phosphorus-containing stainless steel are discussed. It is shown that the above model is also consistent with $M_{23}C_6$-type precipitation in the austenite, whereas a structural mechanism is proposed for the {100} vacancy defects.

5.3 Precipitation in the Fe-Cr-Ni-P-C Alloy

The precipitation behavior of the phosphorus-containing stainless steel will now be discussed. In the furnace-cooled (~3°C/min) samples, no precipitation or voids were observed, Figure 10. Stainless steels with similar compositions and thermal treatments have shown intergranular fracture, which was attributed to an enrichment of P at the grain

boundaries [101]. Similarly, slowly cooled Ni-base alloys (Monel 400) showed an enrichment of P at grain boundaries by Auger Spectroscopy [102]. These examples suggest that the quench rate for the sample in Figure 10 was slow enough to permit solute and vacancies to migrate to sinks. Unfortunately, the thermodynamic and kinetic properties of phosphorus in austenitic alloys are not known with certainty. Guttmann and McLean [101] propose that additions of Cr and Ni decrease the solubility of P in γ-Fe. Goldstein, et al. [103-106] have tabulated data concerning the Fe-Ni-P system; in particular, Doan and Goldstein [103] and Romig and Goldstein [106] have determined isothermal sections of the ternary phase diagram between 300 and 1100°C. For the present purposes, data for the Fe-35Ni-P sections were extrapolated from the above references and are presented in Figure 38. This composition was selected since it remains austenitic to ~400°C, below which the α-phase becomes metastable. This diagram illustrates a terminal solid solution which is typical of other age-hardening systems. While it is recognized that the absolute limits of P solubility may be different in the 18Cr-10Ni alloy, the $\gamma/\gamma + M_3P$ solvus in Figure 38 is in good agreement with the temperature range of phosphide precipitation observed in earlier studies [60,61]. Carbon also has limited solubility in stainless steel; at 800°C the solubility is ~0.2% and drops rapidly with decreasing temperature [7]. Thus, both carbon and phosphorus will be supersaturated in rapidly quenched samples (Figure 11).

The intrinsic-type defects observed in the 500-600°C aged samples demonstrate that vacancies are also retained in supersaturated concentrations by rapid quenching.

Thus, since both vacancies and solute are supersaturated, it is likely that they precipitate together (i.e., co-precipitate). This hypothesis will be examined in the following sections. Section A will discuss the precipitation of the {100} loops; Section B discusses the fine matrix precipitation; Section C presents the discussion of precipitation on dislocations, the defects produced by the direct quench are discussed in Section D; followed by the implications of grain boundary denuded zones in Section E and the precipitation of phosphides in Section F.

A. Precipitation of {100} Faulted Loops

From diffraction contrast analysis of the {100} loops (e.g., Figures 17, 25 and Tables 3, 4) it was shown that the defects have $\underset{\sim}{b} = \underset{\sim}{R}oa/3$ <100> and vacancy-type strain fields. This particular defect is unusual in fcc materials and has been observed only once previously [92]. The usual mode of vacancy precipitation is condensation on {111} planes. The resulting Frank dislocation loops change the plane stacking from ABCABC to ABABC maintaining a close-packed, low-energy configuration. In contrast, the {100} stacking fault is a high energy arrangement analogous to AA stacking. Thus, the formation and stability of these high-energy faults may be rationalized if it is assumed that they consist of both vacancies and solute atoms. In order to develop this hypothesis further, it is necessary to demonstrate that the characteristics of the loops are consistent with vacancy-solute co-precipitation. To this end, a comparison may be made between the theoretical concentration of vacancies at 1150°C and the density of vacancies calculated from the defects. $C_v(T)$ is evaluated from equation 1 using the following data:

E_V^M = 1.4eV [64]

E_B = 0.5eV [66] (as a lower limit for V-P binding)

$C_S = 5.5 \times 10^{-3}$

Thus, C_V (1150°C) = 5.5×10^{-5}. In Figure 15, the density of {100} faulted loops is $\sim 10^{15} cm^{-3}$, the mean loop radius is ~15nm, the displacement vector is $\sim a/3\langle 100\rangle$ and the area density of the atoms on {100} is $15nm^{-2}$. Therefore, the average vacancy concentration per defect is:

$\pi * (15nm)^2 * 15nm^{-2} = 10^4$ or 10^{19} vacancies per cm^3. The experimentally determined vacancy concentration is:

$$10^{19} \frac{\text{vacancies}}{cm^3} * \frac{(0.36nm)^3/\text{unit cell}}{4 \text{ atoms/unit cell}} * 10^{-21} \frac{cm^3}{nm^3}$$

$= 2 \times 10^{-4}$. This is in good agreement with the theoretical vacancy concentration at the quench temperature.

The following precipitation scenario may thus be evisioned: During the quench, vacancies will be redistributed between solute and solvent atoms. From equation 4,

$$\frac{C_B}{C_V^o}(1150°C) = 4 \text{ and } \frac{C_B}{C_V^o}(25°C) = 2 \times 10^7,$$

indicating that at room temperature nearly all the vacancies are associated with phosphorus atoms. This is feasible since the ratio of solute to vacancies, C_S/C_V (1150°C), ~100. Once V-P complexes are formed, the migration of the bound vacancy is no longer by random movements, but rather is correlated with the phosphorus atom. For the vacancy to migrate independently of the solute, the 0.5-0.8eV [66] binding energy must be overcome. Thus, these complexes migrate as entities

and co-precipitate at grain boundaries, dislocations and "homogeneously" within the matrix. The configuration of the a/3 [100]/(100) defects are consistent with a collapsed sheet of vacancies stabilizing a layer of phosphorus atoms, see Figure 39.

This interpretation of the precipitation events is analogous to the structural model proposed for Pt-C [92]. That the supersaturated stainless steel apparently decomposes in a similar manner to the quenched Pt demonstrates the general applicability for the co-precipitation structural model [93]. However, it is surprising that the initial precipitates are identical for carbon in Pt and for phosphorus in austenite. In the former case, theoretical [24] and experimental [92] studies suggest that the carbon atoms are displaced from the vacancy prior to precipitation and assume substitutional positions only when the vacancies collapse. From X-ray diffraction lattice parameter measurements [53,58], it is generally conceded that phosphorus occupies a substitutional position in austenite, although others [56] found that their results are consistent with interstitial positions.

The Goldschmidt radius of phosphorus is 0.115nm which is 0.9 of the nickel radius. In comparison, the ratio of carbon to nickel is ~0.62. However, Goldschmidt [39] suggests that phosphorus is a "semi-interstitial" element in transition metal alloys, implying that it may act as an interstitial and/or a substitutional atom. Furthermore, the Goldschmidt radii are valid only at room temperature, which suggests that there may be a tendency for substitutional behavior at low temperatures and increasing interstitial behavior at higher temperatures. Several characteristics of P support this hypothesis: (a) Phosphorus has an unfilled 3d-band (neon core plus

$3s^2$, $3p^2$); therefore, it is possible that the atom is more compressible than Fe, Cr and Ni which have 5, 6 and 8 electrons in the 3d shell respectively. This argument has been previously used to explain the accommodation of elements in Ni_3X compounds [107]. (b) The diffusivity of phosphorus is faster than the other major components of stainless steel. The diffusion paremeters for Fe [108], Ni [109] and Cr [109] in an Fe-20Cr-25Ni alloy and for Ni [104] and P [104] in a Fe-12.5Ni-0.3P alloy are given in Table 5. Of particular interest are the diffusivities at 500°C, P is 1-3 orders of magnitude faster than the other elements listed. Again, it is realized that the diffusivity of phosphorus may be different in Cr-bearing stainless steels although the values are valid for the present comparative purposes. (c) There are indications that P may become "gaseous" at high temperatures. Elemental (red) P sublimes according to the following reactions [110].

$$P(s) \rightarrow P\ (g,\ 1atm) \qquad \Delta H_V = 79{,}778$$

$$P(s) \rightarrow 1/2P_2\ (g,\ 1atm) \qquad \Delta H_V = 21{,}328$$

$$P(s) \rightarrow 1/4P_4\ (g,\ 1atm) \qquad \Delta H_V = 7{,}678$$

where ΔH_V is the heat of vaporization in cal/mole and the subscripts s and g signify solid and gas phases respectively. Additional data [110] indicate that the total vapor pressure for these reactions increases from 10^{-9} atm at 80°C to 1 atm at 430°C. Moreover, in solution, P lowers the liquidus and solidus temperatures of Fe-Ni-P alloys [103]. Taking all of these factors into consideration, the similarity between the {100} defects in Pt-C and the austenitic steel are not unreasonable. Furthermore, it is possible that all of the conflicting data on P (i.e., whether it is substitutional or interstitial) could be due to the very strong binding

to vacancies. Thus, it would be basically interstitial, but would increasingly bind to vacancies at lower temperatures and would eventually "occupy" the vacancy, i.e., become substitutional. In this way, the {100} defects form by the structural model, but the phosphorus atoms may occupy the vacancies earlier than carbon in Pt. In addition, since there are several structures of phosphorus in the vapor phase, it is likely than the solid phase is equally complicated.

The {100} secondary defects observed in present investigation are qualitatively similar to those obtained by Rowcliffe, et al. [60,61] with two major exceptions. First, by direct quenching from 1100°C to 500°C and aging up to 50h, they observed vacancy-type loops on {100} but with $\underset{\sim}{b} \sim a\langle 100\rangle$. The assignment of this Burgers vector was due to the lack of visible fringes inside the loops. However, there are three factors which indicate that Rowcliffe's defects may also have $\underset{\sim}{b} = \underset{\sim}{R} \sim a/3\langle 100\rangle$.

- From earlier discussions (and the appendix), it was shown that the <220>* extinction distance is less than the loop diameter. Therefore, fringes may be seen only with aid of WBDF diffraction conditions.
- With <111>* reflections the a/3<100> loops are invisible since $(\underset{\sim}{g}\cdot\underset{\sim}{b}) = 1/3$. However, the fault fringes are visible under these conditions since $\alpha = \frac{2\pi}{3}$. The defects shown in Figure 2 of reference 61 appear to be identical to those in this study, i.e., only fringe contrast is visible with <111>* vectors.
- It was originally thought that the discrepancy between the magnitude of the displacement vectors was due to the difference in the thermal treatments. However, in the present study, direct

quenching also produced a/3<100> loops as seen in Figures 33 and 34.

Hence, it is likely that Rowcliffe's {100} loops are identical to those in this investigation.

Although it may appear to be an insignificant difference, the correct assignment of the lattice displacements is important in unveiling the most probable mechanism of precipitation. For instance, it has been shown that the a/3<100> configuration is in harmony with the proposed sequence of precipitation based on a high V-P binding energy and precipitation of V-P complexes. Rowcliffe also recognized that a strong binding energy exists, but suggested that its main effect would be to increase the equilibrium vacancy concentration. Consequently, it was proposed that the defects are formed by phosphorus segregation to the loops. Alternatively, they suggest that single or groups of phosphorus atoms may act as heterogeneous nucleation sites for the precipitation of vacancies. It is unlikely that precipitation occurs by these processes due to the high-energy AA stacking configuration as noted earlier.

A second difference between the two studies is the lack of voids in the present investigation. The effects of gaseous impurities on cavity formation are well known. For example, Maziasz [111,112] investigated the precipitation of small voids in Ti-modified austenitic stainless steels subjected to neutron irradiation or injected with helium. (Helium, in the form of $^{4}_{2}He$, is a by-product of nuclear fission and fusion reactions [113]). His studies yielded the following conclusions:

- The cavities formed exclusively at TiC interfaces

- The TiC particles behave as vacancy-baised sinks due to oversized volume misfit.
- There is a "coupled co-migration" of vacancies and helium atoms to the carbides.

Since phosphorus is probably a vapor in the solutionizing-aging temperature regime, it might be expected that it would also promote void formation. By this reasoning, Rowcliffe and Nicholson [60] dismissed the influence of dissolved gases from the furnace atmosphere to create voids. An explanation for this may lie in the relative solute to vacancy ratios; for low C_s/C_v ratios, voids may form but above a critical ratio {100} loops are preferred. Alternatively, in the presence of oxygen, the combination of vacancies, phosphorus and oxygen may lead to void formation. In this regard, Westmacott [114] investigated the effects of interstitial impurities on secondary defect formation in a variety of fcc metals and alloys. He found, for example, that quenched-in vacancies precipitate on the usual {111} planes in pure Pt, whereas the introduction of carbon induces co-precipitation on {100} planes as discussed previously. Quenching from an oxygen-containing atmosphere resulted in the replacement of the carbide structure with a void structure.

Thus, the lack of voids in the present study may be attributed to the high C_s/C_v ratio, or that the vacuum quenching eliminates oxygen pick-up. It is probable that such conditions prevent void nucleation.

Another topic to be discussed in this section is the stability of the {100} defects. As noted previously, these faulted loops are stable up to at least 100h at 500°C and for 1h at 600°C. However, no loops are observed after 10h at 600°C or at 700°C. Three possibilities exist to

explain the disappearance of defects at 600°C. One explanation is that the limit of thermal stability for the loops is ~600°C and that the actual aging temperature for the 1h samples was slightly less than 600°C, while the 10h aging may have been slightly higher. (The accuracy of the furnace is approximately ± 5°C; therefore, the respective temperatures could be 595 and 605°C). A second possibility is that the quench-induced mechanical deformation in the 10h sample was greater than the 1h sample. Indeed, the dislocation density is greater in Figure 30(a) (10h) than in Figure 15 (1h). However, if this explanation is valid, it is surprising that there are no precipitates associated with the dislocations in Figure 30(a). A third possible explanation is that aging for 1h at 600°C is sufficient for the loops to nucleate and grow whereas longer aging times dissolve the defects prior to the precipitation of more stable phases. It seems unlikely that this latter hypothesis is valid since the {100} loops co-exist with the phosphide phase at 500°C (refer to Figure 22). It is not known whether the defects are precursors to the precipitates or only provide heterogeneous nucleation sites. However, it is apparent that the structures are somehow related as discussed in section F.

Furthermore, in quenched-aged Al-Si [93] the initial microstructure consists of intrinsic dislocation loops. Aging at 150°C fine precipitates were observed to appear as the loops shrank. This illustrates the transitory nature of the phases; the shrinking dislocation loops provided vacancies for the emerging precipitates. Evidently, a more complicated situation exists in the stainless steel at 600°C.

At 700°C, the {100} defects are clearly not stable as seen in Figure 30(b). Moreover, nucleation of more stable phases is difficult since there

was no evidence of any precipitation.

Collectively, these observations are in accord with the solubility limits suggested by the phase diagram in Figure 38, and with the CBMD lattice parameter measurements from the appendix and Figures 43 and 44. Within experimental error, the lattice parameter of the 700°C/1h aged specimens is the same as the as-quenched structure. This implies that the solute is retained in solid solution. The decreasing lattice parameter of the 500-600°C aged structures is consistent with the precipitation of increasing amounts of solute. These results are also in agreement with classical nucleation and growth theories. At 700°C, the supersaturation of vacancies and solute is small; consequently, the driving force for precipitation is reduced. Whereas at 500°C, the driving force for nucleation is higher resulting in copious homogeneous and heterogeneous precipitation. The effect of pre-aging at 500°C on the precipitation of stable phases will be discussed in section F.

The final subject to be addressed in this section is the "anomalous" diffraction contrast behavior of the {100} loops as shown in Figures 15 and 18. To summarize these observations, strong loop and fault contrast results respectively with $(\underset{\sim}{g}.\underset{\sim}{b}) = +2/3$ and with $\alpha = +2\pi/3$ under kinematical conditions (w>o). It is worthwhile to reiterate that diffraction contrast theories are not <u>directly</u> applicable to the {100} defects. However, the existing theories provided an adequate framework for lattice displacement determinations. For instance, since the partial dislocation loops are invisible with <111>* reciprocal lattice vectors, it was determined that $(g.b) = 1/3$ and thus $\underset{\sim}{b} \sim a/3\langle 100\rangle$. Furthermore, the contrast asymmetries observed with $\pm\langle 220\rangle^*$ is in agreement with $\pm$ 2/3 behavior

[75]. The strong/residual contrast from the {100} stacking faults with $\alpha = \pm 2\pi/3$ however, is unique for these experimental conditions. Current contrast theory predicts that the intensity of α-fringes is independent of the sign of the product $(\underset{\sim}{g}\cdot\underset{\sim}{R})\cdot\underset{\sim}{s}$. Multi-beam effects have been shown to produce contrast asymmetries at high accelerating voltages (650keV), and it was further shown how this contrast behavior may be used to determine the nature of stacking faults [115]. More recently, Föll, et al. [116] investigated the conditions for contrast asymmetries for {111} planar defects in diamond cubic and fcc materials. In particular, they observed significant contrast variations in extrinsic stacking faults imaged with $\pm$<220>* reflections in BF and especially in WBDF conditions. The change in contrast of an intrinsic stacking fault under identical diffraction conditions was less pronounced. By considering the finite thickness of an extrinsic fault, a theory was developed which explained the majority of experimental observations for extrinsic faults and overlapping planar defects. The theory did not account, however for the contrast asymmetries in the intrinsic stacking faults. The authors suggested that impurity segregation to the faults may further complicate the image contrast of the defects.

The {100} stacking faults in this investigation present an even more complicated situation due to the non-close packed habit planes, the small size, and the inherent assumption that the defects consist of both vacancies and solute atoms. Nevertheless, it is clear that it may be possible to use this effect to infer the presence of solute atoms. Obviously, computer modeling is necessary to interpret fully these results.

The results of the experimental observations of the a/3 <100> loops discussed above are consistent with the co-precipitation of vacancies and phosphorus atoms. It was suggested that vacancies participate in a structural role in accord with the mechanism proposed for precipitation in Pt-C [92]. The position of the phosphorus in the fcc matrix is quite controversial. However, it is likely that these atoms are essentially interstitial, but due to the high vacancy-solute binding energy, they eventually occupy vacant lattice sites and become substitutional. A further conclusion drawn from this study is that the a/3<100> loops may be synonymously considered as secondary defects or semi-coherent pre-precipitates.

The other modes of precipitation will be discussed in the following sections.

B. Fine Matrix Precipitates

The small size (5-10nm), lack of diffraction spots and seemingly ubiquitous visibility makes the study of the fine matrix precipitates difficult. The only diffraction evidence from these particles was obtained from a slower quenched and subsequently aged sample (Figure 21). The diffraction patterns identify the particles as $M_{23}C_6$-type. Since the {100} faulted loops were not observed after the slower quench, it is assumed that phosphorus is associated with the carbides. This is in agreement with the results of earlier studies [55]. It is still uncertain however if phosphorus enters the carbide on the metal or the carbon lattice. In the rapid quench-age specimens, the carbides probably have the same structure but with less phosphorus than in the slower-quenched samples. The apparent {100} habit planes for the carbides (Figure 20)

is quite interesting. No previous study has reported habit planes for the initial carbides although the long-age carbides are reported to have {111} habit planes [42]. Thus, the {100} particles could be precursors to the {111} equilibrium carbides.

There is evidence that vacancies also participate in the precipitation of the carbides. In the estimation of the vacancy concentrations in the previous section, the effects of vacancy-carbon binding were neglected. However, Beeler [24] proposed a binding energy of 0.3eV for V-C complexes in a nickel lattice. While the total vacancy concentration would not be significantly increased by this association, it does imply that vacancies partition between carbon and phosphorus atoms. Evidence for this is seen in the dual-width PFZ's in Figure 27. This observation suggests that vacancies participate in the carbide precipitation, but to a lesser degree than in the planar loops. It was previously proposed that the carbides nucleate at vacancy-phosphorus-chromium-carbon complexes [55]. Therefore, $M_{23}C_6$ could precipitate by a similar mechanism to that discussed for Fe-Si-C where the lattice strain produced by the complexes is sufficient to attract migrating carbon atoms.

The necessity of vacancies for precipitate nucleation and growth is further suggested by the discontinuous precipitation at dislocations as discussed in the next section.

C. Dislocation-Nucleated Precipitation

The third mode of precipitation is on climbing dislocations. As the dislocations climb, solute renucleates to form two dimensional precipitate arrays. These precipitate-decorated dislocations clearly demonstrate that vacancies are required for precipitation. Since the quenched-in vacancies are used up in the precipitation of the matrix phases, further

precipitation can occur only through the generation of additional vacancies. Climbing dislocations and grain boundaries are sources of vacancies. For dislocation climb to occur, it is necessary that the Burgers vector has an edge component perpendicular to the plane of climb. There are thus two {111} planes and five {110} planes of easy climb for an a/2 <110> dislocation [117]. The choice of climb plane is also a function of the chemical force driving the dislocation to climb [80]. Therefore, by considering the geometry of climbing dislocations and the chemical driving force, the most efficient climb plane for producing vacancies is the one perpendicular to the Burgers vector. Indeed, this is the plane most often observed for MC precipitation in austenitic steels since vacancies are needed to relieve the stresses generated by the ~70% volume misfit [7]. The volume mismatch for $M_{23}C_6$ is only ~11% so that a variety of climb planes may be effectively used. Kegg and Silcock [44] reported that {111} climb planes are observed in addition to the {110} planes perpendicular to $\vec{b}$ for $M_{23}C_6$ precipitation on dislocations. They also state that it is apparently difficult for screw dislocations to climb into helices in these stainless steels.

From the study of dislocation-nucleated precipitation in the present investigation (Figures 23-26) it was shown that there are a multitude of dislocation-precipitate configurations. Although climb usually occurred on {110} planes, especially on the most efficient one, other planes were also observed. In contrast to Kegg and Silcock's [44] conclusions, several cases of precipitation on helical dislocations were also observed, for instance, in the WBDF stereo pair shown in Figure 26.

The identification of the heterogeneously nucleated precipitates

was not explicity determined since no diffraction evidence was obtained. However, several conjectures may be made: from diffraction contrast experiments, it is established that the precipitates are not the a/3 <100> defects (for example see Figure 25). This is to be expected since the {100} loops require such a high concentration of vacancies. For the same reasoning, it is unlikely that the particles have vacancy-type strain fields. The similarity of these dislocation-precipitate arrays with those in high carbon, high phosphorus steels [55] suggests that they are phosphorus-rich $M_{23}C_6$ type, which would explain the multiplicity of climb planes. On the other hand, the observation of matrix phosphide precipitates in the 500°C/100h samples (Figure 22) indicates that the dislocation-nucleated precipitates could be phosphides. Although an unambiguous determination is not possible from the present results, it is likely that both phosphides and carbides precipitate on the dislocations.

Before addressing the precipitate-free zones and phosphide precipitation, the defect formation in the direct quenched-aged samples will be discussed.

D. Direct Quench to 500°C

Figures 35-37 are examples of the microstructure of the direct quenched-500°C/10h aged samples. There are two main types of defects observed, the {100} loops as discussed in section A and {110} loops. This is in contrast to Rowcliffe's results [60,61], since at 500°C they only observed {100} loops, whereas aging at 600°C produced the {110} climb loops. Evidently, the vacuum quench employed in this study allowed a sufficient amount of time at temperatures slightly greater than 500°C for the {110} climb loops to nucleate while the {100} faults formed at 500°C. Clearly, vacancies are necessary for the precipitation of both

types of defects. The a/2<110> loops are probably Bardeen-Herring climb source loops as previously proposed [52,60,61]. The internal structure of these loops remains unknown, although they could be solute clusters, and appear to be on {100} planes.

E. Grain Boundary Denuded Zones

Both the quenched-aged and direct quenched-aged thermal treatments produced grain boundary denuded zones as seen in Figures 27-29, 33 and 35. The average width of PFZ's increases with increasing aging temperature; compare Figures 27 and 28. This observation is analogous to other age-hardening systems such as the well-studied Al-Zn-Mg alloys [118]. It has been previously suggested [60, 119, 120] that PFZ's are formed due to the need for a critical vacancy-solute ratio for precipitation nucleation. This hypothesis is in accord with the co-precipitation model proposed for the precipitation of the defects in this study. Similarly, the dual-width zones are consistent with a higher vacancy requirement for precipitation of the {100} defects than for the carbides.

It is interesting that not all high angle boundaries are denuded, contrary to the results of many earlier investigations [60, 118, 120]. It has been generally concluded that grain boundaries with greater than $\sim$5° misorientation are ideal sinks/sources for vacancies. Since not all of the grain boundaries in this investigation were fully analyzed, a correlation between PFZ width and boundary type is not possible at present. However, the lack of PFZ's near certain grain boundaries, for example in Figure 14 and boundaries 2-3 in Figures 29 and 35, implies that sink efficiency may be reduced at these boundaries. Recently, Balluffi [121] reviewed the effects of high angle ($\geq$15° misorientation) grain boundaries as sources/

sinks for point defects. He concluded that the sink strength depends upon both the structure of the boundary and the chemical potential of the point defects. In general, the sink efficiency decreases as boundaries become more special (i.e., more ordered); specifically Σ=3 coherent twin boundaries have been observed to be poor vacancy sinks in Al [122] and in Au [123].

The present observations are therefore similar to these latter results: disordered boundaries are potent sinks, while the sink efficiency is reduced near coincident boundaries. A possible explanation for these phenomena is as follows [121, 124].

The atomic mobility along coincident boundaries is significantly lower than along disordered ones. Indeed, in certain configurations (such as coherent twin boundaries), boundary diffusivity may approach matrix diffusivity. Therefore, when vacancy-solute complexes migrate to the ordered boundaries they become supersaturated; thus, the driving force for diffusion to the boundaries decreases. This is in contrast to disordered boundaries where the complexes may rapidly migrate along the core to other sinks such as free surfaces. The average grain boundary diffusivity of Fe in an Fe-18Cr-10Ni alloy (assuming a thickness of 1nm) is [125]:

$$D = 1.6 \times 10^{-4} \exp\left\{\frac{-0.73eV}{kT}\right\} cm^2 sec^{-1}.$$

In comparison, the bulk diffusion of Fe in a similar alloy is (see Table 5, [108]):

$$D = 1.74 \exp\left\{\frac{-2.91eV}{kT}\right\} cm^2 sec^{-1}.$$

Thus, at 500°C, the grain boundary diffusivity is approximately ten orders of magnitude higher than matrix diffusion. It is expected that the

types of defects. The a/2<110> loops are probably Bardeen-Herring climb source loops as previously proposed [52,60,61]. The internal structure of these loops remains unknown, although they could be solute clusters, and appear to be on {100} planes.

E. Grain Boundary Denuded Zones

Both the quenched-aged and direct quenched-aged thermal treatments produced grain boundary denuded zones as seen in Figures 27-29, 33 and 35. The average width of PFZ's increases with increasing aging temperature; compare Figures 27 and 28. This observation is analogous to other age-hardening systems such as the well-studied Al-Zn-Mg alloys [118]. It has been previously suggested [60, 119, 120] that PFZ's are formed due to the need for a critical vacancy-solute ratio for precipitation nucleation. This hypothesis is in accord with the co-precipitation model proposed for the precipitation of the defects in this study. Similarly, the dual-width zones are consistent with a higher vacancy requirement for precipitation of the {100} defects than for the carbides.

It is interesting that not all high angle boundaries are denuded, contrary to the results of many earlier investigations [60, 118, 120]. It has been generally concluded that grain boundaries with greater than $\sim 5°$ misorientation are ideal sinks/sources for vacancies. Since not all of the grain boundaries in this investigation were fully analyzed, a correlation between PFZ width and boundary type is not possible at present. However, the lack of PFZ's near certain grain boundaries, for example in Figure 14 and boundaries 2-3 in Figures 29 and 35, implies that sink efficiency may be reduced at these boundaries. Recently, Balluffi [121] reviewed the effects of high angle ($\geq 15°$ misorientation) grain boundaries as sources/

sinks for point defects. He concluded that the sink strength depends upon both the structure of the boundary and the chemical potential of the point defects. In general, the sink efficiency decreases as boundaries become more special (i.e., more ordered); specifically Σ=3 coherent twin boundaries have been observed to be poor vacancy sinks in Al [122] and in Au [123].

The present observations are therefore similar to these latter results: disordered boundaries are potent sinks, while the sink efficiency is reduced near coincident boundaries. A possible explanation for these phenomena is as follows [121, 124].

The atomic mobility along coincident boundaries is significantly lower than along disordered ones. Indeed, in certain configurations (such as coherent twin boundaries), boundary diffusivity may approach matrix diffusivity. Therefore, when vacancy-solute complexes migrate to the ordered boundaries they become supersaturated; thus, the driving force for diffusion to the boundaries decreases. This is in contrast to disordered boundaries where the complexes may rapidly migrate along the core to other sinks such as free surfaces. The average grain boundary diffusivity of Fe in an Fe-18Cr-10Ni alloy (assuming a thickness of 1nm) is [125]:

$$D = 1.6 \times 10^{-4} \exp\left\{\frac{-0.73eV}{kT}\right\} cm^2 sec^{-1}.$$

In comparison, the bulk diffusion of Fe in a similar alloy is (see Table 5, [108]):

$$D = 1.74 \exp\left\{\frac{-2.91eV}{kT}\right\} cm^2 sec^{-1}.$$

Thus, at 500°C, the grain boundary diffusivity is approximately ten orders of magnitude higher than matrix diffusion. It is expected that the

diffusivity of the other elements will follow the same trend. Therefore, disordered boundaries will continue to act as sinks as long as the chemical potential for complex diffusivity remains high. (Obviously, one must consider separately the chemical potentials of vacancies, solute and vacancy-solute complexes. However, the aim of the present discussion is to show qualitatively that the sink efficiency varies with boundary structure in generally-occurring boundaries. Balluffi [121] defines generally-occurring boundaries as those boundaries which are generally present in the specimens employed. This is to differentiate between studies of boundaries in bicrystals. A more detailed consideration would therefore not be realistic and would unnecessarily complicate this discussion). According to Balluffi [121], the effective grain boundary diffusivity increases with increasing binding energy between the defect and the boundary core. Furthermore, Martin and Perraillon [125] propose that the binding energy varies with the geometry to the boundary. The limited investigations of phosphorus diffusivity to austenitic grain boundaries suggests that the binding energy between phosphorus and boundaries is high [101, 102]. However, the observations of the {100} loops precipitating adjacent to certain boundaries demonstrates that the V-P complex binding energy is higher than the binding energy of the separate components to those boundaries. As such, it is speculated that the complexes retain their identity near these special boundaries allowing the co-precipitation mechanism to operate.

To test the validity of these concepts, it would be necessary to fabricate bicrystals of stainless steel with configurations near specific C.S.L. misorientations.

The next section in this chapter will discuss the precipitation of the phosphide phase.

F. Phosphide Precipitation

One of the main objectives of the study of the austenitic steel was to determine the sequence of events occurring prior to the precipitation of equilibrium phases. From the results of the 500°C/100h aged samples (Figure 22), it appears that the {100} phosphorus-rich loops and phosphide precipitates co-exist. In the Pt-C system, there is a gradual transition from a/3<100>vacancy loops to a/2<100> loops and continuing progressively to a<100> defects and beyond [93]. Furthermore, it was recently shown [74, 126] that the a/2<100> loops have a bct crystal structure similar to θ' in Al-Cu. Therefore, in this context, the a/3<100> loops in Pt-C are analogous to G.P. zones. In the present study, however, there is no evidence of other transitional phases prior to the phosphide precipitation. As noted earlier, it is not known whether the a/3<100> planar loops are true pre-precipitates or if they only act as heterogeneous nucleation sites for the precipitates. In either case, there is a strong evidence that the homogeneously dispersed precipitates in the double-aged samples (Figure 31) are due to the precipitation of vacancy-type defects at 500°C. Rowcliffe and Nicholson [60] also observed this effect and further found that the density of phosphide precipitates increases with lower pre-aging temperatures. These observations are in line with other "innoculation" studies, such as in reference 88.

The equilibrium precipitate in low-carbon, phosphorus-containing austenitic steels is chromium-rich M_3P. Rowcliffe, et al. [60, 61], as well as Azarian, et al. [64], proposed that the stable precipitate in their

alloys is Cr_3P; although neither group provided diffraction evidence for this identification. In chromium-free austenites, the stable phase is $(Fe, Ni)_3P$ [103-106]. From the X-ray diffraction card catalogue, M_3P structures are generally body-centered tetragonal ($I\bar{4}$) with c/a ~2.0. The CBMD patterns shown in Figure 32 are clearly not consistent with a bct unit cell in real space. Rather, the model more closely resembles the reciprocal lattice of a (real space) face-centered tetragonal (F4/mmm) structure. Alternatively, it is consistent with either a face-centered or base-centered orthorhomic cell (Fmmm or Cmmm respectively) in real space. A related compound within this range of structures is Cr_3PN which has a base-centered orthorhombic cell with a screw diad (Cmcm). The lattice parameters for this precipitate are a = 0.30nm, b = 0.98nm and c = 0.72nm [127]. Obviously, additional diffraction evidence is required to determine uniquely the crystal structure of the precipitates in this investigation. This could be done most readily by chemically extracting the phase onto TEM grids. The necessity for high angle tilting would therefore be reduced since CBMD patterns are capable of providing three dimensional symmetries as discussed in the appendix. Another advantage of using extraction replicas is the relative ease of doing chemical analysis by X-ray dispersive techniques without the complications of simultaneously analyzing the matrix.

The final section in this chapter will address the implications of this study on other related materials.

5.4 Concluding Remarks

The two alloys studied in this investigation are widely diverse in terms of crystal structure, composition and types of interstitial phases

that form. These technologically important systems were chosen and the experiments designed to test the validity of recently developed concepts of phase transformations. This comparative study has advanced the understanding of the interrelationships between precipitation processes and lattice defects. The observations on both the ferritic and austenitic alloy systems clearly demonstrated that the microstructures, and by inference, the properties, are sensitively dependent on the type of minor alloy additions as well as the thermal history. Specifically, the nucleation and growth of intragranular oversize second phases requires the structural and volume accommodation provided by lattice defects. By varying the concentration of vacancies or dislocations participating in the reaction, quite different structures can arise. This evidence, when considered together with early studies on steels and more recent investigations which have elucidated the roles of defects in phase transformations in model systems confirms the generality of these concepts.

This has important implications for many practical aspects of alloy design; thus, it seems fruitful to extend these ideas to phase transformations in related alloy systems. For example, the current generation of dual-phase steels provides a wide avenue of structure property relationships. However, it is not generally appreciated that these steels undergo precipitation hardening reactions which can clearly effect working operations and in-service properties. The present investigation shows that by studying the component alloy phases separately, the mechanistics of the reactions can be identified. Furthermore, the two distinct roles of vacancies which have been characterized points to the potential for sophisticated alloy design through the use of carefully

controlled thermo-mechanical treatments.

The results from the study of the austenitic steel also demonstrates the delicate balance that exists between experimental parameters: Furnace atmosphere, quench rate, annealing and aging temperatures and aging time all affect the resultant microstructures. Another effect of minor alloying additions, that of segregation to grain boundaries or other interfaces, is also better understood: The strong vacancy/solute atom binding energies show that the partitioning of embrittling elements is inevitable under conditions of large vacancy or interstitial fluxes (e.g., in a reactor environment) unless the offending atom can be sequestered in a stable precipitate structure.

Appendix: Convergent Beam Microdiffraction Techniques

The purpose of this appendix is to present a brief review of the salient features and uses of convergent beam microdiffraction (CBMD) techniques in a TEM. Comprehensive reviews of this subject exist in the literature; especially noteworthy are the articles by Warren [128], Steeds [129] and Carpenter [130]. The present discussion is therefore limited to a summary of the applications and to the specific procedures employed in this investigation.

CBMD is simply defined as the use of small electron probes (~0.5 to 50nm in diameter) to form a diffraction pattern from a region of interest. These patterns are obtained by using the two condenser lenses and the upper objective lens as a triple condenser system to focus the incident beam on the sample. As with conventional selected area diffraction (SAD) techniques, the CBMD patterns are formed at the back focal plane of the lower objective lens. (Refer to the ray diagrams in references [128] and [129]). However, since the specimen is irradiated over a range of angles, the Bragg "disk" diameters are larger than in the case of SAD. The terms beam divergence and angular resolution, denoted by αi, refer to one-half the diameter of a Bragg disk in a diffraction pattern, expressed in radians [130]. From Bragg's law, the spacing of diffraction spots is $2\theta_B$; therefore, if $\alpha i > \theta_B$, the disks overlap. The incident probe size and divergence angle are controlled by the size of the second condenser aperature and the excitation of the probe-forming lenses; the probe diameter and divergence angle are inversely related.

In modern TEM's (such as the Philips EM 400), a wide range of convergence angles and resultant Bragg disk sizes are possible. Two

other advantages inherent in the design of the EM400 are: (1) an improved vacuum system to reduce specimen contamination, and (2) a wide range of diffraction pattern magnifications (i.e., camera lengths) which enables the viewing of large areas of reciprocal space (low camera length) or the fine details within a single Bragg reflection (high camera length). The choices of microscope parameters depends upon the desired results. The CBMD applications used in this investigation along with the experimental methods are described below.

1. Second-Phase Diffraction

As discussed in chapter 4.0, several attempts were made to extract diffraction information from the a/3 <100> planar defects in the stainless steel. Although the results were negative (Figure 17), CBMD patterns were obtained from the {100} phosphide phase (Figure 32). Since the crystal structure of these precipitates was not known a priori, the CBMD patterns were taken at high spatial (small probe diameter) and high angular (small second condenser aperture) resolution resulting in a beam divergence of ~0.7mrad. Consequently, it was possible to resolve the closely spaced Bragg reflections of the precipitates (Figure 32). In principle, the procedure for obtaining CBMD information is straight forward, although in practice the technique requires much experimental manipulation for small particles. For example, the following procedures were used in the study of the a/3<100> defects in this investigation and the a/2<100> defects in Pt-C [74, 131]. It is first necessary to align the microscope, obtain the eucentric position and tilt to the exact zone axis. Since the small precipitates have <100>-type displacement vectors, a small tilt away from the exact orientation is often

required to see the defects in certain zone orientations. While the initial tilting may be accomplished at lower magnifications (20,000-40,000x), it is helpful to work at ∿100 000x for the final adjustments. At 100,000x the ∿30nm particles are ∿0.3cm on the screen which necessitates high spatial resolution. Thus, after focussing the sample with the objective lens control, the second condenser lens was fully excited and the electron probe was centered on the precipita . The diffraction conditions may then be checked and any final adjustments made. When the diffraction conditions are optimized, a small condenser aperature may be selected; since it is difficult to recenter the aperatures precisely with a fully excited condenser lens, this alignment step may be skipped as long as the fully focussed beam is centered on the precipitate. If the preceding steps are carried out with an objective aperature in, it is wise to remove it and reposition the beam if necessary. (This precautionary measure is required if the objective aperature is dirty). Finally, the diffraction pattern may be recorded; typical exposure times were from 30 seconds to 3 minutes. It should be noted that the precipitate reflections were not seen on the screen, so several exposures of each condition were necessary. After every exposure, the position of the beam with respect to the precipitate was rechecked. Specimen and/or beam drift was often a problem with long exposure times. To eliminate the possibility of confusion from higher order matrix Laue reflections, several exposures were also taken from adjoining precipitate-free areas. The optimum camera length for these experiments was 450mm.

If smaller probe diameters are required, three alternatives may be

used: (1) Tungsten filaments may be undersaturated slightly to form smaller coherent tips. Although the overall intensity on the screen decreases, there is sufficient intensity in the focused probe for diffraction. (2) The specimen height may be slightly lowered from eucentric position to form a finer probe. (3) Higher convergence is also possible by using scanning transmission electron microscopy (STEM) configurations. However, it is difficult to image the fine precipitates in the STEM mode, and therefore more difficult to position the probe accurately.

The above exacting procedures are necessary to form single crystal CBMD patterns from small precipitates. However, less rigorous techniques may be used for larger and/or more strongly diffracting phases. For instance, after the initial experiments, larger probe sizes were used for the CBMD patterns in Figure 32. In general, the largest beam diameter comensurate with the size of the phase should be used to reduce exposure times and to reduce specimen contamination.

2. Matrix Orientation

CBMD also facilitates the determination of matrix orientations by providing Kikuchi lines in relatively thin areas. Three applications in which this was especially helpful in the present investigation were for high angle specimen tilts, to select the precise diffraction conditions for WBDF imaging, and for axis/angle pair studies as discussed in section 4.2.1.E. The origin and advantages of Kikuchi lines for these applications are well-known [67-70]. However, not all materials provide crisp electron channeling patterns; nor is inelastic scattering

always available in thin or highly deformed regions by conventional SAD. These limitations may be overcome with CBMD; in this situation, Kikuchi patterns arise from the Bragg diffraction of the cone of electrons irradiating the sample. Coupled with low camera lengths (e.g., 280mm), the resulting patterns are amazingly simple to index; for example, refer to the patterns in Figure 29.

Compared to the procedures in the previous section, the experimental constraints are relaxed for these applications of CBMD. For large-grain materials, high spatial resolution is often not critical, so that larger probe sizes may be used. Indeed, it was found that the larger beam diameters provided the sharpest Kikuchi patterns. However, relatively higher angular resolution must be maintained; otherwise, intensity from the Bragg disks will overshadow the Kikuchi lines. Hence, the optimal condenser aperature must be experimentally determined for the specific situation.

3. Thickness Measurements

Another widely used application of CBMD patterns is the determination of foil thickness; while several methods have been proposed for this purpose (e.g., references 132-134) Kelley's, et al. [132] technique is the most readily applicable for use with the EM400 without the necessity of extensive calculations. This analytical method makes use of the spacing of intensity oscillations within the Bragg disks formed by a focused probe of electrons. From dynamical two-beam theory, the intensity oscillations are related to the foil thickness, t, by the following

equation

$$(A1) \qquad (s_i^2 + {}^1/\xi_g^2)\, t^2 = n_i^2$$

where s_i is the deviation from the i-th minimum from the exact Bragg position, ξ_g is the extinction distance and n_i is an integer.

Allen [132] found that errors of less than 2% in thickness determinations are possible with higher order diffraction vectors using this method. For fcc materials, it is advisable to use <200>*, <220>* or <311>* vectors to avoid multiple beam effects. For maximum accuracy, the reflection is set close to the exact Bragg position in an orientation to minimize extraneous Kikuchi lines. The probe size depends upon the condition of the specimen, e.g., the grain size, and densities of dislocations and precipitates. In general, a large second condenser aperature (such that $\alpha_i \lesssim \Theta_B$) and a relatively high camera length (600-900mm) facilitate the analysis.

The analysis procedure will be demonstrated by referring to Figure 40(a) which is a $[2\bar{2}0]^*$ two-beam pattern from a stainless steel sample. The s_i values are determined by measuring the distance D_i from the center of the diffracted beam to the successive minima as well as the $2\Theta_B$ distance, as shown. These measurements are easily obtained from a magnified print using a ruler. The s_i values are then obtained from the relationship:

$$(A2) \qquad s_i = \frac{\lambda}{d^2}\left(\frac{\Delta Oi}{2\Theta_B}\right)$$

where λ is the electron wavelength and d is the interplanar spacing.

Equation (A1) may be rewritten in the general format of a straight line,

$$(A3) \qquad \left(\frac{si}{n_i}\right)^2 = -\left(\frac{1}{\xi g}\right)^2 \left(\frac{1}{n_i}\right)^2 + \left(\frac{1}{t}\right)^2$$

and $(s_i/n_i)^2$ plotted versus $(^1/n_i)^2$.
Thus, the slope of the line is $-(^1/\xi_g)^2$ and the y-intercept is $(1/t)^2$. The values of n_i are found by trial and error, and only the correct set of n_i yield a straight line. Figure 41(b) illustrates the plot obtained from the experimental pattern. The y-intercept corresponds to a thickness of 132nm, and the slope gives a <220>* extinction distance of 40nm. This experimentally derived ξ_{220} value agrees well with the uncorrected value from pure nickel [67, 75] which was assumed valid for the stainless steel.

Similar analyses have been made in dual-phase steels (in the ferrite) by Hoel and Thomas [32] and in the course of the present research program.

4. Lattice Parameter Determinations

A further use of CBMD employed in this investigation was to assess the matrix lattice parameter variations in the aged stainless steel. Steeds and his coworkers [129, 136] elegantly demonstrated that the shifts of the higher order Laue zone (HOLZ) lines in <111> CBMD patterns are proportional to the change in the lattice parameter. According to kinematical theory, the line shift with lattice parameter change may be derived from the formula:

(A4) $$\frac{\Delta a}{a} = -\frac{\Delta\Theta}{\Theta}$$

An example of a [111] CBMD pattern from a stainless steel specimen is shown in Figure 41 and illustrates the fine HOLZ lines in the central disk and the corresponding HOLZ ring of radius R. Note that the HOLZ lines reveal three-fold symmetry; the prominent "triangle" in the central disk is formed by the intersection of three $<\bar{5}\bar{5}11>^*$ lines. The relative size of this triangle may be used to monitor the change in lattice parameters; the accuracy of these dererminations is greater when the

measurements are made with respect to a known standard [129]. Figure 42 is a schematic drawing of a HOLZ triangle and the 000 and $\bar{2}00$ Bragg disk in a [111] pattern. If the height of the triangle is X and the <200>* distance is Y, then equation (A4) may be rewritten as:

(A5) $$\frac{\Delta a}{a} = -\frac{2}{3}\left(\frac{\Delta X}{\Delta Y}\right) / R$$

where $\Delta X = X_{ref} - X$

$\Delta Y = Y_{ref} - Y$

R = HOLZ radius

The factor of two is introduced since R is equivalent to $2\theta_B$, while the factor of 1/3 is included because the change in line position is equal to one-third of the change in height of the triangle [129].

The central disks from [111] zone axis patterns from the quenched-aged steels are presented in Figure 43. Several measurements from each of these samples were averaged to deduce the change in lattice parameter with respect to the as-quenched samples. The resulting values are plotted on the graph in Figure 44, where the error bar reflects the range of values which were averaged for the determinations.

As discussed in chapter 5.3, the relative decrease in the matrix lattice parameter correlates well with the degree of precipitation observed in the BF and WBDF images. However, due to the paucity of thermodynamic data in the stainless steel-phosphorus system, a direct comparison between the matrix lattice parameter and phosphorus content is not presently possible. Sarikaya [137] has recently used this procedure to determine the carbon content of retained austenite in a duplex martensite-austenite steel.

The microscope parameters used to obtain the zone axis patterns are

similar to those suggested for thickness measurements. Several additional experimental factors should also be pointed out: First, not all TEM specimens are suitable for CBMD with HOLZ lines; highly strained samples are especially unsuitable. Steeds [129] discussed the conditions for visibility of HOLZ lines and suggested that lower temperatures and lower accelerating voltages often enhance visibility. Second, for fcc materials at 100keV and ambient temperatures, HOLZ lines are most likely to be visible at the <111> and <114> poles. Third, the final tilting to an exact zone axis may be done by shifting the condenser aperature; however, extreme aperature movements may produce pattern a symetries. Fourth, low camera lengths (280mm) are used to view the HOLZ ring such as in Figure 41, whereas higher camera lengths (600-900mm) are beneficial for lattice parameter determinations, as shown in Figure 43.

An alternative procedure for measuring small changes in lattice parameters by the positions of HOLZ lines was recently published by Ralph and his coworkers [138]. Their method is to treat the HOLZ lines as higher-order Kikuchi lines and to generate CBMD patterns via computer simulations. A series of these patterns with different lattice parameters are compared with experimental patterns and the closest match chosen. This method is perhaps less susceptible to human errors, and is therefore more accurate for relative lattice parameter measurements.

Acknowledgements

This section of the thesis attests to the fact that whereas vacuum atmospheres are beneficial for metallurgical applications, researchers can not work effectively in vacu. Therefore, it is with great satisfaction that I make the following acknowledgements: I would like to thank Prof. G. Thomas, Dr. K.H. Westmacott, Prof. J. Clarke and Dr. U. Dahmen for their critical and illuminating reviews of my thesis. This program could not have been completed without the continual collaboration with Ken and Uli; their sagacity, humor and friendship created a pleasurable environment for research. I also acknowledge Ron Gronsky whose ubiquitous enthusiasm was contagious, and Mike Witcomb for his timely wit and expertise in the art of sample preparation. I additionally thank David Ackland, Kathleen Brusse, Madeline Moore and Mark Wall for their friendship and help in many ways during the course of this work; an extra note of appreciation is extended to Kathleen for expertly typing this manuscript. Gareth is further acknowledged for his oenological seminars.

Much of my time at Berkeley was spent in the basement of Hearst Mining Building; I especially want to acknowledge my friends who shared that time with me, including: Llewellyn Rabenberg, R'Sue Caron, Eduardo Kamenetzky, Jean-Marc Lang, José Briceño Valero, Jamie Rose, Jurek Mazur, I-Nan Lin, Jim Gebhardt, Tom Shaw, Channing Ahn and Mehmet Sarikaya.

To my family for their constant encouragement and to my wife, Sandy, for her understanding, love and endurance during this adventure.

I also acknowledge Bob Sinclair at Stanford University for his patience and support during the final throes of thiswork. Similarly, I thank Lee Tanner for his lively discussions.

I wish to thank Dr. A. F. Rowcliffe for providing the stainless steel samples and Prof. Thomas' steel group for the dual-phase alloys.

This work was supported by the Director, Office of Energy Research, Office of Basic Energy Sciences, Materials Science Division of the U.S. Department of Energy under Contract No. DE-AC03-76SF00098.

REFERENCES

1. W. G. Johnston, T. Lauritzen, J. H. Rosolowski and A. M. Turkalo, "The Effect of Metallurgical Variables on Void Sewlling," in Radiation Damage in Metals, eds., N. L. Peterson and S. D. Harkness, ASM, Metals Park, OH, p. 227 (1976).
2. J. Burke, J. Less-Common Metals, 28, 441 (1972).
3. D. N. Seidman, "Field-Ion Microscope Studies of the Defect Structure of the Primary State of Damage of Irradiated Metals, p. 28 in ref. 1.
4. Vacancies and Interstitials in Metals, eds., A. Seeger, D. Schumacher, W. Schilling and J. Diehl, North Holland, Amsterdam (1970).
5. J. K. Tien, S. T. Tao, J. P. Wallace and S. Purushothaman, "Positron Probing of Microstructures and Substructures in Metals and Alloys," in Electron and Positron Spectroscopies in Materials Science and Engineering, eds., O. Buck, J. K. Tien, H. L. Marcus, Academic Press, New York, p. 73 (1979).
6. A. S. Nowick, Progress in Metal Physics, Volume 4, ed. B. Chalmers, Permagon Press, New York, p. 1 (1953).
7. D. V. Edmonds and R. W. K. Honeycombe, "Precipitation in Iron Base Alloys," in Precipitation Processes in Solids, eds., K. C. Russell and H. I. Aaronson, TMS-AIME, New York, p. 121 (1978).
8. Precipitation From Iron-Base Alloys, eds., G. R. Speich and J. B. Clark, AIME, New York (1965).
9. W. Pitsch and A. Schrader, Arch. Eisenhuetten W. , 29, 715 (1958).
10. K. F. Hale and D. McLean, J.I.S.I., 201, 337 (1963).
11. W. C. Leslie, R. M. Fisher and N. Sen, Acta Met. 7, 632 (1959).

12. R. H. Doremus and E. F. Koch, Trans. AIME, 218, 591 (1960).

13. W. C. Leslie, Acta Met. 9, 1004 (1961).

14. H. Wagenblast and R. C. Glenn, Met. Trans. 1, 2299 (1970).

15. E. W. Langer, Met. Sci. J. 2, 59 (1968).

16. D. Hull and I.L. Mogford, Phil. Mag. 6, 535 (1961).

17. H. Wagenblast and A. C. Damask, J. Phys. Chem. Solids, 23, 221 (1962).

18. F. E. Fujita and A. C. Damask, Acta Met. 12, 331 (1964).

19. R. A. Arndt and A. C. Damask, Acta Met 12, 341 (1964).

20. H. Wagenblast, F. E. Fujita and A. C. Damask, Acta Met. 12, 347 (1964).

21. T. Takeyama and H. Takahasi, J. Japan Inst. Metals, 38, 138 (1974).

22. M. Weller and J. Diehl, Solid State Commun. 17, 1223 (1975).

23. P. Hautojärvi, J. Johansson, A. Vehanen, J. Yli-Kauppila and P. Moser, Phys. Rev. Letters 44, 1326 (1980).

24. J. R. Beeler, "Impurity Atom Effects in Metallic Crystals," in Interatomic Potentials and Simulations of Lattice Defects, Plenum Press, New York, p. 339 (1972).

25. R. F. Vyhnal and S. V. Radcliffe, Acta Met. 20, 435 (1972).

26. M. J. Young, M.S. Thesis, University of California, Berkeley, CA, 1977 (LBL report number 6620).

27. T. J. O'Neill, M.S. Thesis, University of California, Berkeley, CA, 1979 (LBL report number 9047).

28. X. F. Wu and G. Thomas, in press.

29. G. Thomas and J. Y. Koo, "Developments of Strong, Ductile Duplex Ferritic-Martensitic Steels," in Structure and Properties of Dual-Phase Steels, eds., R. A. Kot and J. W. Morris, AIME, Warrendale, PA, p. 183 (1979).

30. J. Y. Koo, M. J. Young and G. Thomas, Met. Trans. 11A, 852 (1980).

31. P. K. Costello, M.S. Thesis, University of California, Berkeley, CA, 1978 (LBL report number 8628).

32. R. H. Hoel and G. Thomas, Scripta Met. 15, 867 (1981).

33. J. S. Gau, M.S. Thesis, University of California, Berkeley, CA, 1981, (report number 12058).

34. A. Nakagawa, M.S. Thesis, University of California, Berkeley, CA, 1981 (LBL report number 12843).

35. J. S. Gau, J. Y. Koo, A. Nakagawa and G. Thomas, "Microstructure and Properties of Dual Phase Steels Containing Fine Precipitates," in Fundamentals of Dual-Phase Steels, eds., R. A. Kot and B. L. Bramfill, AIME, New York, (1981).

36. J. Y. Koo, Ph.D. Thesis, University of California, Berkeley, CA, 1977 (LBL report number 6657).

37. R. H. Hoel, private communication.

38. W. B. Pearson, Handbook of Lattice Spacings and Structures of Metals, Volume 2, Permagon Press, Oxford (1967).

39. H. J. Goldschmidt, Interstitial Alloys, Butterworths, London (1969).

40. E. H. Lee, P. J. Maziasz and A. F. Rowcliffe, "The Structure and Composition of Phases Occurring in Austenitic Stainless Steels in Thermal and Irradiation Environments," in Phase Stability During Irradiation, eds., J. R. Holland, D. I. Potter, L. K. Mansur, AIME, New York, p.191 (1981).

41. M. K. Lewis and B. Hattersley, Acta Met. 13, 1159 (1965).

42. F. R. Beckitt and B. R. Clark, Acta Met. 15, 113 (1967).

43. G. R. Kegg and J. M. Silcock, Met. Sci. J. 6, 47 (1972).

44. G. R. Kegg and J. M. Silcock, Scripta Met. 8, 1245 (1974).

45. L. K. Singhal and J. W. Martin, J.I.S.I. 205, 947 (1967).

46. P. H. Pumphrey and J. W. Edington, Acta Met. 22, 89 (1974).

47. J. M. Silcock, J.I.S.I. 201, 409 (1963).

48. L. K. Singhal and J. W. Martin, Acta Met. 16, 1169 (1968).

49. B. Weiss and R. Stickler, Met. Trans. 3, 851 (1972).

50. L. Boulanger, J. Nucl. Mater. 64, 179 (1977).

51. H. R. Brager and F. A. Garner, J. Nucl. Mater. 73, 9 (1978).

52. G. Henry, H. J. Harding, J. Philibert and J. Plateau, Mem. Sci. Rev. Met. 64, 11 (1967).

53. B. R. Banerjee, E. J. Dulis and J. J. Hauser, Trans. ASM 61, 103 (1968).

54. F. H. Froes, M. G. M. Wells and B. R. Banerjee, Met. Sci. J. 2, 232 (1968).

55. G. R. Kegg, J. M. Silcock and D. R. F. West, Met. Sci. J. 8, 337 (1974).

56. A. G. Allten, J. G. Y. Chow and A. Simon, Trans. ASM 46, 950 (1954).

57. G. R. Rundell and R. J. Raudebaugh, Trans ASM 53, 233 (1961).

58. K. J. Irvine, D. T. Llewellyn and F. B. Pickering, JISI 199, 153 (1961).

59. K. C. Thomas and E. B. Weglein, Trans. ASM, 56, 566 (1963).

60. A. F. Rowcliffe and R. B. Nicholson, Acta Met. 20, 143 (1972).

61. A. F. Rowcliffe and B. L. Eyre, J. Phys. F: Metal Phys. 1, 771 (1971).

62. J. P. Shepherd, Met. Sci. 10, 174 (1976).

63. M. Kikuchi, T. Nishimura, T. Tanaka and R. Tanaka, TMS-Met. Trans.

9A, 1337 (1978).

64. A. Azarian, M. Da Cunha Belo and J. LeTeurtre, Scripta Met. 9, 185 (1975).

65. A. Azarian and K. Kheloufi, J. Nucl. Mater. 97, 25 (1981).

66. L. Boulanger, Scripta Met. 14, 67 (1980).

67. P. B. Hirsch, A. Howie, R. B. Nicholson, D. W. Pashley and M. J. Whelan, Electron Microscopy of Thin Crystals, R. E. Kriger Huntington, NY (1977).

68. G. Thomas and M. J. Goringe, Transmission Electron Microscopy of Materials, J. Wiley and Sons, New York (1979).

69. J. W. Edington, Practical Electron Microscopy in Materials Science, Monograph 2, Philips, Einhoven (1975).

70. M. H. Loretto and R. E. Smallman, Defect Analysis in Electron Microscopy, Chapman and Hall, London (1975).

71. M. F. Ashby and L. M. Brown, Phil. Mag. 8, 1083 (1963).

72. M. F. Ashby and L. M. Brown, Phil. Mag. 8, 1649 (1963).

73. U. Dahmen, K.H. Westmacott and G. Thomas, Acta Met. 29, 627 (1981).

74. M. J. Witcomb, U. Dahmen and K.H. Westmacott, proceedings of EMSSA Meeting 11, 45 (1981).

75. J. M. Oblak, B. H. Kear in Electron Microscopy and Structure of Materials, eds. G. Thomas, R. M. Fulrath and R. M. Fisher, University of California Press, Berkeley, CA, p. 566 (1972).

76. D. J. H. Cockayne, M. L. Jenkins, I. L. F. Ray, Phil. Mag. 24, 1383 (1971).

77. G. Thomas and W. Bell in Lattice Defects and Their Interactions, ed. Hasiguti, Gordon and Breach Sci. Publ. Inc., N.Y., p. 477 (1967).

78. U. Dahmen, Ph.D. Thesis, University of California, Berkeley, CA, 1979 (LBL report number 8661).

79. H. Föll and M. Wilkens, Phys. Stat. Sol. (a) 31, 519 (1975).

80. J. P. Hirth and J. Lothe, Theory of Dislocations, McGraw-Hill, New York (1968).

81. T. Malis, *in reference 82 page 42.*

82. Grain Boundary Structure and Kinetics, eds. R. W. Balluffi, ASM, Metals Park, OH (1980).

83. R. Gronsky, Ph.D. Thesis, University of California, Berkeley, CA, 1976 (LBL report number 5784).

84. J. M. Briceno-Valero, Ph.D. Thesis, University of California, Berkeley, CA 1981 (LBL report number 13626).

85. E. Kamenetzky, M.S. Thesis, University of California, Berkeley, CA, in press.

86. H. Mykura, in reference 82, page 445.

87. Precipitation Processes in Solids, eds. K. C. Russell and H. I. Aaronson, TMS-AIME, New York, (1978).

88. H. S. Rosenbaum and D. Turnbull, Acta Met. 6, 653 (1958).

89. T. Federighi and G. *Thomas, Phil. Mag. 7, 127 (1962).*

90. A. G. Khachaturyan, Sov. Phys.-Solid State 13, 2024 (1972).

91. K. C. Russell, Scripta Met. 3, 313 (1969).

92. K. H. Westmacott and M. I. Perez, J. Nucl. Mat. 83, 231 (1979).

93. U. Dahmen, A. R. Pelton, M. J. Witcomb and K. H. Westmacott, Proceedings of the International Conference on Solid-Solid Phase Transformations, eds. H. I. Aaronson and M. Waymen, in press.

94. J. A. Wert, Acta Met. 28, 1361 (1980).

95. L. DeSchepper, G. Knuyt and L. M. Stals, Phys. Stat. Sol. (a) 67, 153 (1981).

96. J. Y. Koo, M. Raghavan and G. Thomas, Met. Trans. 11A, 351 (1980).

97. H. I. Aaronson, J. K. Lee and K. C. Russell in reference 87, page 31.

98. R. A. Johnson, Acta Met. 15, 513 (1967).

99. D. H. Jack and K. H. Jack, Mat. Sci. and Eng. 11, 1 (1973).

100. C. Wert, Phys. Rev. 79, 601 (1950).

101. M. Guttmann and D. McLean, "Grain Boundary Segregation in Multicomponent Systems," in Interfacial Segregation, eds., W. C. Johnson and J. M. Blakely, ASM, Metals Park, OH, p. 261 (1979).

102. A. W. Funkenbusch, L. A. Heldt and D. F. Stein, Met. Trans. 13A, 611 (1982).

103. A. S. Doan, Jr. and J. I. Goldstein, Met. Trans. 1, 1759 (1970).

104. T. R. Heyward and J. I. Goldstein, Met. Trans. 4, 2335 (1973).

105. A. S. Norkiewicz and J. I. Goldstein, Met. Trans. 6A, 891 (1975).

106. A. D. Romig, Jr. and J. I. Goldstein, Met. Trans. 11A, 1151 (1980).

107. K. M. Chang, Ph.D. Thesis, University of California, Berkeley, CA (1979) (LBL report number 9208).

108. A. F. Smith and C. Gibbs, Met. Sci. J. 2, 47 (1968).

109. A. F. Smith and C. Gibbs, Met. Sci. J. 3, 93 (1969).

110. R. Hultgren, P. D. Desai, D. T. Hawkins, M. Gleiser and K. K. Kelley, Selected Values of the Thermodynamic Properties of the Elements, ASM, Metals Park, OH (1973).

111. P. J. Maziasz, Scripta Met. 14, 1251 (1980).

112. P. J. Maziasz, "Helium Trapping at Ti-Rich MC Particles in Ti-Modified

Austenitic Stainless Steel," in reference 40.

113. H. Semat and J. R. Albright, Introduction to Nuclear Physics, Holt Rinehart and Winston, New York (1972).

114. K. H. Westmacott, Crystal Lattice Defects 6, 203 (1976).

115. L. J. Chen and G. Thomas, Phys. Stat. Sol. (a) 25, 193 (1974).

116. H. Föll, C. B. Carter and M. Wilkens, Phys. Stat. Sol. (a) 58, 393 (1980).

117. H. M. Miekk-oja and R. Räty, Phil. Mag. 24, 1197 (1971).

118. J. D. Embury and R. B. Nicholson, Acta Met. 13, 403 (1965).

119. A. Eikum and G. Thomas, J. Phys. Soc. Japan 18, 98 (1963).

120. P. N. T. Unwin, G. W. Lorimer and R. B. Nicholson, Acta Met. 17, 1363 (1969).

121. R. W. Balluffi,"High Angle Grain Boundaries as Sources or Sinks for Point Defects," in reference 82 page 297.

122. B. K. Basu and C. Elbaum, Acta Met. 13, 1117 (1965).

123. R. W. Siegel, S. M. Chang and R. W. Balluffi, Acta Met. 28, 249 (1980).

124. R. Gronsky, private communication.

125. G. Martin and B. Perraillon, "Measurements of Grain Boundary Diffusion," in reference 82 page 239.

126. U. Dahmen, M. J. Witcomb and K. H. Westmacott, to be published.

127. ASTM X-ray card number 21-240.

128. J. B. Warren, "Microdiffraction," in Introduction to Analytical Electron Microscopy, eds., J. J. Hren, J. I. Goldstein and D. C. Joy, Plenum Press, New York, p. 369 (1979).

129. J. W. Steeds, "Convergent Beam Electron Diffraction," in reference

128, page 387.

130. R. W. Carpenter, "Microdiffraction from Crystals Containing Defects," in Proceedings of 15th Annual Conference of the Microbeam Analysis Society, ed., D. B. Wittry, San Francisco Press, Inc., San Francisco, p. 1 (1980).

131. M. J. Witcomb, private communication.

132. P. M. Kelly, A. Jostsons, R. G. Blake, and J. G. Napier, Phys. Stat. Sol. (a) 31, 771 (1975).

133. T. Tan, W. L. Bell and G. Thomas, Phil. Mag. 24, 417 (1971).

134. D. J. H. Cockayne , P Goodman, J. C. Mills and A. F. Moodie, Rev. Sci. Instrum. 38, 1097 (1967).

135. S. M. Allen, Phil. Mag. 43A, 325 (1981).

136. P. M. Jones, G. M. Rackham and J. W. Steeds, Proc. R. Soc. Lond. A 354, 197 (1977).

137. M. Sarikaya, Ph.D. Thesis, University of California, Bekekeley, CA, in press.

138. E. C. Ecob, M. P. Shaw, A. J. Porter and B. Ralph, Phil. Mag. 44A, 1117 (1981).

Table 1: Alloy Compositions in wt%

Fe - 1.96Si - 0.15C

Fe - 18.18Cr · 10.25Ni - 0.60Mn - 0.31Si - 0.009N - 0.01C - 0.31P

Table 2: Thermal Treatments

Alloy	Solution Treatment	Aging Treatment
Fe-Si-C	1150°C 1h Ice Water Quench (IWQ)	25°C < 1h
	+ 850°C 1h IWQ	25°C 1 week (W)
		25°C 1 w + 100°C 1h
		100°C 1 h + 25°C 2w
		170°C 1 h
Fe-Cr-Ni-P	1150°C 1 h Furnace Cool	
	1150°C 1h IWQ	500°C 1h
		500°C 10h
		500°C 100h
		600°C 1h
		600°C 10h
		700°C 1h
		500°C 10h + 700°C 24h
	1150°C 1h Direct Quench	500°C 10h

Table 3: Summary of Defect Contrast Behavior in Figure 15

[Values of ($\underset{\sim}{g}\cdot\underset{\sim}{b}$) and α (= $2\pi\underset{\sim}{g}\cdot\underset{\sim}{R}$)]

$\underset{\sim}{B}$		110					100		
Defect	$\underset{\sim}{g}$	$1\bar{1}1$	$1\bar{1}\bar{1}$	002	$2\bar{2}0$	$\bar{2}20$	$00\bar{2}$	$0\bar{2}0$	$02\bar{2}$
	$\underset{\sim}{b}$								
A	$\pm$1/3[010]	$\pm$1/3(I)	$\pm$1/3(I)	0(I)	+2/3(V) Inside	+2/3(I) Outside	0(I)	$\pm$2/3(V)	$\pm$2/3(V)
B	$\pm$1/3[100]	$\pm$1/3(I)	$\pm$1/3(I)	0(I)	+2/3(I) Outside	+2/3(V) Inside	0(I)	0(I)	0(I)
C	$\pm$1/3[001]	$\pm$1/3(I)	$\pm$1/3(I)	$\pm$2/3(V)	0(I)	0(I)	$\pm$2/3(V)	0(I)	$\pm$2/3(V)
	R								
A	$\pm$1/3[010]	$\pm2\pi/3$(I)	$\pm2\pi/3$(V)	0(I)	$\pm2\pi/3$(V)	$\pm$2 /3(V)	0(I)	$\pm2\pi/3$(V)	$\pm2\pi/3$(V)
B	$\pm$1/3[100]	$\pm2\pi/3$(V)	$\pm2\pi/3$(I)	0(I)	$\pm2\pi/3$(V)	$\pm$2 /3(V)	0(I)	0(I)	0(I)
C	$\pm$1/3[001]	$\pm2\pi/3$(V)	$\pm2\pi/3$(V)	$\pm2\pi/3$(V)	0(I)	0(I)	$\pm2\pi/3$(V)	0(I)	$\pm2\pi/3$(V)

V - Dislocation loop or stacking fault in strong contrast

I - Dislocation loop or stacking fault in weak contrast

Table 4: Summary of Defect Contrast Behavior in Figure 33

[Values of $(\underset{\sim}{g}\cdot\underset{\sim}{b})$]

$\underset{\sim}{B}$		110		100				
	g	$1\bar{1}1$	$1\bar{1}\bar{1}$	002	$00\bar{2}$	$0\bar{2}\bar{2}$	$0\bar{2}0$	020
Defect	$\underset{\sim}{b}$							
A	$\pm1/3[010]$	$\pm1/3$(I)	$\pm1/3$(I)	0(I)	0(I)	$\pm2/3$(V)	$\pm2/3$(V)	$\pm2/3$(V)
B	$\pm1/3[100]$	$\pm1/3$(I)	$\pm1/3$(I)	0(I)	0(I)	0(I)	0(I)	0(I)
C	$\pm1/3[001]$	$\pm1/3$(I)	$\pm1/3$(I)	$\pm2/3$(V)	$\pm2/3$(V)	$\pm2/3$(V)	0(I)	0(I)
D	$\pm1/2[101]$	±1(V)	0(I)	±1(V)	±1(V)	±1(V)	0(I)	0(I)
E	$\pm1/2[1\bar{1}0]$	±1(V)	±1(V)	0(I)	0(I)	±1(V)	±1(V)	±1(V)
F	$\pm1/2[01\bar{1}]$	$\pm$(V)	0(I)	±1(V)	±1(V)	0(I)	Inside ±1(V)	Outside ±1(V)
G	$\pm1/2[011]$	0(I)	±1(V)	±1(V)	±1(V)	±2(V)	±1(V)	±1(V)
H	$\pm1/2[10\bar{1}]$	0(I)	±1(V)	±1(V)	±1(V)	±1(V)	0(I)	0(I)

Table 5: Diffusivity of Selected Elements in Austenite

Element	Alloy Composition (wt%)	Q(eV)	Do (Cm^2/sec)	D(500°C)(cm^2/sec)	Reference
Fe	Fe-20Cr-25Ni	2.91 ± 0.04	1.74	1.70×10^{-19}	108
Cr	Fe-20Cr-25Ni	2.52 ± 0.15	0.19	6.54×10^{-18}	109
Ni	Fe-20Cr-25Ni	2.88 ± 0.11	4.06	6.22×10^{-19}	109
Ni	Fe-12Ni-0.3P	2.93 ± 0.13	1.13	8.16×10^{-20}	104
P	Fe-12Ni-0.3P	2.35 ± 0.11	0.51	2.27×10^{-16}	104

LIST OF FIGURES

8 Diffraction contrast analysis of carbides from a sample treated as in Figure 7. With $\underset{\sim}{B}$ = 001 and $\underset{\sim}{g}$ =[200]* (a), there are two variants of the larger precipitates visible but only one variant of the smaller precipitates. In (b) (BF) and (c) (DF) two variants of both precipitate sizes are visible. Note the PFZ's near the larger precipitates.

9 Fe-Si-C alloy quenched from 850°C and aged at 170°C for 1h. The {001} precipitates have nucleated heterogeneously on dislocations and small angle grain boundaries. (a) is a BF image and (b) is a weak beam dark field with the g/3g [0$\bar{1}$1]* conditions satisfied. Note that two variants of the precipitates show fringe contrast since they are inclined ∿45° to the beam.

10 Stainless steel with 0.3P sample furnace cooled (∿3°/min) from 1150°C. There does not appear to be any precipitates visible.

11 Stainless steel sample quenched from 1150°C and aged at room temperature. Only dislocations were evident after this treatment.

12 Stainless steel sample quenched from 1150°C and aged at 500°C for 1h. The beam direction is near 110 with $\underset{\sim}{g}$ = [002]*. One variant of the {100} defects is visible.

13 A BF/WBDF pair of a stainless steel sample quenched from 1150°C and aged at 500°C/10h. $\underset{\sim}{B}$ ∿ 110, and the [$\bar{1}$1$\bar{1}$]* diffraction vector was used with the g/3g condition operating for the WBDF. All three variants of the {100} loops are visible as well as precipitation on dislocations.

14 A BF/WBDF pair from a stainless steel specimen quenched and subsequently aged at 500°C for 100h. The beam direction is near 110 with the [$\bar{1}$1$\bar{1}$]* diffraction condition used to illuminate the

{100} defects and heterogeneous precipitation on climb dislocations. Note the lack of a precipitate free zone near the grain boundary.

15 A diffraction contrast analysis of defects in a sample aged at 600°C for 1h. (a), (b) BF/WBDF pair with $\underset{\sim}{B} \sim 110$ and $g = [\bar{1}11]^*$ and the g/3g condition for the WBDF. The outline area in (a) is shown in subsequent micrographs imaged in various two-beam conditions. (b)-(f) and (j) are near $\underset{\sim}{B} \sim 110$ and (g)-(i) are near $\underset{\sim}{B} \sim 100$. See text for further details.

16 A schematic Kikuchi map of the diffraction conditions used to image the micrographs in Figure 15.

17 A 100 convergent beam microdiffraction pattern from an edge-on loop in stainless steel. Only matrix reflections were evident; no precipitate reflections were observed.

18 A series of micrographs in stainless steel illustrating the asymmetry in {100} fault contrast with $\pm g = [1\bar{1}\bar{1}]^*$ and in loop contrast with $g = [\bar{2}20]^*$. c.f. Figure 15.

19 A $g/3g$ $[\bar{2}20]^*$ weak beam dark field image near $\underset{\sim}{B} = 110$ showing {100} fault contrast and fine matrix precipitates.

20 A multibeam image from a stainless steel sample with $\underset{\sim}{B} = 100$ showing edge-on vacancy-phosphorus loops and fine matrix carbide precipitates. The carbides appear to have {100} habit planes; the (100) variant is visible through residual contrast (see arrows).

21 (a) A 100 multibeam image from a stainless steel sample slowly quenched from 1150°C and aged at 600°C for 10h. (b) 110 and (c)

100 selected area diffraction patterns from the region shown in (a). The diffraction evidence confirms that the carbides are $M_{23}C_6$-type.

22 A BF and $\underset{\sim}{g}/3\underset{\sim}{g}$ [111]* WBDF pair near $\underset{\sim}{\beta}$ = 21$\bar{1}$ illustrating "coarse" matrix precipitates near the arrows.

23 A diffraction contrast analysis of a dislocation decorated with precipitates. (a)-(c) are near $\underset{\sim}{\beta}$ = 110 and (d)-(f) are near $\underset{\sim}{\beta}$ = 111. Section BC has a pure edge character. See text for further details.

24 Precipitation on a climbing dislocation imaged near $\underset{\sim}{\beta}$ = 100 in (a) and (b) and near $\underset{\sim}{\beta}$ = 21$\bar{1}$ in (c) and (d).

25 A diffraction contrast analysis of heterogeneously nucleated precipitates in a stainless steel sample aged at 500°C for 100h. Dislocation A has an edge configuration, B has a mixed character and C is a helical array. The text provides further explanations.

26 A weak beam dark field stereo pair with $\underset{\sim}{g}$ = [$\bar{1}$11]* illustrating precipitation on climbing dislocations with mixed characters (A and B) and on a helix (C).

27 Precipitate-free zones near a grain boundary in a stainless steel sample aged at 500°C for 10h. (a) is a BF image and (b) and (c) are WBDF images showing dual width of the denuded region. The PFZ for the {100} faulted loops is larger than for the $M_{23}C_6$-type precipitates.

28 Precipitate free zones near a grain boundary in a sample aged at 600°C for 1h. The PFZ in grain 2 is larger due to precipitation on climbing dislocations.

29 (a) Triple junction in a sample aged at 500°C for 10h which has a uniform PFZ between grains 1-2 and 1-3, but precipitation on and near grain boundary 2-3. Axis-angle pair determinations were made from the diffraction pattern pairs in (b)-(d). Grain boundaries 1-2 and 1-3 are high angle disordered boundaries while 2-3 is an incoherent twin boundary.

30 Microstructures from samples quenched from 1150°C and aged at (a) 600°C for 10h and (b) 700°C for 1h. No intragranular precipitation was evident.

31 Phosphide precipitation from a sample double aged at 500°C for 10h and 700°C for 24h. Three variants of the {100} laths are visible in this 100 multibeam image.

32 Convergent beam microdiffraction patterns from a phosphide lath with a (010) habit plane. The [010], [110] and [310] reciprocal lattice sections are shown respectively in (a)-(c). Figure (d) is a schematic representation of the reciprical lattice unit cell of the phosphide phase.

33 A diffraction contrast series from a stainless steel sample directly quenched from 1150°C to 500°C and aged for 10h. Dislocations A-C lie on {100} planes and are analogous to those produced by quench-age treatments. (c.f. Figure 15). Defects F-H are vacancy-type edge loops on {110} planes with $\underset{\sim}{b}$ = a/2 <110>. Figures (a)-(d) are near $\underset{\sim}{B}$ = 110 and (e)-(h) are near $\underset{\sim}{B}$ = 100. See the text for additional details.

34 A BF/WBDF pair with $\underset{\sim}{g}$ = [$\bar{2}$20]* near $\underset{\sim}{B}$ = 110 illustrating the fault fringes and dislocation loops of the {100} defects in a

direct-quenched specimen.

35 Grain boundary triple junction in a sample directly quenched to 500°C showing denuded regions between grains 1-2 and 1-3 and precipitation on and near boundary 2-3.

36 A psuedo-binary Fe-2%Si-C phase diagram showing the approximate carbon content in equilibrium with the α-phase at 850°C; after reference 29.

37 The unit cell for bct $Fe_{16}N_2$ (α") used for the carbide growth model proposed in the text; after reference 99.

38 Psuedo-binary Fe-35%Ni-P phase diagram extraploted from data presented in references 103, 106.

39 A schematic illustration of the a/3 [100] stacking fault in the stainless steel; after reference 93.

40 (a) A [$\bar{2}$20]* two beam CBMD pattern for foil thickness measurements in stainless steel. (b) A plot of $(s_i/n_i)^2$ vs $(1/n_i)^2$ which provides a foil thickness of ∿132nm and a <220>* electron distance of ∿40nm.

41 A [111] CBMD zone axis pattern illustrating the HOLZ ring of radius R and fine HOLZ lines in the central disk in a stainless steel sample.

42 A schematic drawing illustrating the procedure used to determine the lattice parameters of the stainless steel specimens. Refer to the appendix for more details.

43 The central disks from 111 zone axis patterns from stainless steel samples aged in various conditions.

44 A plot of the change in lattice parameters relative to the as-quenched condition as a function of thermal treatment.

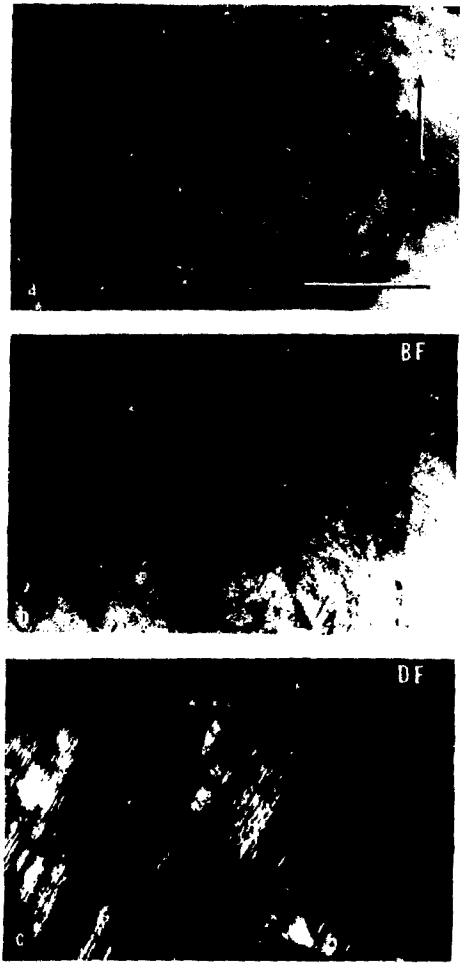

Fig. 1 XBB 826-5145

XBB 809-11365

Fig. 2

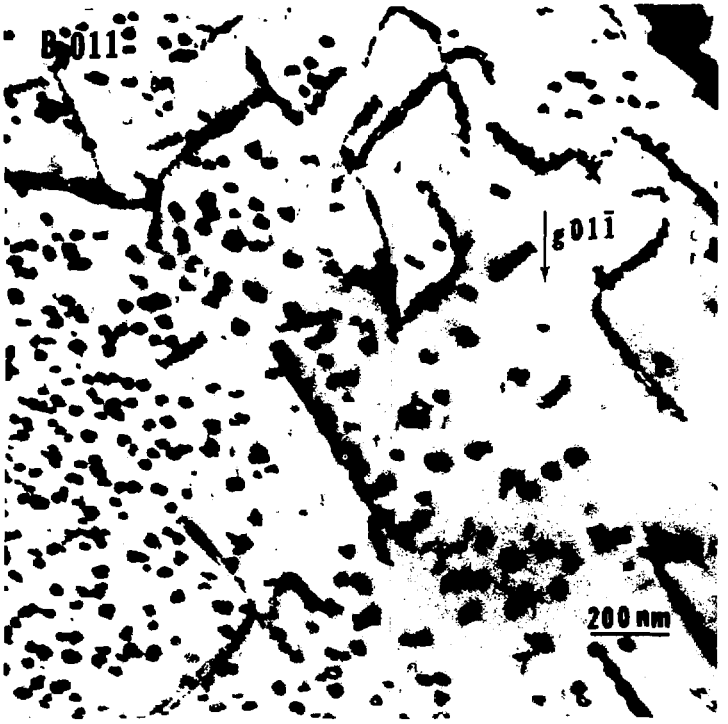

XBB 809-11366

Fig. 3

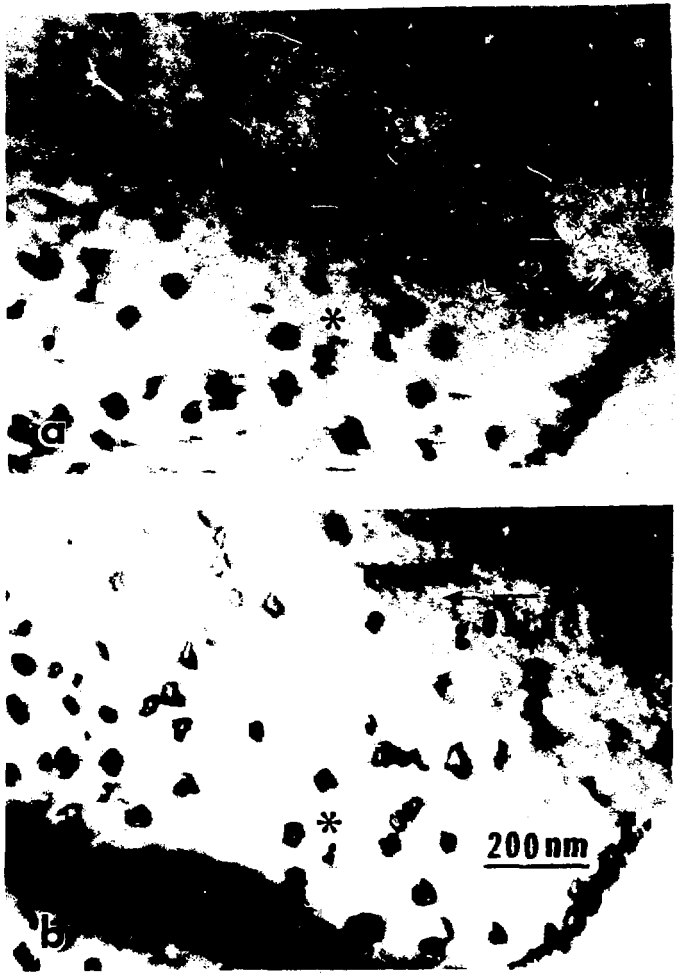

XBB 809-11361

Fig. 4

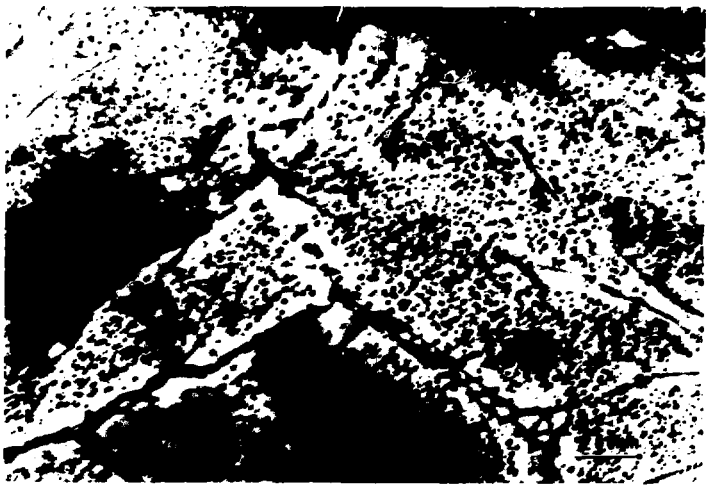

XBB 826-5144

Fig. 5

XBB 826-5143

Fig. 6

XBB 809-11363

Fig. 7

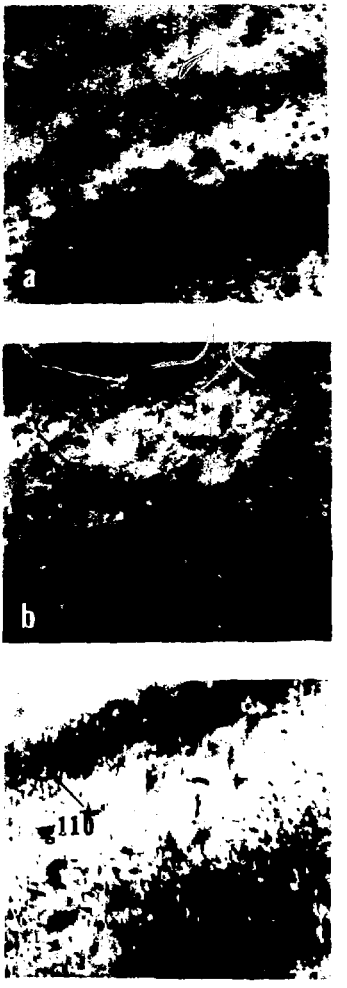

XBB 809-11364

Fig. 8

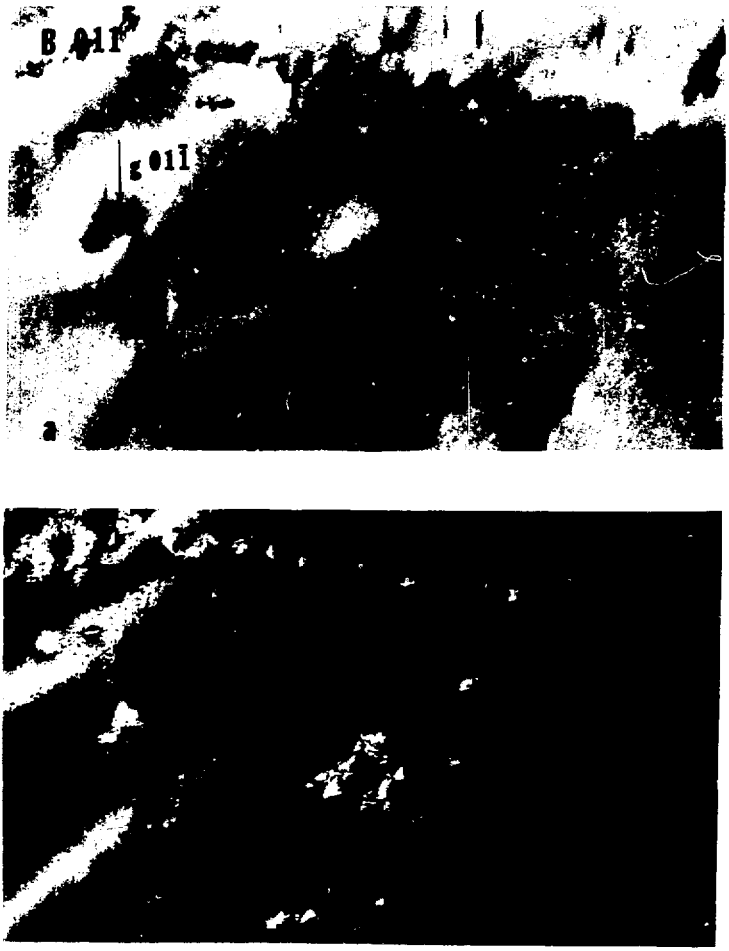

Fig. 9

XBB 809-11360

XBB 826-5148

Fig. 10

Fig. 11

XBB 826-5147

Fig. 12

XBB 826-5146

Fig. 13 XBB 826-5152

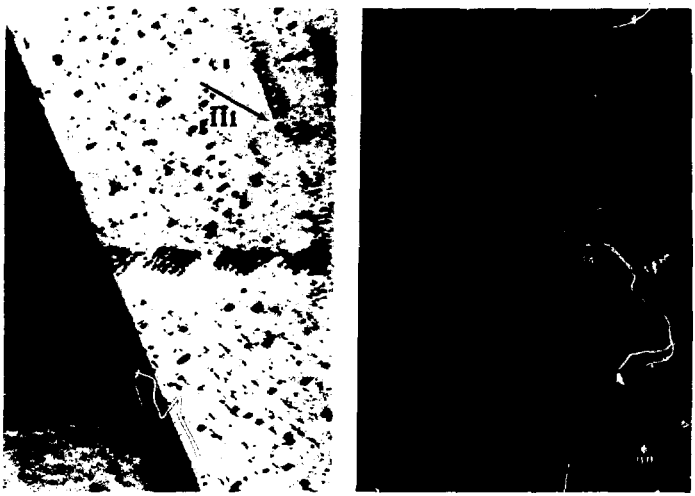

XBB 826-5151

Fig. 14

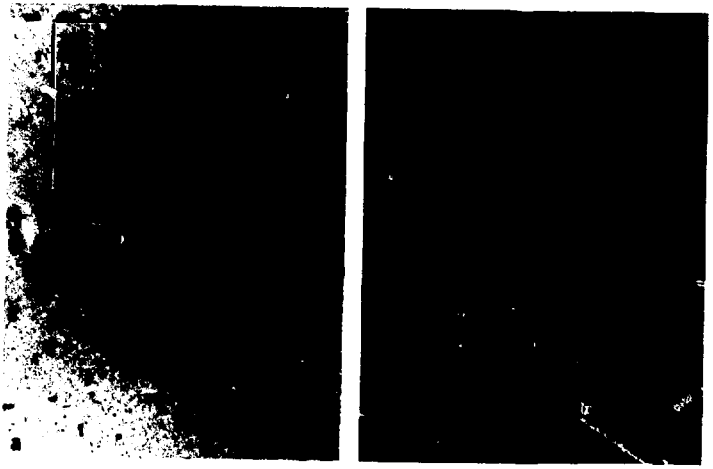

XBB 826-5170

Fig. 15a-b

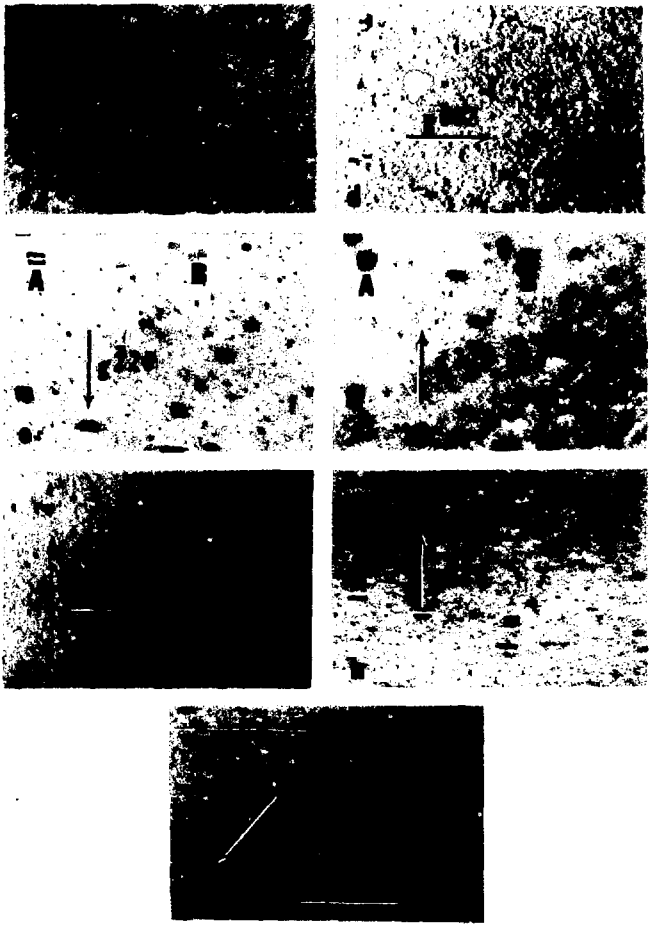

XBB 826-5171

Fig. 15c-i

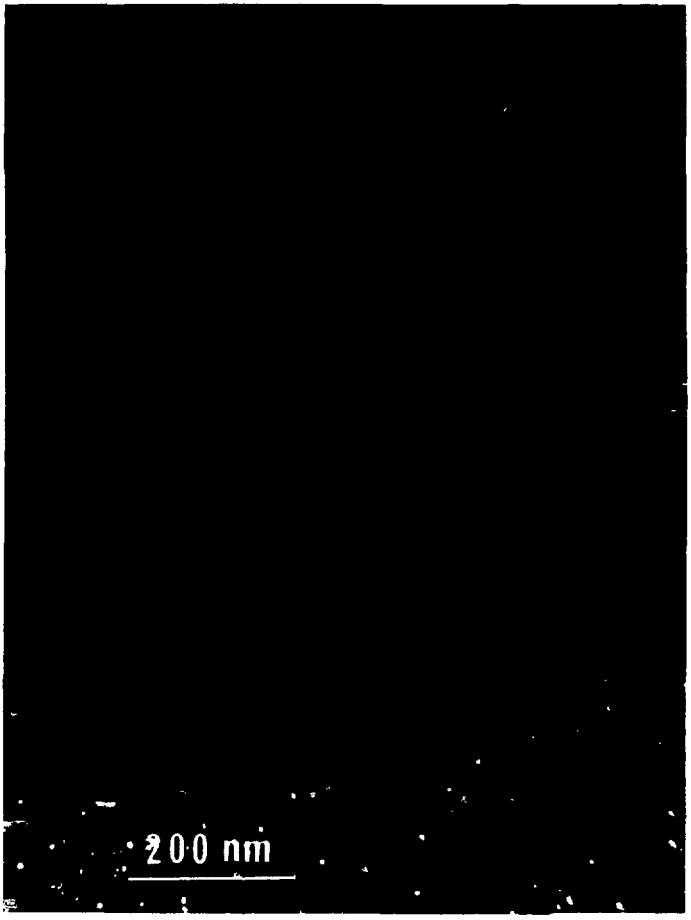

XBB 826-5165

Fig. 15j

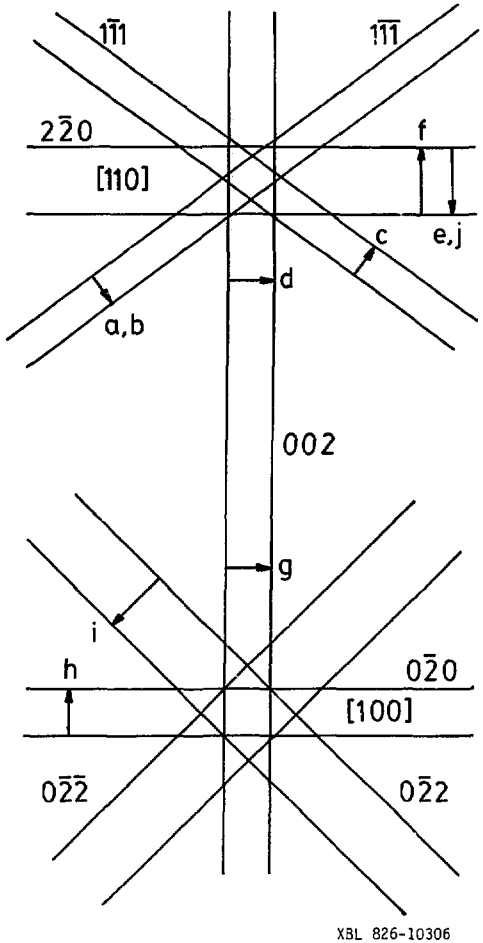
1$\bar{1}\bar{1}$
1$\bar{1}$1
2$\bar{2}$0
[110]
f
e,j
c
d
a,b
002
g
i
h
0$\bar{2}$0
[100]
0$\bar{2}\bar{2}$
0$\bar{2}$2
XBL 826-10306

Fig. 16

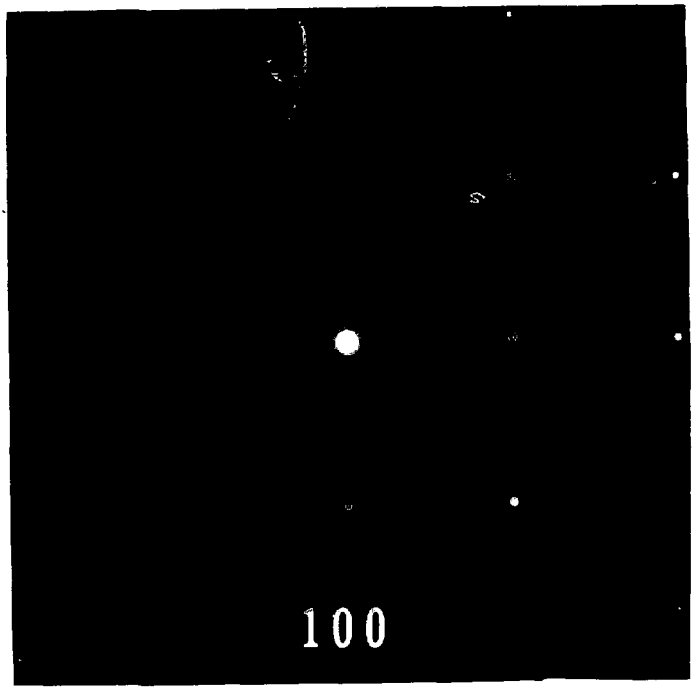

XBB 826-5166

Fig. 17

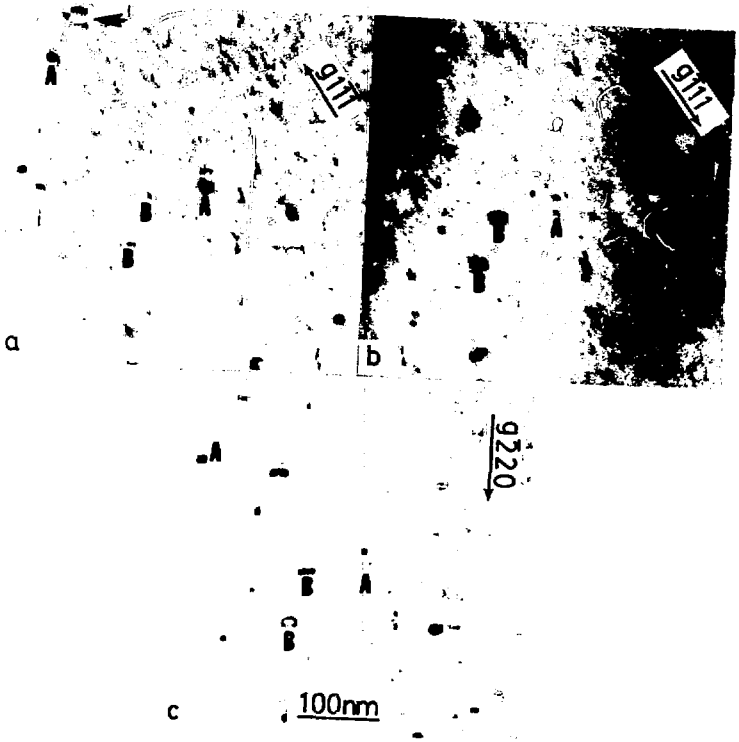

XBB 826-5155

Fig. 18

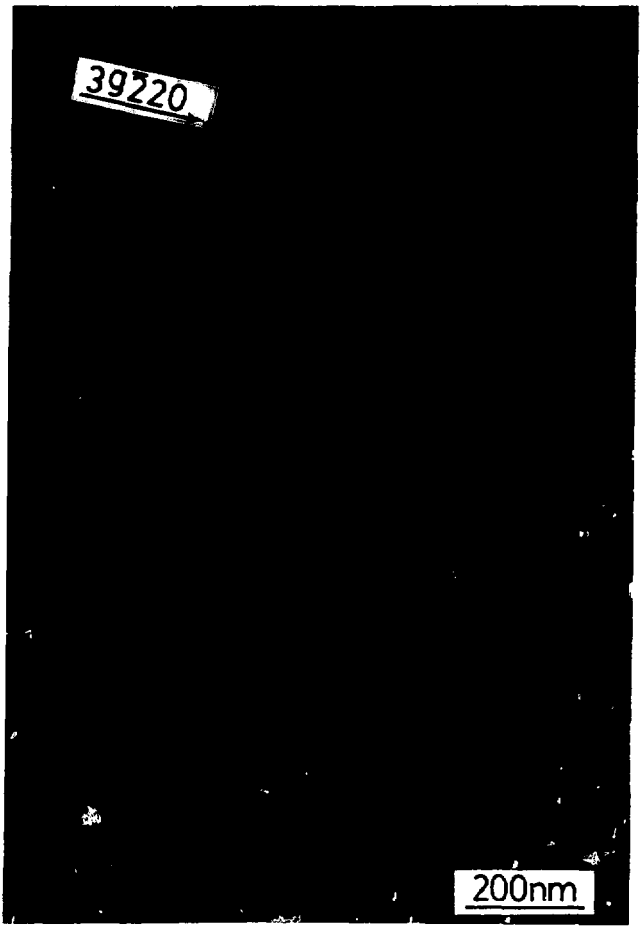

XBB 826-5156

Fig. 19

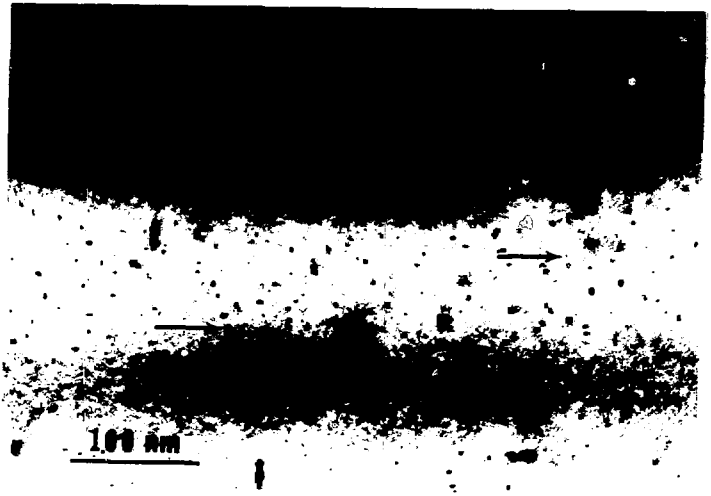

Fig. 20

XBB 826-5173

XBB 826-5172

Fig. 21a

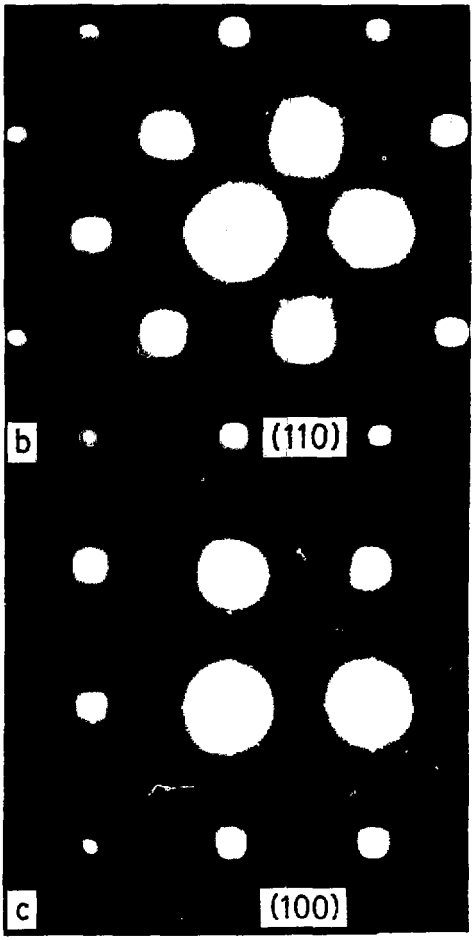

XBB 826-5157

Fig. 21b-c

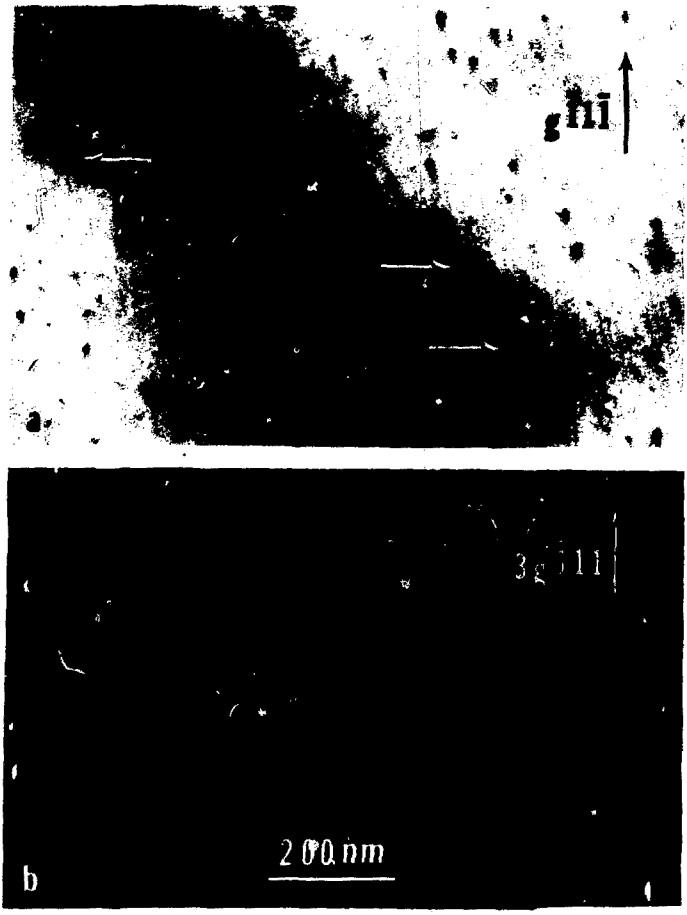

XBB 826-5158

Fig. 22

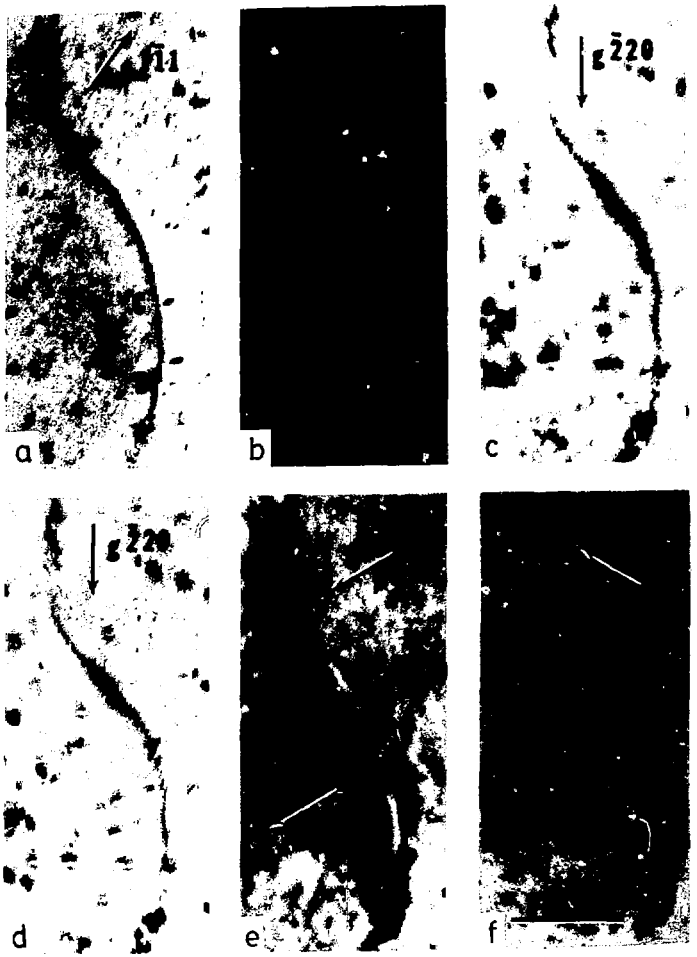

XBB 826-5150

Fig. 23

XBB 826-5169

Fig. 24

XBB 826-5149

Fig. 25

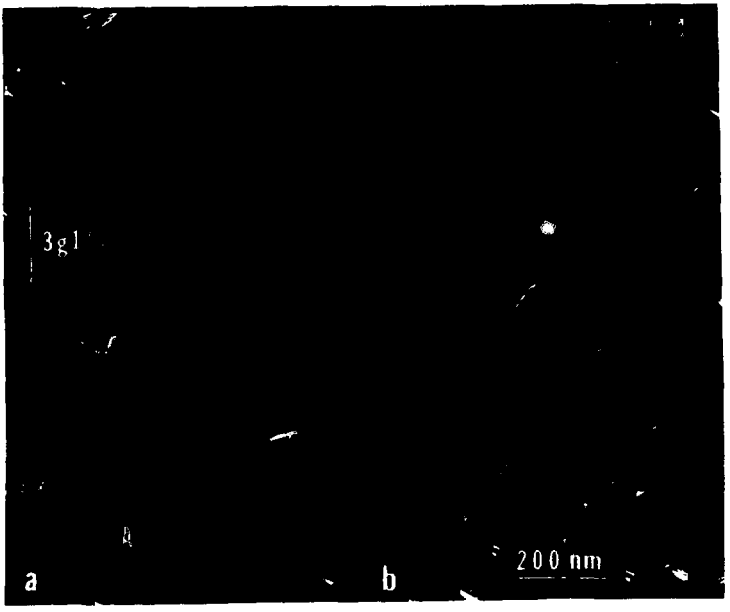

XBB 826-5153

Fig. 26

Fig. 27

XBB 826-5162

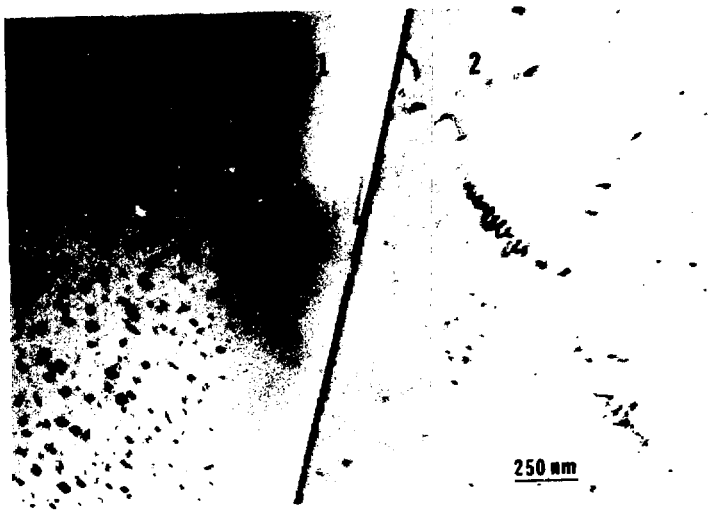

XBB 826-5161

Fig. 2B

XBB 826-5100

Fig. 29a

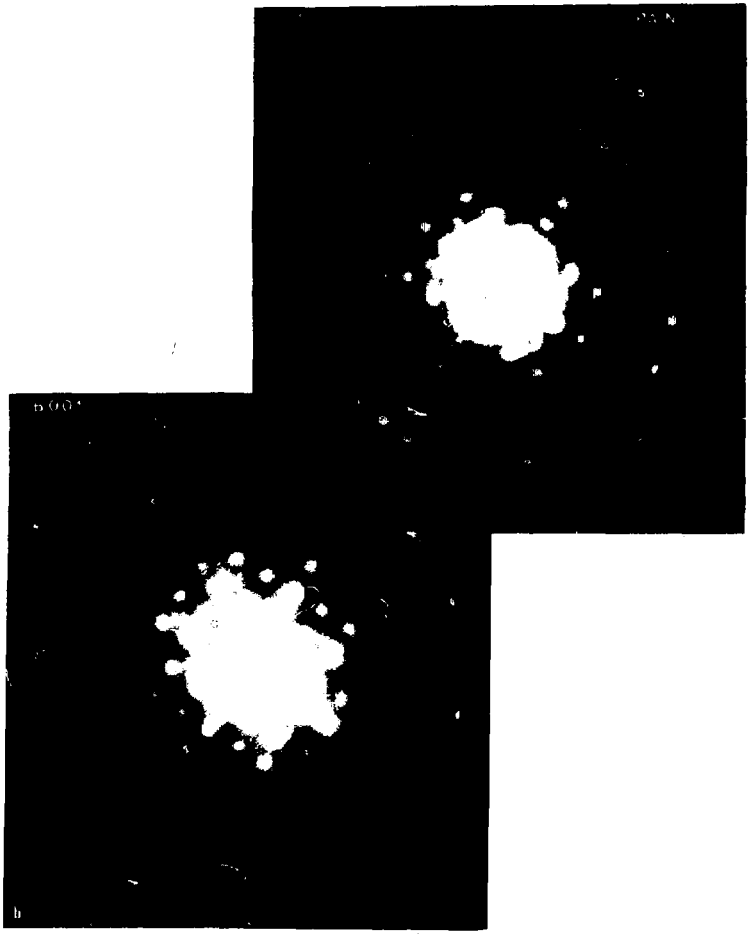

XBB 826-5176

Fig. 29b

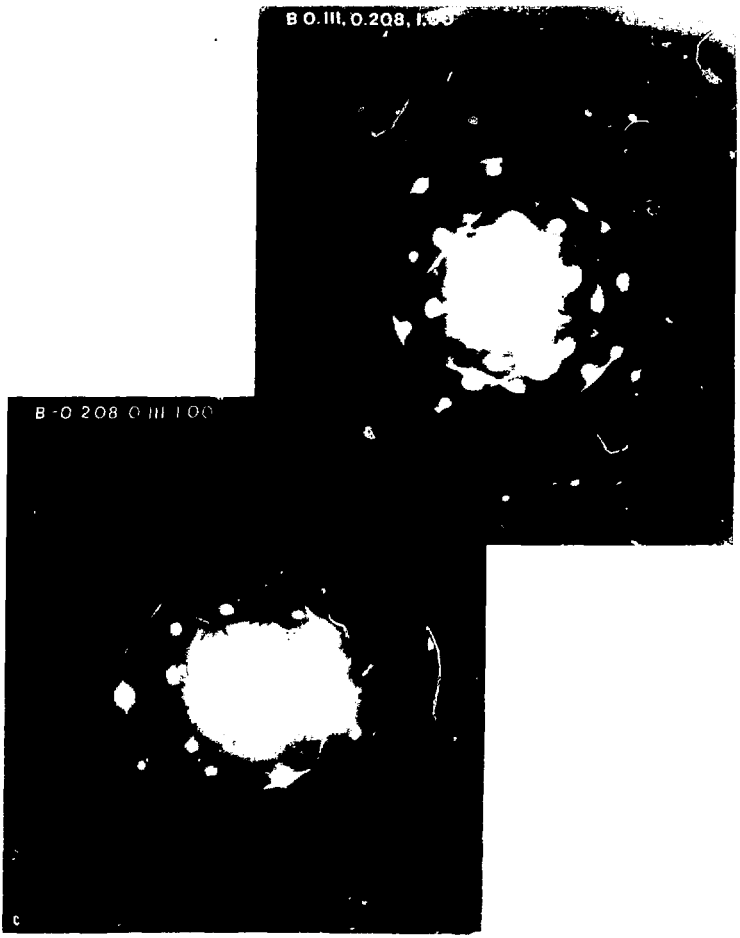

XBB 826-5143

Fig. 29c

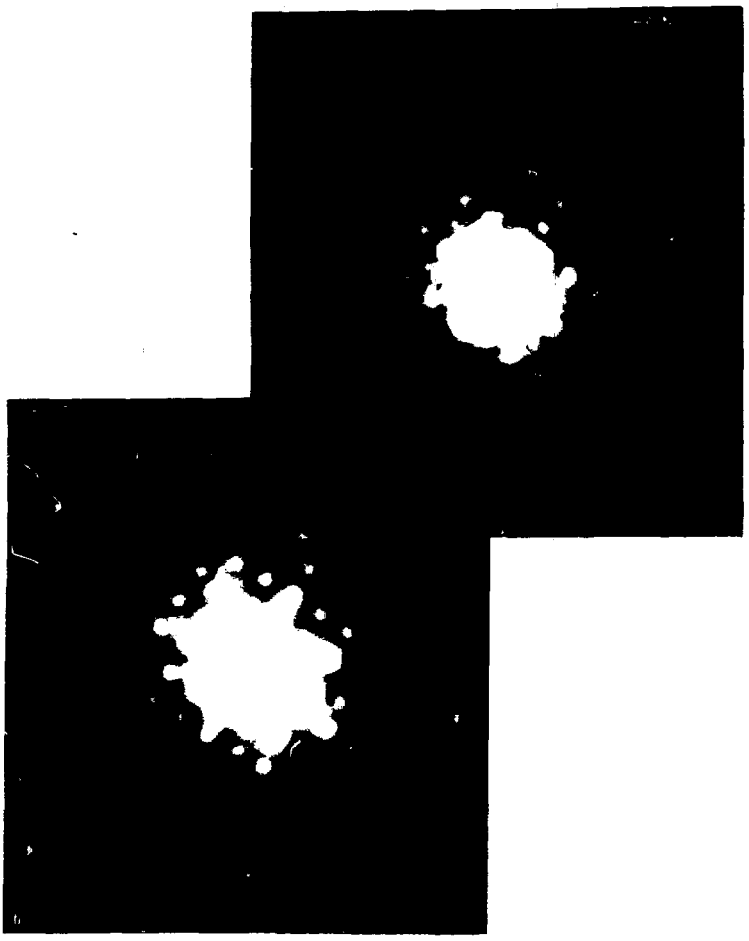

XBB 826-5176

Fig. 29b

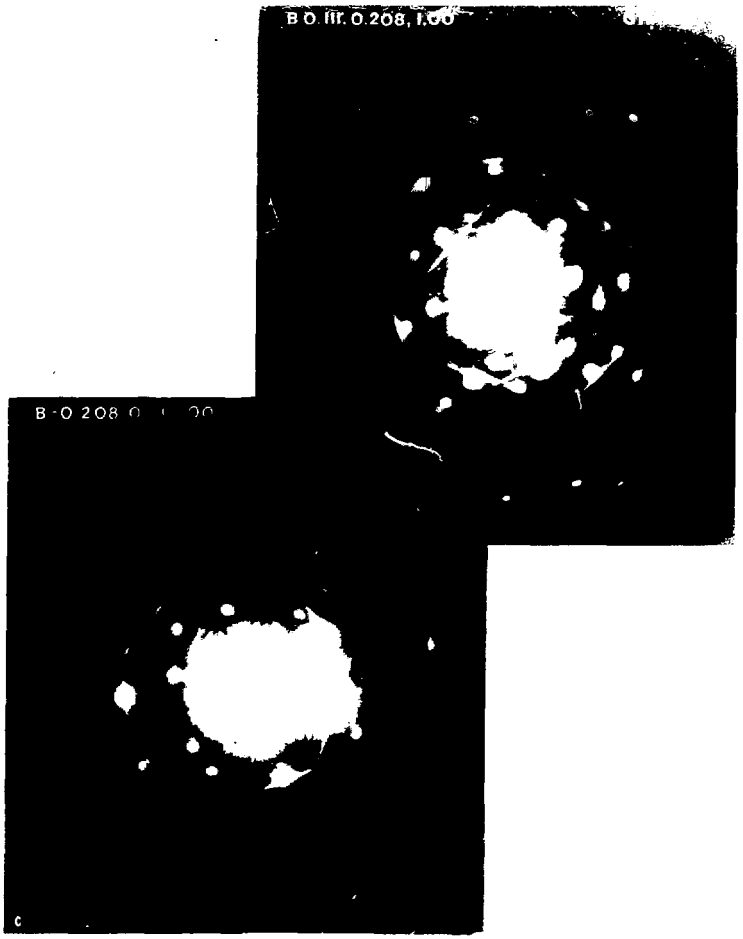

XBB 826-5140

Fig. 29c

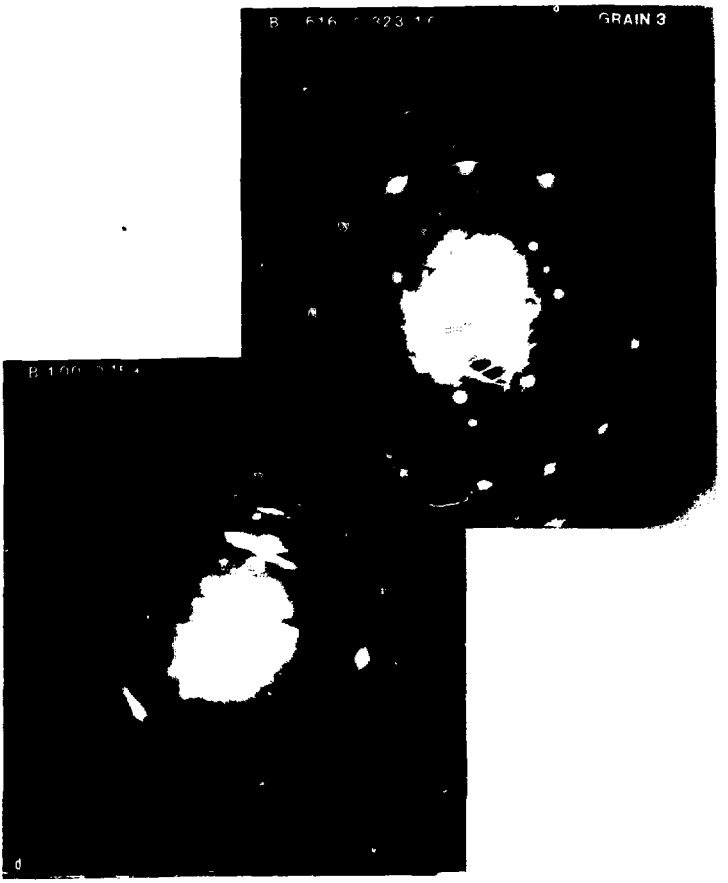

XBB 826-5141

Fig. 29d

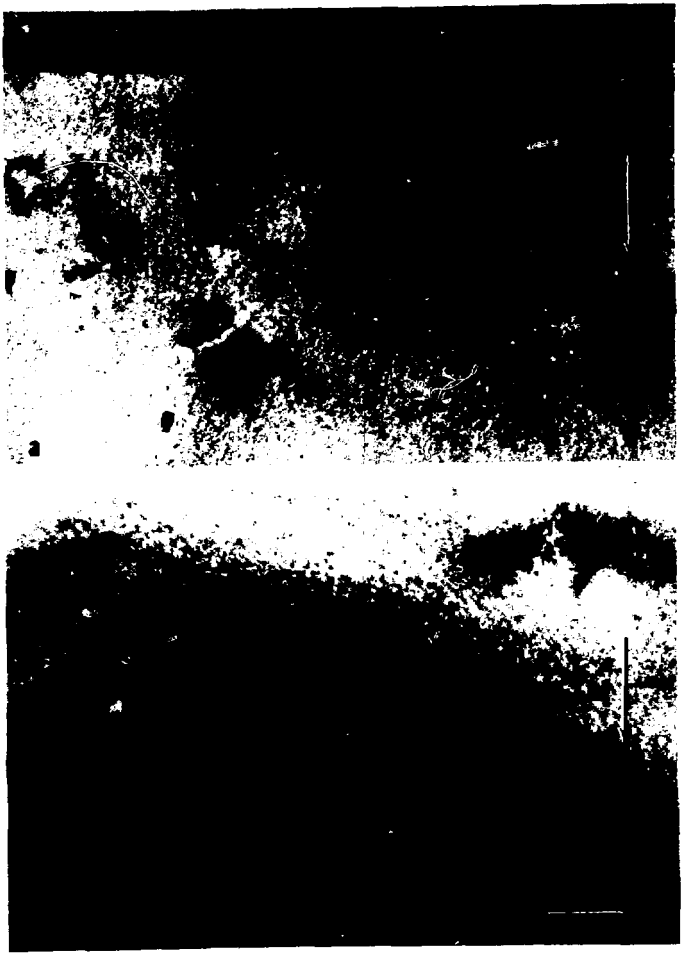

XBB 826-5154

Fig. 30

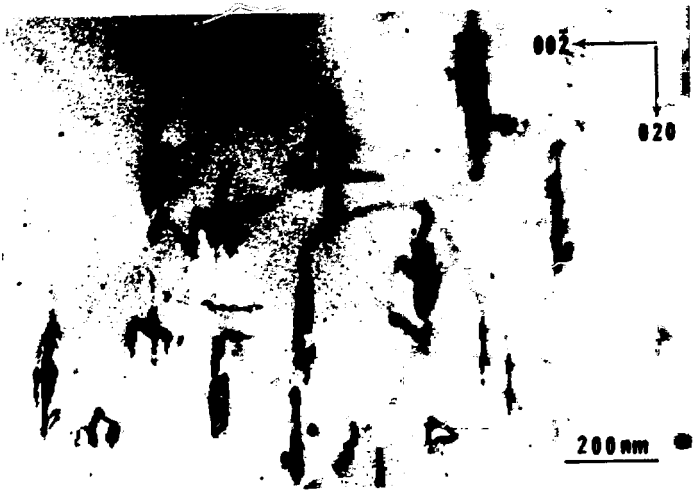

Fig. 31

XBB 826-5159

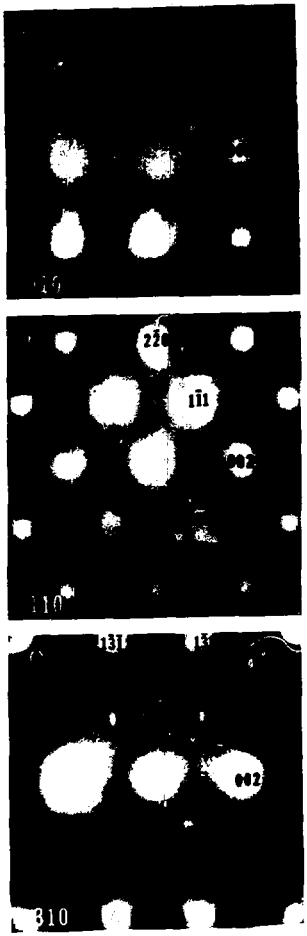

XBB 826-5174

Fig. 32a-c

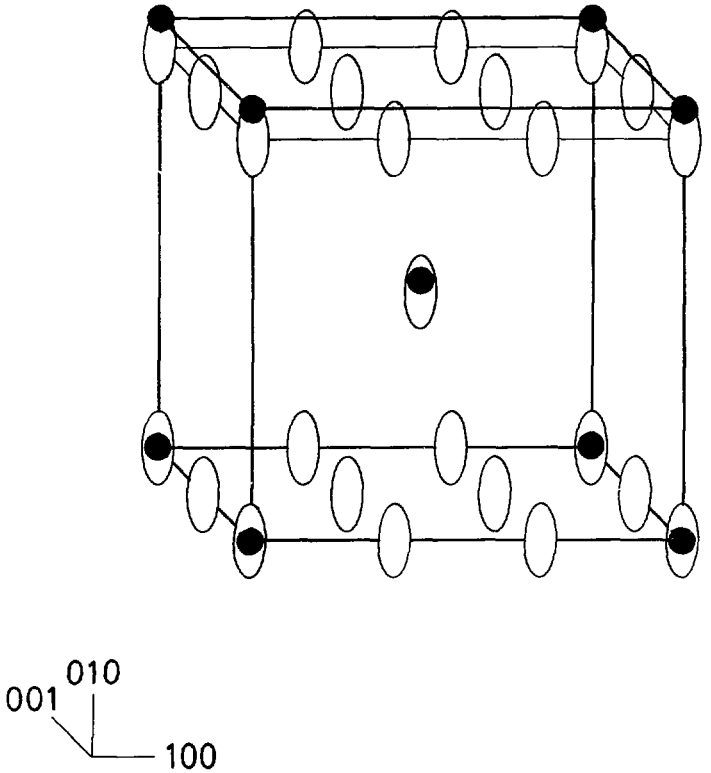

XBL 826-10370

Fig. 32d

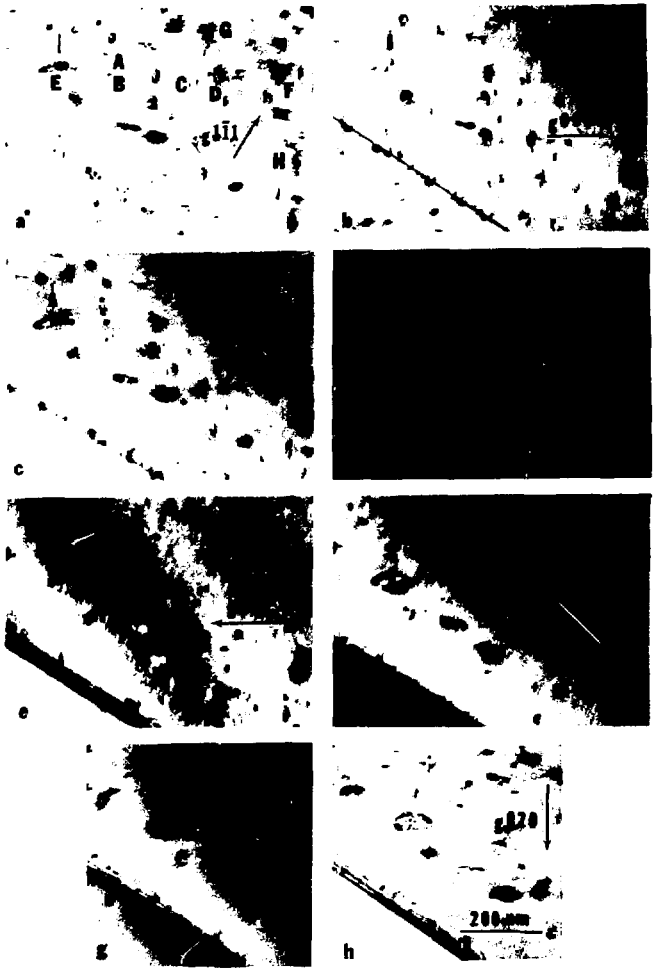

Fig. 33 XBB 826-5142

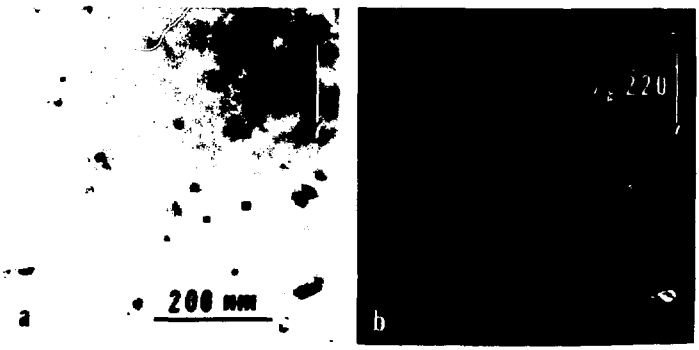

Fig. 34

XBB 826-5164

Fig. 35

XBB 826-5163

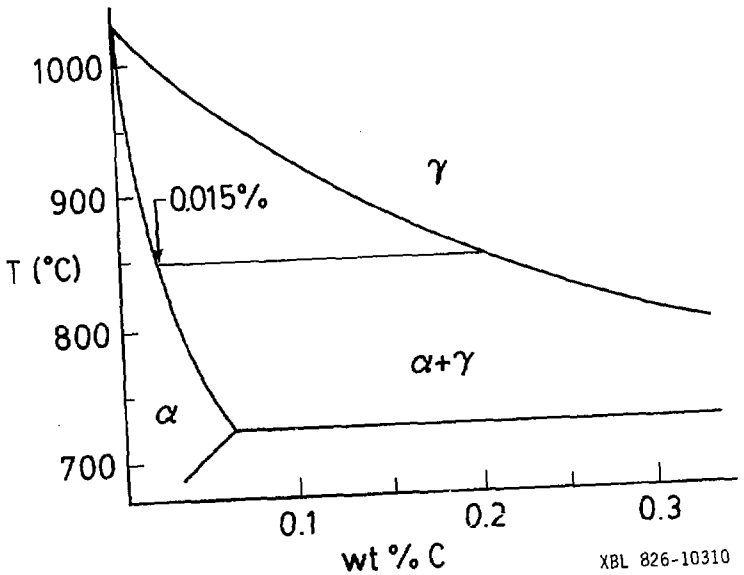

Fig. 36

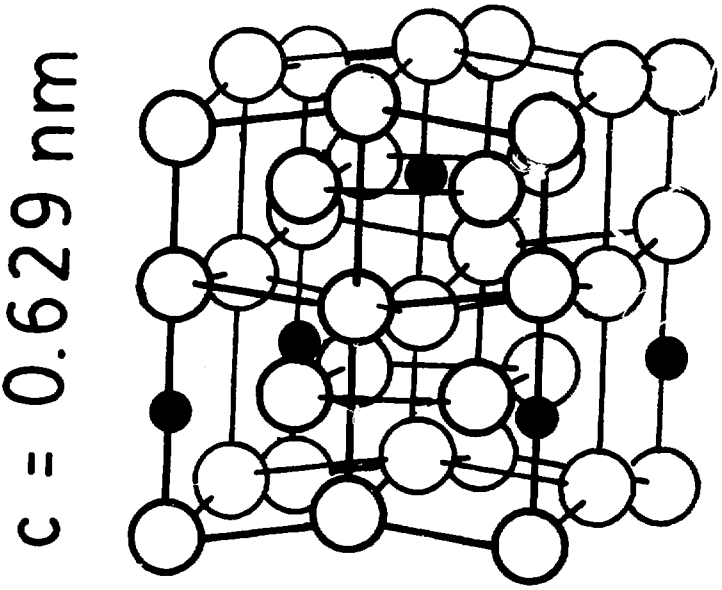

XBL 8112-13037

Fig. 37

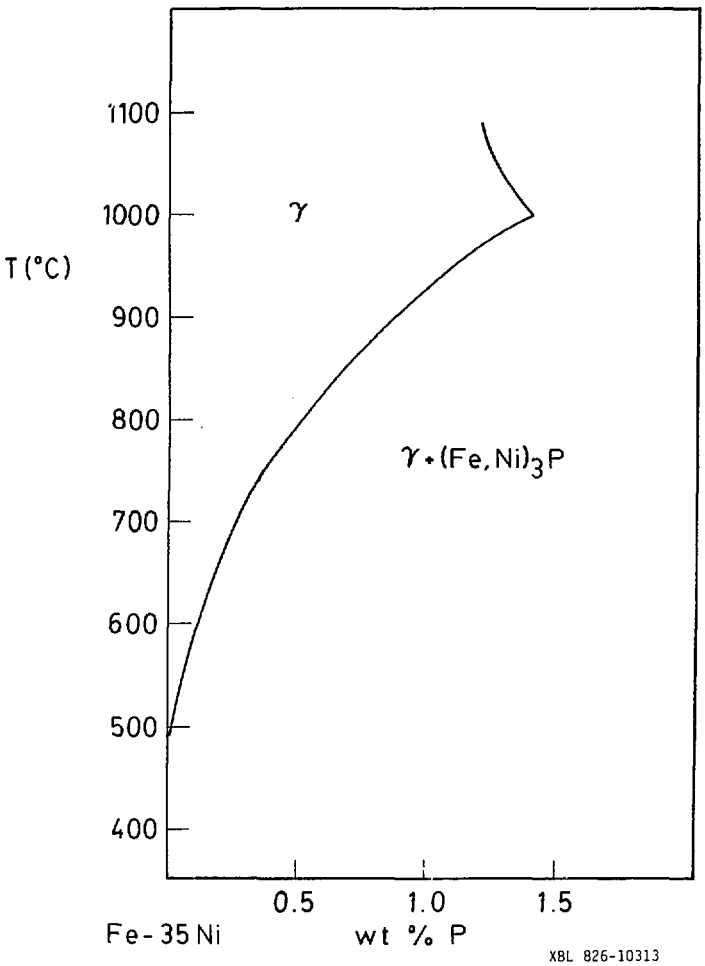
T (°C)
1100
1000
900
800
700
600
500
400
γ
γ + (Fe, Ni)3P
0.5
1.0
1.5
Fe - 35 Ni
wt % P
XBL 826-10313

Fig. 38

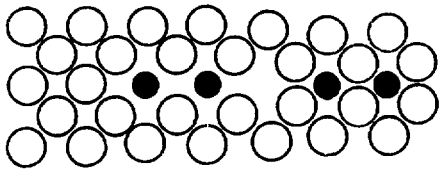

b = a/3 [100]

XBL B26-10307

Fig. 39

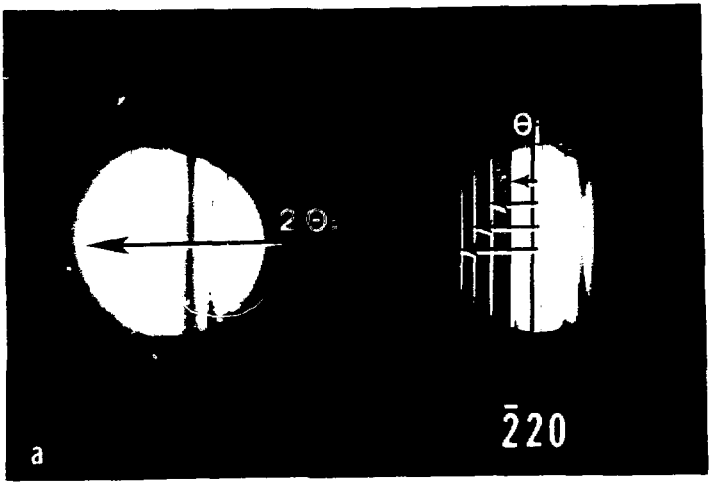

XBB 826-5167

Fig. 40a

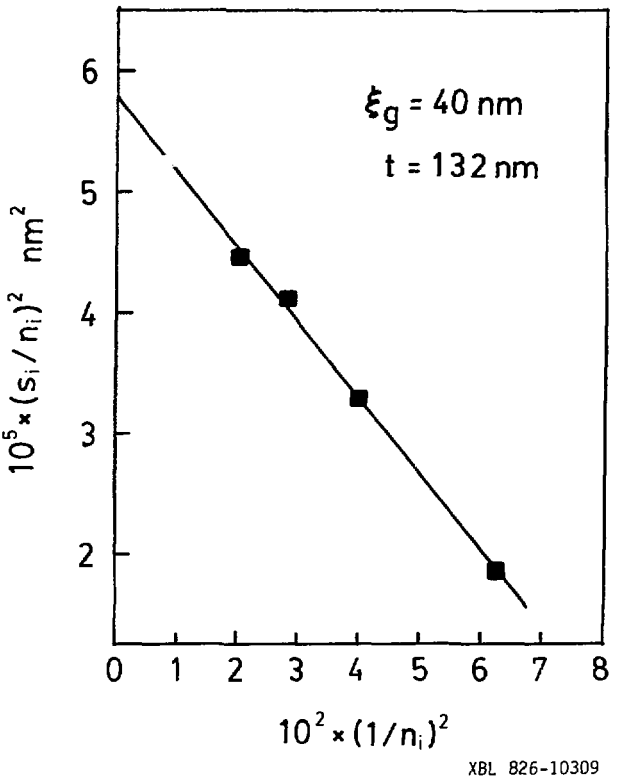

XBL 826-10309

Fig. 40b

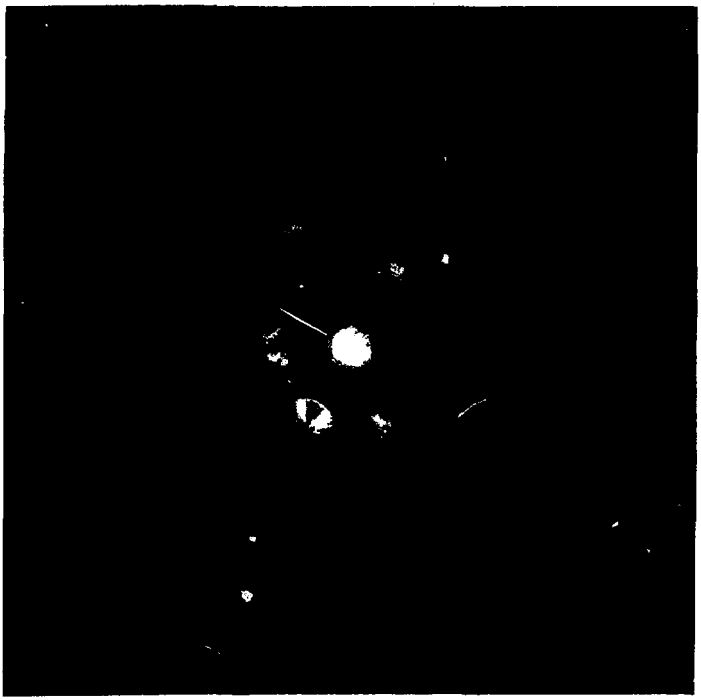

XBB 826-5168

Fig. 41

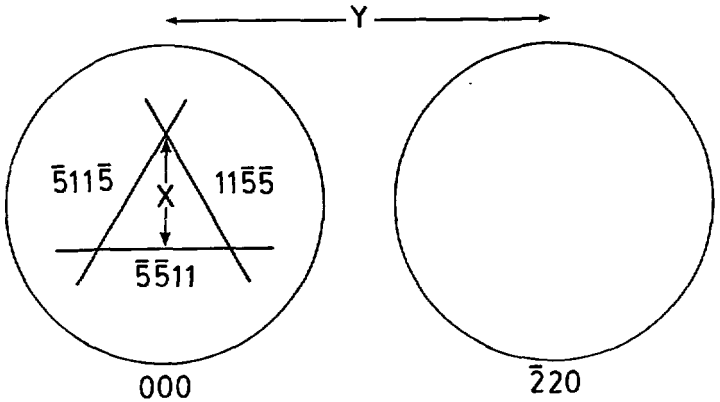

$$\frac{\Delta a}{a_{ref}} \sim \left[\frac{X}{Y} - \frac{X_{ref}}{Y_{ref}}\right] \div R$$

XBL 826-10312

Fig. 42